Microstructural Analysis of Mild Traumatic Brain Injury in Pediatrics using DTI and QSM

MICROSTRUCTURAL ANALYSIS OF MILD TRAUMATIC

BRAIN INJURY IN PEDIATRICS USING DTI AND QSM

BY

DAVID STILLO, B.Eng.Mgt

A THESIS

SUBMITTED TO THE DEPARTMENT OF BIOMEDICAL ENGINEERING

AND THE SCHOOL OF GRADUATE STUDIES

OF MCMASTER UNIVERSITY

IN PARTIAL FULFILMENT OF THE REQUIREMENTS

FOR THE DEGREE OF

MASTER OF APPLIED SCIENCE

Master of Applied Science (2016)   McMaster University

(Biomedical Engineering)   Hamilton, Ontario, Canada

TITLE: Microstructural Analysis of Mild Traumatic Brain Injury

                    in Pediatrics using DTI and QSM

AUTHOR: David Stillo

                    B.Eng.Mgt., (Mechanical Engineering)

                    McMaster University, Hamilton, Canada

SUPERVISOR: Dr. Michael Noseworthy

NUMBER OF PAGES: xiv, 123

Lay Abstract

Concussions affect over one million people in the United States each year. In a number of cases, these individuals must cope with persistent long-term cognitive impairment resulting from the injury. Currently, a significant problem is that concussions cannot be reliably diagnosed using conventional CT and MR imaging methods. Therefore, an accurate and reliable imaging method is needed to determine both injury location and severity, as well as to monitor healing. The goal of this study was to quantify concussion through MR imaging techniques known as Diffusion Tensor Imaging and Quantitative Susceptibility Mapping, which accurately model the brain's microstructure. Analysis utilizing these MRI methods found significant abnormalities in a number of brain regions of concussed subjects relative to healthy individuals. These results suggest that DTI, in particular, is sensitive to microstructural changes caused by concussions and has the potential to be a useful tool for improving diagnosis accuracy.

Abstract

Each year in the United States, approximately 1.35 million people are affected by mTBI (aka concussion) and subsequent cognitive impairment. Approximately 33% of mTBI cases results in persistent long-term cognitive deficits despite no abnormalities appearing on conventional neuroimaging scans. Therefore, an accurate and reliable imaging method is needed to determine injury location and extent of healing. The goal of this study was to characterize and quantify mTBI through DTI, an advanced MRI technique that encodes voxel-wise tissue water microstructural diffusivity as a tensor, as well as QSM, which measures iron deposition within tissues. We hypothesized that personalizing the analysis of DTI and QSM will provide a better understanding of trauma-induced microstructural damage leading to improved diagnosis and prognosis accuracy. Through regression analysis, a preliminary comparison between DTI data to QSM measurements was performed to determine potential correlations between the two MRI techniques. Further, a large database of healthy pediatric brain DTI data was downloaded and each was warped into a standardized brain template to ultimately use for voxel-wise z-score analysis of individual mTBI patients (n=26). This allowed localization and quantitation of abnormal regions on a per-patient basis. Significant abnormalities were commonly observed in a number of regions including the longitudinal fasciculus, fronto-occipital fasciculus, and corticospinal tract, while

unique abnormalities were localized in a host of other areas (due to the individuality of each childs injury). Further, through group-based Bonferroni corrected T-test analysis, the mTBI group was significantly different from controls in approximately 65% of regions analyzed. These results show that DTI is sensitive to the detection of microstructural changes caused by mTBI and has potential to be a useful tool for improving mTBI diagnosis accuracy.

Acknowledgements

I would truly like to thank my supervisor, Dr. Michael Noseworthy, for the opportunity to work in his lab in and for all of the guidance and support provided over these past two years. Thanks are also due to Dr. Carol DeMatteo and Dr. John Connolly for their advice throughout the project. Norm Konyer, thank you for all of your help, especially on the technical side of things. Further, I would like to acknowledge the IRC technologists, Carol Awde, Cheryl Contant, and Julie Lecomte, for all the work put in during data collection. I really appreciate all the efforts made by Chia-Yu Lin and the Back 2 Play team reaching out to patients and helping to schedule exams. And of course I have to thank Rachelle Ho for helping to coordinate everything for the study and for giving me someone to bounce ideas off of throughout the whole process (also, thanks to you, I can say that I now know the first 30 minutes of Wall-E by heart).

And last but not least, a huge thank you to all my labmates; Alireza Akbari, Michael Behr, Caty Charles Herrera, Olga Dona Lemus, Mitch Doughty, Amy Harrison, Evan McNabb, Conrad Rockel, Alejandro Santos Diaz and Saurabh Shaw. It's been an absolute pleasure getting to know each and every one of you. Our (almost) daily discussions regarding the latest GOT theories were always a welcome distraction and will definitely be missed. Thanks everyone for a great two years!

Notation and Abbreviations

AD   Axial diffusivity

ADC   Apparent diffusion coefficient

BET   Brain extraction tool

CNR   Contrast-to-noise ratio

CSF   Cerebrospinal fluid

DAI   Diffuse axonal injury

DTI   Diffusion tensor imaging

DWI   Diffusion weighted imaging

EMF   Electromotive force

EPI   Echo-planar imaging

FA   Fractional anisotropy

FOV   Field-of-view

FT   Fourier Transform

GCS	Glasgow coma scale
GM	Gray matter
HARDI	High angular resolution diffusion imaging
iLSQR	Initial least-squares regression
MD	Mean diffusivity
MRI	Magnetic Resonance Imaging
mTBI	Mild traumatic brain injury
PCSS	Post-concussive symptom scale
QSM	Quantitative susceptibility mapping
RD	Radial diffusivity
RF	Radio frequency
ROI	Region of interest
SNR	Signal-to-noise ratio
SWI	Susceptibility weighted imaging

T1   Spin-lattice relaxation time

T2   Spin-spin relaxation time

TBI   Traumatic brain injury

TE   Echo time

TR   Repetition time

WM   White matter

Contents

List of Figures

Chapter 1

Introduction

1.1 Thesis Statement

Mild traumatic brain injury (mTBI), commonly referred to as concussion, affects approximately 1.35 million people in the United States each year (Bazarian *et al.*, 2006). In most cases, symptoms tend to resolve in a matter of days, however, approximately 15 to 30% of people experience post concussive symptoms three months post injury (Vanderploeg, 2007). Areas of cognitive impairment resulting from mTBI include memory, information processing speed, attention, and executive function (Parizel, 2007). Sports-related TBI attracts significant attention as the assessment and ultimate decision of when an athlete should return to play is unclear. Studies propose that resuming full activity too quickly can place the individual at a greater risk of sustaining future concussions (Guskiewicz, 2005). In rare cases, if an individual sustains a second concussion before the initial injury has resolved, the brain may undergo rapid swelling and possible herniation. This is known as second-impact syndrome (Cantu, 1998). Research by Binder et al. suggests that 33% of mTBI cases results in

persistent long-term cognitive deficits despite no abnormalities appearing on conventional neuroimaging scans (Binder *et al.*, 1997a,b). Therefore it is paramount that an accurate, reliable method be developed in order to determine when an individual is safe to return to their particular sport or activity.

1.2   Proposed Solution

Advanced imaging methods are required to improve diagnosis and prognosis in cases of mTBI. Currently, subtle changes in brain structure caused by Diffuse Axonal injury (DAI), which is indicative of mTBI, are not adequately detected using conventional MRI and CT imaging methods (Hughes, 2004a). MR neuroimaging techniques such as Diffusion Tensor Imaging (DTI) are sensitive to subtle changes in white matter fibre tracts revealing microstructural DAI in the brain (Pierpaoli and Basser, 1996). In tissues such as white matter, water diffusivity is not equal in all directions and is termed anisotropic. Utilizing tensors, the shape of the diffusion ellipsoid can be modelled and represented by the parameter fractional anisotropy (FA) where low FA trends toward isotropic diffusivity and high FA is seen in healthy anisotropic myelin. Similarly, the tensor calculation provides further metrics of water mobility known as axial and radial diffusivity (AD and RD, respectively). AD and/or RD may increase when the mobility of diffusing water becomes less restricted. Another structural MR imaging technique, Susceptibility Weighted Imaging (SWI), can be used in conjunction with DTI to better understand mTBI. SWI detects subtle changes in brain tissue, especially in the case of micro-hemorrhaging resulting from mTBI (Haacke *et al.*, 2009). Additionally, because of the deoxyhemoglobin content in blood, SWI can visualize the brain venous system. This data can be quantified through

Quantitative Susceptibility Mapping (QSM). Measurement of QSM and quantification of DAI can be a powerful combination to improve the accuracy of both diagnosis and prognosis of mTBI.

Using advanced brain imaging techniques such as DTI and QSM allows us to visualize and quantify brain abnormalities in cases of mTBI. Improved understanding of microstructural changes resulting from brain injuries will lead to better determination of the severity of brain injury for a given individual. Further, accurate biomarkers of injury, determined through longitudinal studies, will allow us to better predict which patients are likely to recover from their injuries versus which are at greater risk of developing post-concussive symptoms.

1.2.1   Objectives

The focus of this study was to develop methods of analysis using data from a longitudinal cohort of mTBI cases with initial scans scheduled immediately following injury and follow up scans scheduled post-symptom resolution. The objectives were to:

- Compare DTI measures of each injured brain to itself in time and to a large normative database of healthy age-matched human brains using case-based z-score analysis;

- Using a combination of z-scoring and group-based t-scoring analysis, assess which parameters are most sensitive to injury (FA, AD, RD, Susceptibility) and are most likely to help in understanding recovery; and

- Develop a novel approach to correlate QSM-derived brain-iron content from SWI data with DTI measures.

To date, the majority of studies undertaken have focused on only one of the two MR techniques previously discussed. Additionally, most have been cross sectional studies thereby limiting the researchers' ability to assess within subject dynamics over time as well as to assess the effectiveness of different MR techniques at evaluating mTBI. In order to address this limitation, a longitudinal study was implemented to monitor changes in the brain and observe the progression of recovery over time following mTBI. Further, most research in the field of TBI has used SWI and DTI to qualitatively assess microstructural changes in the brain. This study aimed to utilize both QSM and DTI metrics to improve quantification of brain abnormalities indicative of mTBI.

1.2.2   Hypothesis

It has been established that both QSM and DTI are useful techniques for modeling the brain's microstructure. We hypothesize that these methods can be further utilized to assess and monitor patient recovery after sustaining a mTBI. The hypothesis can be summarized as follows:

1. An initial reduction in FA and an increase in one of RD or AD will be observed in particular brain regions of patients with mTBI.

2. After an individual's symptoms have resolved, the FA, AD, and RD abnormalities will also resolve over time.

3. There exists a correlation between iron deposition, as measured by QSM, and an overall reduction in FA, as measured by DTI.

Chapter 2

MRI Overview

MRI is a non-invasive medical imaging technique which uses a magnetic field in addition to pulses of radio wave energy in order to image anatomy and physiological processes within the body. Subjects are situated in a large, homogeneous magnetic field, B_0, for the duration of the scan. The signal acquired from the MR machine is digitized and then reconstructed into a two-dimensional image format using Fourier Transforms. The typical end result is a tomographic series of images, meaning that the images are viewed as 'slices' through a particular plane of the body.

2.1   Signal Generation

The MRI signal is actually generated by protons, primarily the ^{1}H atoms from water (H_2O) due to its great abundance in the human body. Though quantum mechanics are needed in order to fully describe the physics at work behind this process, a classical physics approach is adequate to obtain a general understanding of MRI. Under

normal every day circumstances, individual protons (referred to as spins) are randomly oriented within the body. When placed into a strong magnetic field, some of the spins will tend to orient themselves in the same direction as the field. This results in that volume of tissue having a net magnetization. The spins within this tissue will precess at a frequency, designated the Larmor frequency, which is proportional to the magnitude of the magnetic field. The Larmor equation is defined as:

$$\omega = \gamma B \tag{2.1}$$

where $\gamma = 2.67 \times 10^8 rad/(s \cdot T)$ represents the gyromagnetic ratio for protons.

2.2   Spatial Localization

The relationship defined by equation 2.1 demonstrates that creating known spatial deviations in the applied magnetic field will cause the spins to precess at a unique frequency in that particular region. Tuned radio-frequency (RF) coils are used to transmit and receive these MR signals whereas gradient coils are responsible for producing spatial deviations in the magnetic field by generating three orthogonal linear magnetic field gradients. In order to generate an axial image of the subject, the spins must be tipped into the x-y (transverse) plane by a specialized RF pulse. Note that the z-axis refers to the direction parallel to the bore of the magnet. By applying a linear gradient in the z-direction, the spins are given a linear frequency dependence based on position as defined by:

$$\omega(z) = \gamma G_z z \tag{2.2}$$

where G_z represents the linear gradient dB/dz and z is the position along the z-axis. The image slice may then be selected based on a combination of the gradient, RF transmit centre frequency, and RF transmit bandwidth. At the centre of the volume, spins would precess at the centre frequency of the transmitted RF whereas spins located elsewhere would be within a range defined by the RF transmit bandwidth.

As the spins precess in the transverse plane they produce a variable magnetic flux which, in turn, induces an electromotive force (EMF) in the receiver coil according to Faraday's Law:

$$\xi = -\frac{d\phi_B}{dt} \tag{2.3}$$

where ξ represents the EMF and ϕ_B is defined as the magnetic flux through the coil. The induced current in the coil is dependent on the EMF in addition to the resistance, capacitance and inductance in said coil.

Within each image slice, spatial information is encoded through linear gradients in both the x- and y-axis. The y-axis is incrementally encoded using a gradient lobe, applied for a time T, thereby producing a spatially dependent phase change, ϕ

$$\phi(y) = \gamma y \int_0^T G_y dt \tag{2.4}$$

where G_y represents the linear gradient dB/dy (Bernstein *et al.*, 2004). During signal digitization, the x-axis is encoded using a bipolar gradient lobe.

By applying the Fourier Transform (FT), an image can then be obtained from this generated signal. FT is a mathematical operation used to convert a signal into its individual frequency components through approximation from a finite number of sinusoidal waveforms. The resulting image is the amalgamation of a number of

discrete periodic waveforms with frequencies corresponding to their spatial location.

2.3   K-space and Image Reconstruction

Referring to Figure 2.1, k-space represents the matrix on which raw MRI data is read. For this case, the raw data refers to the spatial frequency information which will be Fourier transformed into image space. The outer regions of k-space represent the high frequency information of the image, which define the finer features and details. Further, the centre of k-space contains the lower frequency components and determines the overall signal level and image contrast. The image field-of-view (FOV) is defined by the extent of k-space. Additionally, the signal-to-noise ratio (SNR) as well as scan time can both be determined based on the contents of k-space.
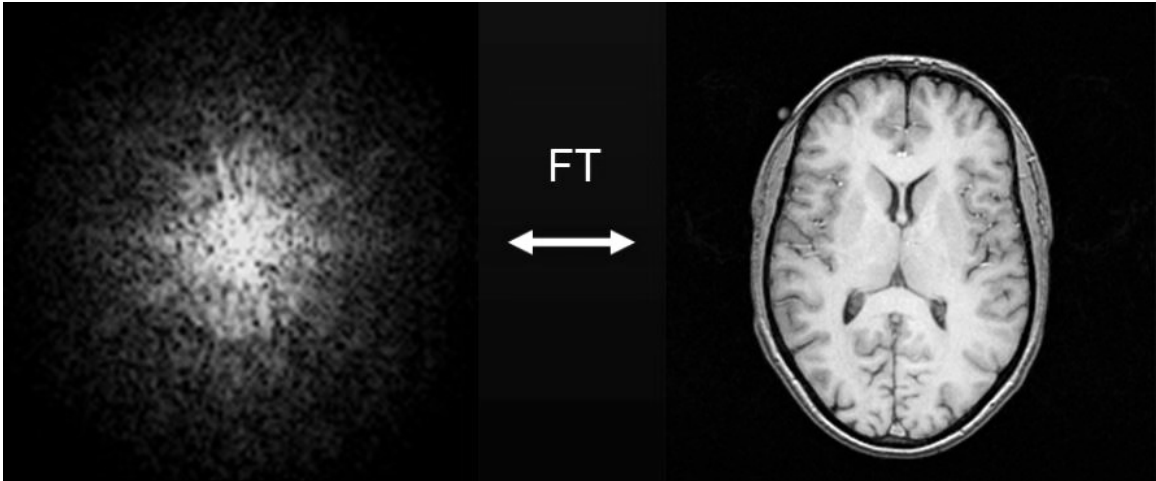
Figure 2.1: Small case 'K'-space and its corresponding image space (image courtesy of Dr. Michael Noseworthy, McMaster University)

The horizontal and vertical axis of k-space are commonly denoted as k_x and k_y, which represent the frequency encoding and phase encoding, respectively. Depending on what image features (such as resolution or field of view) are most critical, various

k-space sampling strategies based on the trajectory in k-space, $\mathbf{k}$, may be utilized. As described by Bernstein (Bernstein *et al.*, 2004), $\mathbf{k}$ is found to be proportional to the time integral of the gradient waveforms, $\mathbf{g}$:

$$\mathbf{k}(t) = \frac{\gamma}{2\pi} \int_0^t \mathbf{g}(\tau)d\tau \tag{2.5}$$

Further, we can conclude that the step size between points in k-space in the frequency encode direction (x) can be defined as:

$$\Delta k_x = \frac{\gamma}{2\pi} g_x(t)\Delta t \tag{2.6}$$

where Δt represents the time between samples. Further, the speed at which acquisition travels through k-space is equivalent to $\Delta k_x/\Delta t$. Refer to Figure 2.2 for an example of a Cartesian-based trajectory through k-space. Alternative strategies such as radial trajectories and spiral trajectories are also used when acquiring image data.
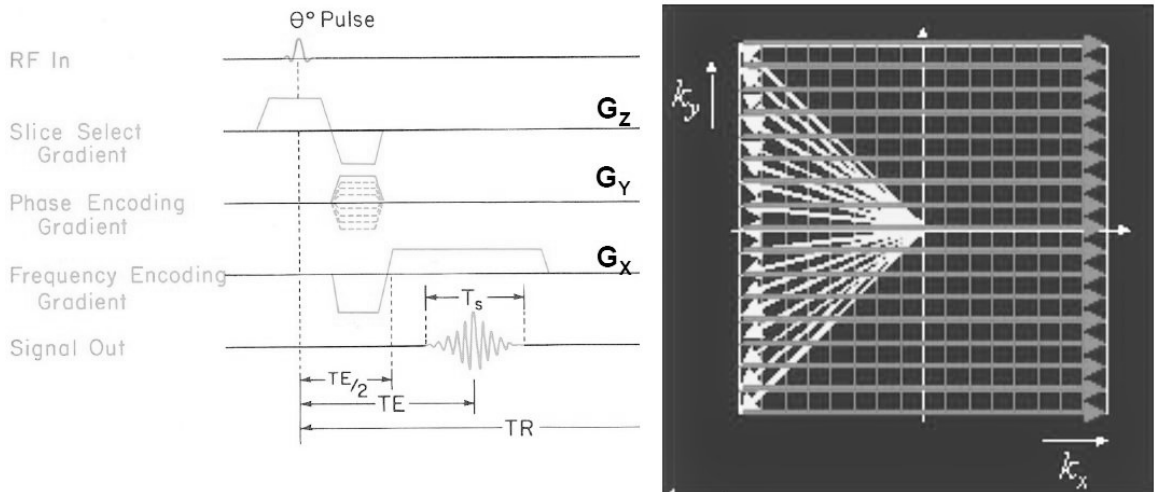
Figure 2.2: Cartesian-based K-space Trajectory [image courtesy of Stark and Bradley (1991)]

Through use of the FT, the resultant image's field of view (FOV) in the frequency encode direction can be related to the k-space sampling resolution:

$$FOV_x = \frac{1}{\Delta k_x} \tag{2.7}$$

The resolution in the frequency encode direction, Δx, can then be calculated as:

$$\Delta x = \frac{1}{N \cdot \Delta k_x} \tag{2.8}$$

with N denoting the number of samples in the frequency encode direction. Overall, these equations describe that in order to acquire higher resolution images a more comprehensive k-space sampling strategy is required.

Chapter 3

Background and Literature Review

3.1 Diffusion Tensor Imaging

3.1.1 Underlying mechanics

Diffusion weighted imaging (DWI) is an MR imaging method based on the water diffusion rate within tissues. DTI provides a quantitative method of modelling the DW-signal. The overarching concept behind DTI is that the diffusion of water molecules varies depending on the tissue type, architecture, and integrity (Beaulieu, 2002). Water mobility in tissues may not necessarily be the same in every direction. DTI is able to characterize the 3-dimensional diffusion of water as a means to quantify the microstructural integrity of white matter (WM) fibre tracts in the brain (Pierpaoli and Basser, 1996; Pierpaoli, 2001). Research from Pierpaoli and Basser (1996) suggests that within WM, water is able to diffuse more freely along the axon and is considered anisotropic whereas Gray Matter (GM) tends to be relatively less anisotropic. Diffusion within the Cerebrospinal fluid (CSF) is virtually unrestricted in all directions

and can be classified as isotropic.

For cases where diffusion is anisotropic, Basser *et al.* (1994a,b) found that diffusion could be mathematically represented by a 3×3 rank 2 tensor $\underline{\mathbf{D}}$ defined as

$$
\underline{\mathbf{D}} = \begin{vmatrix} D_{xx} & D_{xy} & D_{xz} \\ D_{yx} & D_{yy} & D_{yz} \\ D_{zx} & D_{zy} & D_{zz} \end{vmatrix} \tag{3.1}
$$

This tensor is symmetrical where $D_{ij} = D_{ji}$ with $i, j = x, y, z$. Referring to Figures 3.1 and 3.2, this diffusion tensor can also be modelled as an ellipsoid.
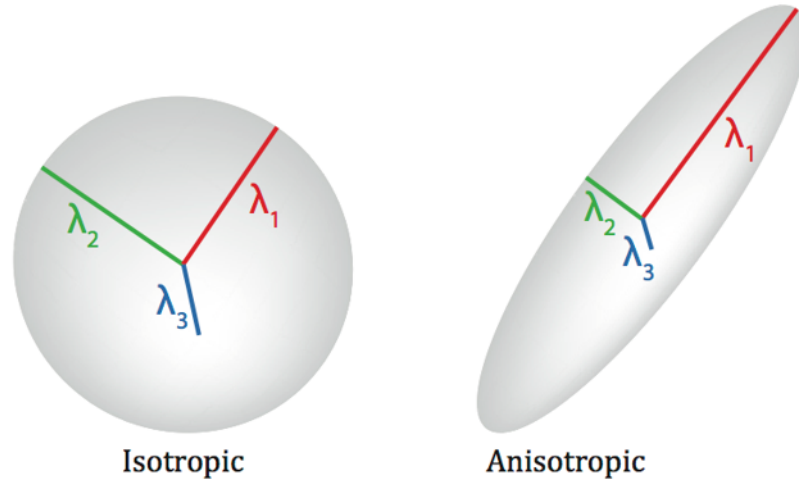
Figure 3.1: Diffusion Tensor modelling: anisotropic vs isotropic ellipsoids

Based on this model we can calculated voxel-wise tissue properties such as Mean Diffusivity (MD) or Apparent Diffusion coefficient (ADC), representing the molecular diffusion rate, as well as Fractional Anisotropy (FA), which measures the preferred direction of diffusion. FA is a dimensionless quantity and is defined as

$$FA = \sqrt{\frac{1}{2}} \frac{\sqrt{(\lambda_1 - \lambda_2)^2 + (\lambda_1 - \lambda_3)^2 + (\lambda_2 - \lambda_3)^2}}{\sqrt{\lambda_1^2 + \lambda_2^2 + \lambda_3^2}} \tag{3.2}$$

where λ_i is the ith eigenvalue from the diffusion ellipsoid model (Figure 3.1). In addition, both axial and radial diffusivity (AD and RD) can be inferred from DTI. AD represents the rate of diffusion along the main axis of diffusion whereas RD indicates diffusivity rates in the transverse plane. AD and RD are measured in units of mm^2/s and are defined below in equations 3.3 and 3.4, respectively:

$$AD = \lambda_1 \tag{3.3}$$

$$RD = \frac{\lambda_2 + \lambda_3}{2} \tag{3.4}$$

For the purposes of this thesis, the focus was given to FA, AD, and RD as a means to study the microstructure of various WM regions.
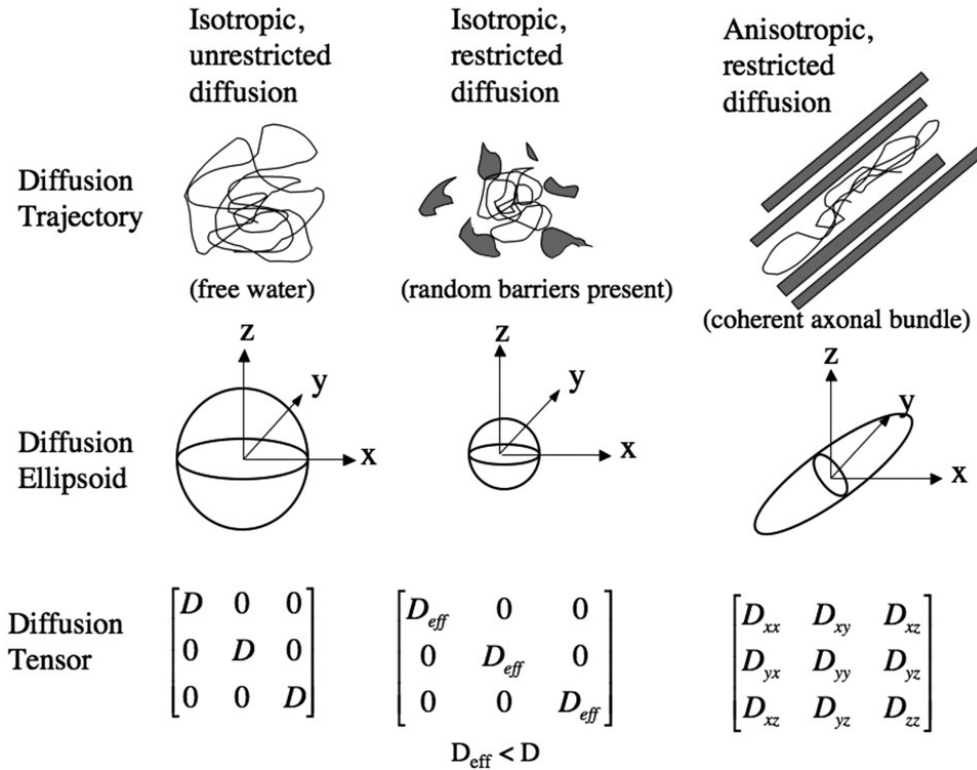
Figure 3.2: Diffusion Tensor modelling: relating increased presence of barriers to effective diffusivity [image published in American Journal of Neuroradiology (Mukherjee *et al.*, 2008). Permission to use this image included in Appendix E]

3.1.2   Relevant Studies

As previously explained, a reduction of white matter integrity is considered to be a key indicator of mTBI (Arfanakis, 2002) and generally is not detected with conventional T1 or T2-weighted MR imaging (Hughes, 2004b). DTI metrics such as FA, AD, and RD can be used to quantify the degree of diffusion anisotropy as well as the overall magnitude of diffusivity, respectively, within each voxel. In general, damaged white matter exhibits lower FA and increased MD compared to healthy myelinated WM (Yuh *et al.*, 2014). An increase in MD can be attributed to an increase in

AD and/or RD. Many methods based on the DTI protocol (Tuch, 2002) have been proposed in order to extract more information from the diffusion-weighted (DW) signal. Essentially, this can be accomplished by using a greater number of gradient directions to evaluate the higher angular frequencies that are not modelled effectively with a single tensor.

In patients with TBI, specific tracts of interest include the corpus callosum, longitudinal fasciculus, forceps major and minor, corona radiate, cingulum bundle, and uncinate fasciculus (Niogi *et al.*, 2008; Rutgers, 2008; Morey, 2013). A number of studies have been performed to analyze the usefulness of DTI in TBI patients. Some studies looking at pediatric mTBI cases have shown that the degree of axonal injury across a wide range of WM is correlated to impaired executive function (Wozniak, 2007; Dennis, 2015). Another study from Lipton *et al.* (2009) found that lowered executive function after mild TBI was related to axonal injury within the dorsolateral prefrontal cortex. In general, in TBI studies where patients were scanned a minimum of 2 weeks post-injury there was an observed increase in MD or a reduction in FA, or both (Inglese, 2005; Smits, 2011; Cubon, 2011; Messe, 2011). However, some null DTI results following mTBI were also reported suggesting that the severity of the injury can greatly affect the degree of change in DTI measures (Sharp and Ham, 2011).

Further work undertaken by Caeyenberghs *et al.* (2011a,b) looked at the consequences of TBI on motor function in adults. A substantial decrease in FA and increase in radial diffusivity were observed in TBI subjects compared to controls. Further, their results suggest that structural changes in various subregional callosal fibres coincided with differential behavioral manifestations of bimanual motor functioning.

Longitudinal studies from Mayer (2010) suggested that partial normalization of

DTI values may occur in several WM tracts following mTBI. In addition, observed WM abnormalities indicated that cytotoxic edema may exist during the semi-acute phase of mTBI. As a result of the initial mechanical damage to axons, ionic homeostasis is disrupted thereby affecting diffusion perpendicular to the axons. This work shows that DTI measures could potentially serve as biomarkers of recovery following TBI.

Recent work from Laitinen *et al.* (2015) used TBI rat models to investigate secondary injury detection at a chronic time point using ex vivo DTI. The DTI results showed microstructural changes in WM within the corpus callosum, angular bundle, and internal capsule. Further, histological examination confirmed that these changes mainly resulted from the loss of myelinated axons and iron accumulation. Interestingly, there was an increase in FA within areas of gray matter (GM) in the thalamus after TBI. This may have been related to neurodegeneration, loss of myelinated fibres, and calcification occuring in the chronic phase of TBI.

Research from Morey (2013) investigated the effects of chronic mTBI on WM integrity in war veterans. As a caveat, it should be noted that it is difficult to differentiate chronic mTBI from post-traumatic stress disorder (PTSD) and depression as there are a number of overlapping behavioral symptoms. However, the results did suggest that a reduction in WM integrity in primary fibres correlated with chronic mTBI in major fibre bundles and smaller peripheral tracts including the corpus callosum and longitudinal fasciculus. Additionally, the loss in WM integrity was found to be associated with duration of loss of consciousness and feelings of dizziness.

Overall, DTI has proven to be more sensitive relative to conventional imaging methods in detecting subtle microstructural changes following TBI. As a result, this

imaging technique may provide an enhanced method of diagnosis, prognosis, and management of TBI patients. Beyond DTI there are other analysis methods known as high angular resolution diffusion imaging (HARDI) as well as q-space which assumes there is a Fourier relationship between the spin displacement probability density function and the DW signal over DW gradient amplitude vectors. Though q-space provides precise results, it also requires exceptionally long scan times in order to acquire the necessary data.

3.2   Quantitative Susceptibility Mapping

3.2.1   Underlying Mechanics

Susceptibility weighted imaging is a velocity-compensated 3D gradient echo imaging technique that is able to utilize phase as a means to enhance T2* contrast and examine magnetic susceptibility of tissues (Haacke, 1995, 2004; Reichenbach, 1997, 1998, 2000). Magnetic susceptibility is a dimensionless proportionality constant that indicates the degree of magnetization of a material in response to an applied magnetic field. At adequately long echo times, tissue signals will become out of phase relative to their neighbouring tissues with different magnetic susceptibilities. The iron, calcium, lipid, and myelin content are what provides the main source of phase contrast in tissues (Haacke, 2005, 2007, 2009; Fatemi-Ardekani *et al.*, 2009; Lee, 2009; Xiang and Yablonskiy, 2009). The MR signal magnitude of phase of the venous structure within the brain is dependent on the deoxyhemoglobin level. The amount of deoxyhemoglobin can be related to oxygen saturation which, in turn, can be used to assess

changes in blood flow (Suskauer and Huisman, 2009; Akiyama, 2009). Due to its sensitivity to deoxygenated blood and intracranial mineral deposition, SWI has proven useful when imaging various pathologies such as intracranial hemorrhage, traumatic brain injury, stroke, neoplasm, and multiple sclerosis. The one drawback of SWI is that it only provides a qualitative measure of magnetic susceptibility. This limitation has been addressed with the development of quantitative susceptibility mapping (QSM).

MR exams generate both a magnitude and phase image (Figure 3.3). In most cases, only the magnitude is considered for further analysis whereas QSM uses both the magnitude and filtered phase image data to improve image contrast. Postprocessing can be applied to the magnitude volume through a phase mask to enhance or, in some cases, suppress spectral components.

(a) Magnitude data   (b) Phase data
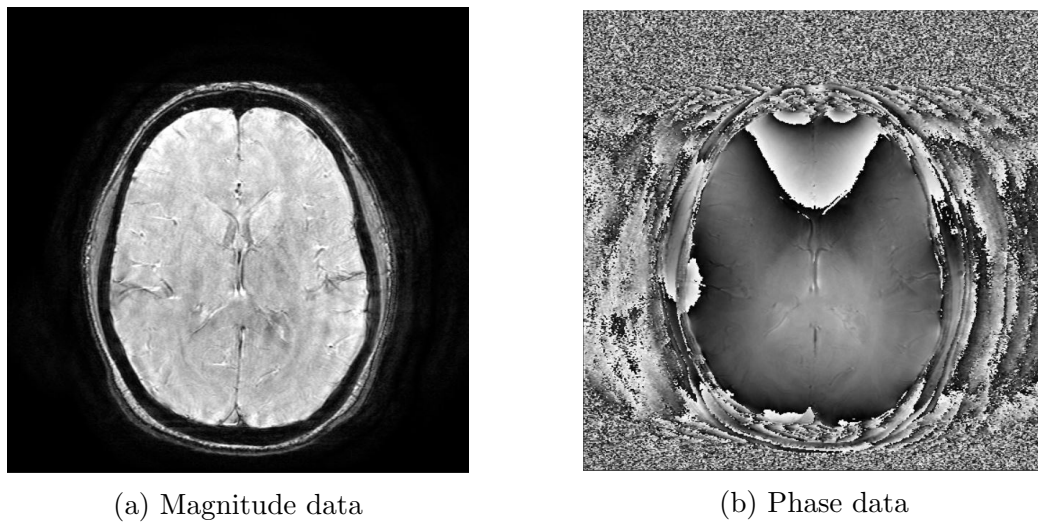
Figure 3.3: Raw MRI Magnitude and Phase volumes

As previously mentioned magnetic susceptibility is defined as the magnetic response of a substance when placed in an external magnetic field. The induced magnetization B is found to be directly proportional to the main magnetic field M and is defined as

$$B = \chi M \qquad (3.5)$$

where χ is the magnetic susceptibility of the tissue. In general, $\chi > 0$ for diamagnetic materials such as calcium and $\chi < 0$ for paramagnetic materials such as iron. As a reference, deoxygenated blood has a $\Delta\chi = 0.45 ppm$ relative to its surrouding tissue. This equates to approximately 120μg of iron per gram of tissue.

As described by Haacke (2004), B will cause distortions to the field surrounding an object within a uniform M. These localized field deviations produce the local phase differences observed in the MR images. Phase, ϕ, is defined as

$$\phi = -\gamma(\Delta B_{lg} + \Delta B_{cs} + \Delta B_{gg} + \Delta B_M)TE \qquad (3.6)$$

where $\gamma = 2.67 \times 10^8 rad/(s \cdot T)$ represents the gyromagnetic ratio for protons, ΔB_{lg}, ΔB_{cs}, ΔB_{gg} and ΔB_M are the changes in induced magnetization cause due to local geometry, chemical shift, global geometry and the main magnetic field, respectively. ΔB_{gg} and ΔB_M both exhibit a lower frequency dependence and thus are removed using a high pass filter.

After performing phase unwrapping and background field removal, the next step is to merge the magnitude and filtered phase images to generate a SW image. A phase mask is used in order to enhance the contrast in the original magnitude image. This phase mask, $f(x)$, is designed as a decimal value within each voxel and is constrained

such that $0 \leq f(x) \leq 1$. Essentially, the value for each voxel can be set at $f(x) < 1$ in order to suppress the signal intensity within a particular region. As an example, if the minimum phase of interest is $-\pi$, the phase mask would be designed as

$$f(x) = \begin{cases} \frac{\phi(x)+\pi}{\pi}, & \text{if } -\pi < \phi(x) < 0 \\ 1, & \text{otherwise} \end{cases} \tag{3.7}$$

where $\phi(x)$ represents the phase measured in voxel x (Haacke et $al.$, 2009).

The original magnitude image $p(x)$ is then multipled by the phase mask to generate an image $p^m(x)$ with a new contast:

$$p^m(x) = f^m(x)p(x) \tag{3.8}$$

where m denotes the number of phase mask multiplications. Generally, $m = 4$ is chosen in order to optimize the contrast-to-noise ratio (CNR). Figure 3.4 provides a visual reference of this process. Note that when $m = 4$, the veins with $\phi(x) = -\frac{\pi}{2}$ have a corresponding $f^m(x) = 0.0625$ which is virtually identical to the phase mask intensity value of the $\phi = -\pi$ veins.
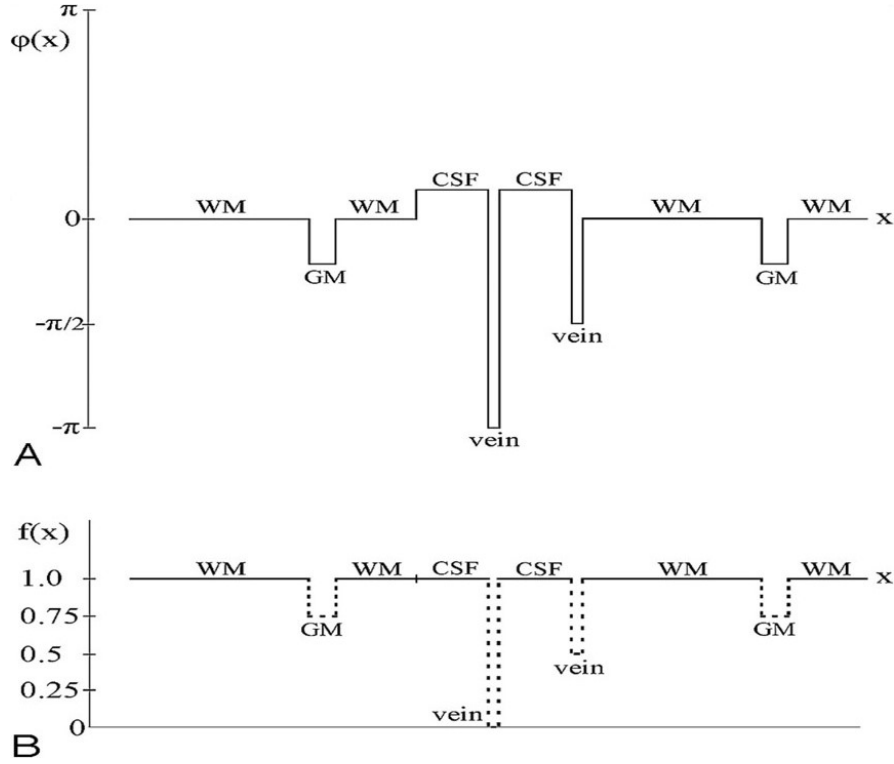
Figure 3.4: Phase masking process: (A) Phase profile in filtered phase image. (B) corresponding intensity profile of phase mask [image published in American Journal of Neuroradiology (Haacke *et al.*, 2009). Permission to use this image included in Appendix E]

In order to map susceptibility for QSM, the following equation must be solved (Liu *et al.*, 2015a):

$$f(\mathbf{k}) = \gamma B_0 (\frac{1}{3} - \frac{k_z^2}{k^2})\chi(\mathbf{k}) \tag{3.9}$$

where $\mathbf{k}$ is the k-space vector, k_z is its z-component; $f(\mathbf{k})$ is the FT of $f(x)$; B_0 is the induced magnetization corresponding to the applied magnetic field M; $\chi(\mathbf{k})$ is the FT of $\chi(x)$; and γ is the gyromagnetic ratio constant. In this case, $f(k)$ is the experimental measurement and we are solving for $\chi(\mathbf{k})$.

3.2.2 Relevant Studies

In cases of TBI, SWI is able to detect extravascular blood products; a common result of shearing injury (Liu *et al.*, 2015b). Research by Akiyama (2009) compared SWI relative to conventional MR imaging techniques in terms of its ability to detect cerebral hemorrhages in patients with TBI. SWI detected an average of 76+/-52 hypointense lesions relative to 21+/-19 observed by T2*-weighted imaging suggesting that SWI is an extremely sensitive method for visualizing microhemorrhages. Additionally, research has suggested that SWI is also able to differentiate, with reasonable accuracy, hemorrhages from deep veins in TBI patients (Liu *et al.*, 2015b).

Further, work from Tong (2004) looked at correlating the degree of diffuse axonal injury to clinical variables such as Glasgow Coma Scale (GCS) score as well as coma duration. The results showed that subjects with a lower GCS score or coma lasting longer than four days had a greater number and volume of hemorrhagic lesions. However, another study by Doshi *et al.* (2015) found no correlation between susceptibility measures and symptoms assessed by neuropsychological testing. One drawback with SWI is that it is only able to provide qualitative information. That has been addressed with the advent of Quantitative Susceptibility Mapping (QSM). Overall, studies have shown that QSM is able to visualize and quantify micro bleeds in cases of TBI and can also be an effective means to evaluate longitudinal changes (Wang, 2014; Lin *et al.*, 2014; Liu *et al.*, 2014; Haacke *et al.*, 2015).

Chapter 4

Methods and Materials

4.1 Study Overview

4.1.1 Participant Recruitment and Monitoring

Pediatric patients recently diagnosed with mTBI and between the age of 10 and 17 were recruited in collaboration with the Back to Play study, led by Dr. Carol DeMatteo. The goal was to perform an MRI scan on each participant as soon as possible after the initial injury and then schedule one or two additional follow up scans at either the three-month mark or after the participant's symptoms had resolved (depending on which occured first). These follow up scans would provide a reference for longitudinal analysis to determine if an observed change could be seen on the MR images for each individual. Due to scheduling conflicts and participant drop-outs midway through the study, only a small portion returned for at least one follow up scan. In total, 26 subjects successfully completed their initial MRI scan with seven returning for a follow up scan (all post-symptom resolution) and two returning for

a third and final scan. The average age of the participants was 13.8 ± 2.61. Of the participants, 16 were female and 10 were male.

At the time of scanning, each participant was asked to complete a Post Concussion Symptom Scale (PCSS) to assess their symptom severity. The PCSS score provides a general means to quantify the symptom severity for a given individual. The score can range from 0 to 132 with higher scores indicating greater symptom severity. The average PCSS score for the 26 preliminary scans was 17.74 ± 17.16, with a minimum score of 2 and a maximum of 68. For the nine follow-up scans, the average PCSS score was 8.44 ± 11.01, with a minimum score of 0 and a maximum of 33.

Subjects were monitored for concussive symptoms and asked to self-report their symptom severity through PCSS surveys every 48 hours until symptom resolution. The participant was deemed to have reached symptom resolution after scoring 0 on two sequential PCSS surveys, meaning that they had not experienced any symptoms over a 96-hour (4-day) period. The subjects were then divided into three mutually exclusive groups based on time to symptom resolution:

- Stratum 1: recovery within 14 days of injury

- Stratum 2: recovery between 15 and 28 days post-injury

- Stratum 3: recovery greater than 28 days post-injury

In the end, only one participant achieved symptom resolution within 14 days, whereas eight participants reached symptom resolution between 15 and 28 days and 17 participants had their symptoms resolve after 28 days. Refer to Table 4.1 for further details pertaining to each participant.

Table 4.1: General Participant Information

Pt. #	Gender	Age	Date of Injury	Date of Symptom Resolution	Stratum	Scan 1 Date	PCSS	Scan 2 Date	PCSS (2)	Scan 3 Date	PCSS (3)
1	M	13	2015-06-01	2015-06-17	2	2015-06-12	5	2015-09-02	0	---	---
2	F	11	2015-07-13	2015-08-09	2	2015-07-23	17	---	---	---	---
3	F	10	2015-03-31	2015-05-11	3	2015-08-20	8	---	---	---	---
4	M	10	2015-08-11	2015-09-04	2	2015-08-28	14	---	---	---	---
5	F	15	2015-09-05	2015-11-24	3	2015-09-24	30	2015-12-21	15	2016-02-16	16
6	F	15	2015-10-15	2015-11-05	2	2015-10-30	45	---	---	---	---
7	M	10	2015-10-20	2015-11-11	2	2015-11-03	13	2016-02-01	2	---	---
8	F	17	2015-05-09	2015-11-14	3	2015-11-10	10	2015-12-15	3	2016-02-09	5
9	F	14	2015-10-28	2016-05-19 ††	3	2015-11-12	68	---	---	---	---
10	F	16	2015-10-28	2015-11-25	3	2015-11-24	2	2016-04-07	2	---	---
11	F	16	2015-05-13	2016-03-02	3	2015-11-25	27	---	---	---	---
12	F	14	2015-11-01	2016-02-05	3	2015-12-04	57	2016-04-15	33	---	---
13	M	10	2015-07-15	2016-05-19 ††	3	2015-12-08	5	---	---	---	---
14	M	16	2015-11-21	2016-01-09	3	2015-12-11	2	2016-03-29	0	---	---
15	M	16	2016-01-07	2016-02-08	3	2016-01-28	27	---	---	---	---
16 †	M	11	2016-01-03	2016-01-30	2	2016-02-03	2	---	---	---	---
17	F	16	2015-10-29	2016-05-19	3	2016-02-04	16	---	---	---	---
18	F	16	2016-01-14	2016-02-03	2	2016-02-10	3	---	---	---	---
19	M	12	2016-01-12	2016-05-19	3	2016-02-18	36	---	---	---	---
20	M	17	2016-02-15	2016-03-19	3	2016-02-18	15	---	---	---	---
21 †	F	15	2016-02-02	2016-03-02	3	2016-02-29	11	---	---	---	---
22	F	15	2016-01-03	2016-05-19 ††	3	2016-02-29	11	---	---	---	---
23	F	10	2016-02-03	2016-02-19	2	2016-03-03	2	---	---	---	---
24	F	14	2016-02-14	2016-05-19 ††	3	2016-03-23	25	---	---	---	---
25	M	10	2016-02-10	2016-02-23	1	2016-04-22	8	---	---	---	---
26	F	16	2015-10-10	2016-05-19 ††	3	2016-04-22	17	---	---	---	---

† denotes that there were errors in the QSM imaging t and only DTI was used for analysis for this patient

†† denotes that symptom resolution had not yet been achieved as of 2016-05-19

Further, 49 age-matched healthy control subjects were also included in this study in order to provide a means of comparison between a healthy sample population relative to the mTBI group. Control DTI data used in the preparation of this thesis was obtained from the Pediatric MRI Data Repository created by the NIH MRI Study of Normal Brain Development. This is a multi-site, longitudinal study of typically developing children, from ages newborn through young adulthood, conducted by the Brain Development Cooperative Group and supported by the National Institute of Child Health and Human Development, the National Institute on Drug Abuse, the National Institute of Mental Health, and the National Institute of Neurological Disorders and Stroke (Rivkin *et al.*, 2007).

4.1.2   MRI Data

Data for mTBI patients was collected using the Research-dedicated 3-Tesla GE Discovery MR750 MRI scanner at the Imaging Research Centre of St. Joseph's Healthcare, Hamilton. For this study, the 32-channel Head and Neck coil was used for image acquisition. Each subject underwent the same protocol which included the following scans:

- 3D Anatomical

- Axial Susceptibility Weighted Imaging (SWI) scan

- Three separate Diffusion Tensor Imaging (DTI) scans with 19, 20, and 21 tensor directions respectively

- Two B0 maps with TE of 5 ms and 8 ms respectively

It is worth noting that the SWI scan used a TE of 20 ms and flip angle of 15° in order to achieve adequate contrast between the different brain tissues. Further, the DTI portion of the protocol was split into three separate scans for the purpose of mitigating potential time losses. Since this study involved relatively young pediatric subjects, there was a high likelihood that they would shift around while in the MRI thus creating motion artifacts on the images. By splitting the DTI scan into three separate scans the time was shortened and a single scan could easily be repeated if there was excessive movement. As explained later on in this thesis, the three scans were then concatenated to form a single merged 60-direction DTI scan to be used for analysis. The data contained 12 b=0 volumes and 60 b=1000 s/mm^2 volumes for a total of 72 images per slice. Refer to Appendix A for the 60-direction tensor file used for acquiring the DTI data. For each of the three scans TE=87ms and flip angle=90° were used and prescan values were not changed.

As for the control dataset, downloaded from the NIH database, the DTI scans were performed on GE MRI Scanners with different parameters compared to the mTBI data. Overall, 50 unique diffusion-encoding gradients were acquired in the scan at b=1100 s/mm^2 with 9 b=0 volumes for a total of 59 volumes. Though the parameters are different, studies from Lebel *et al.* (2012) have shown that diffusion schemes with different number of diffusion-encoding gradients were able to produce similar quantitative results and thus can be used for drawing comparisons.

4.2   Processing Steps

4.2.1   mTBI Data

Diffusion Tensor Imaging

The majority of data processing for the DTI images was performed using FSL (Woolrich *et al.*, 2009; Smith *et al.*, 2004; Jenkinson *et al.*, 2012). Prior to analysis, each DTI acquisition had all DICOM images concatenated into a NIfTI file format. Figure 4.1 shows the major processing steps from the raw DTI images to the fully processed FA, RD, and AD images which were used for quantitative analysis.
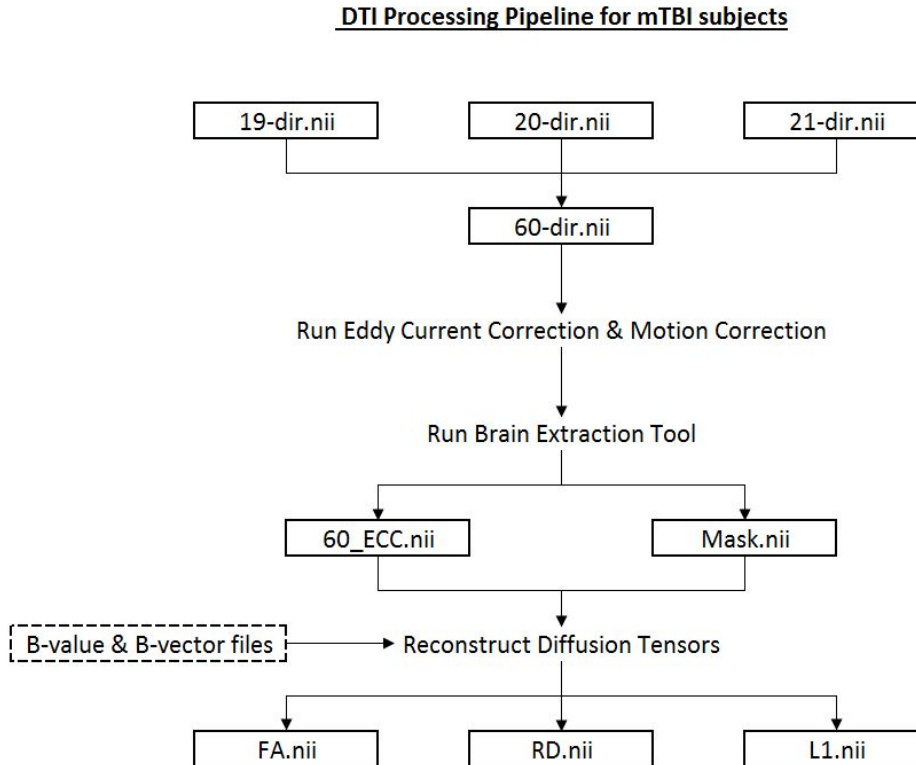
Figure 4.1: Processing Pipeline for mTBI data showing major steps from the raw DTI image files to the fully processed FA, RD, and AD (λ_1) images

As previously mentioned, after acquiring the raw DTI images for 19, 20, and 21-directions, the files must be merged to form a single DTI file with 60 unique tensor directions. Each raw DTI file contained $n + 4$ volumes, where n represents the number of diffusion directions. So the 19-direction contains 23 volumes; 19 unique DTI vectors and four embedded b=0 images. Volumes from all three raw files were split and then concatenated to form the complete 60-direction DTI image comprised of 72 total volumes including 12 b=0 volumes organized at the start as opposed to embedded within the file. This order was important to perform further processing steps. Figure 4.2 shows example images of brain volumes at b=0 and b=1000.

(a) B0 volume   (b) B=1000 volume
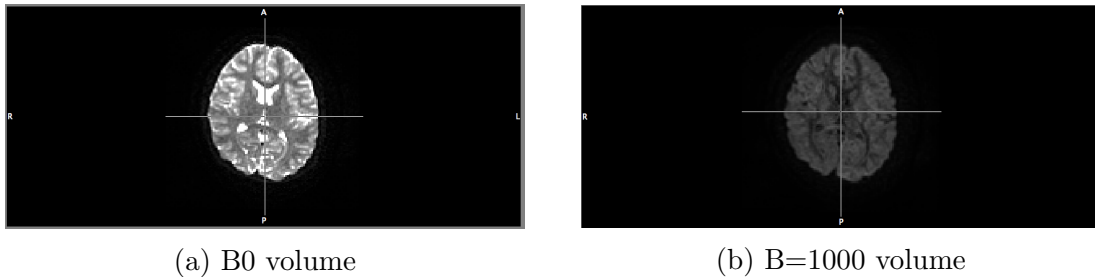
Figure 4.2: B=0 reference volume and B=1000 DTI volume for one of the 60 unique tensor directions

The next step was to perform eddy current and motion corrections as well as to correct for fieldmap (EPI) distortion. As explained by Faraday's law of induction, changing magnetic fields within conductors induce circular electric currents known as eddy currents. During the acquisition of diffusion images, artifacts such as shear, image intensity loss, and image blurring may occur in different gradient directions. EPI distortions are the result of inhomogeneities in the applied magnetic field. Signal loss and geometric distortions can occur due to these inhomogeneous fields affecting the spatial encoding gradients. Through affine registration to a reference volume, the

29

FSL tool 'Eddy' (Andersson and Sotiropoulos, 2016) was able to correct for these distortions in addition to moderate head motion.

Afterward, FSL Brain Extraction Tool (BET) (Smith, 2002) was run in order to remove the skull and optic nerves from the Eddy-current corrected image and produce a binary brain mask for the next step in the process. After trial and error a threshold value of 0.3 was selected to ensure that no parts of the brain were accidentally removed during the BET processing. Figure 4.3 shows the graphic user interface for FSL BET as well as the outputted binary brain mask.
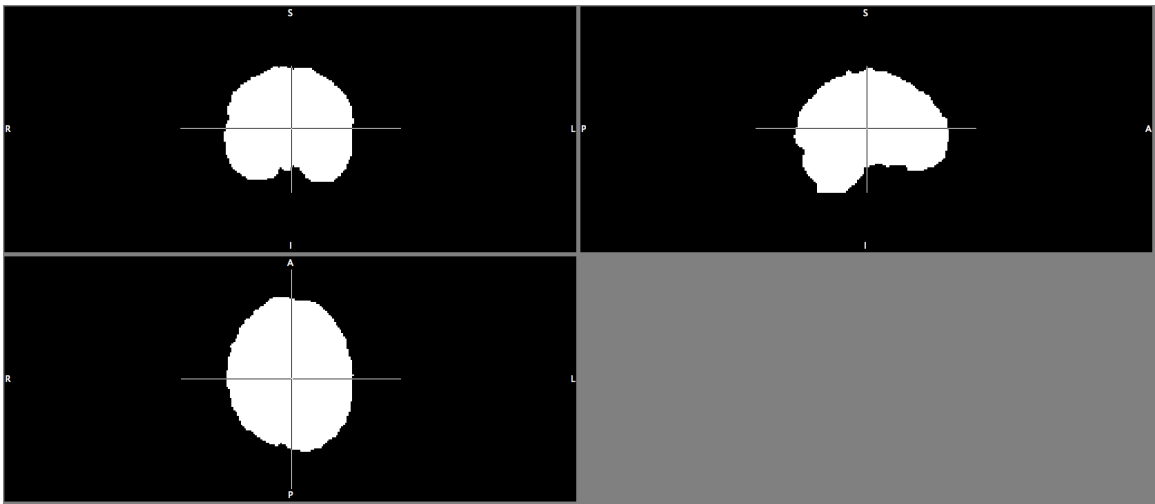
Figure 4.3: BET Processing: Resultant binary brain mask

Using this newly processed BET brain mask, the diffusion tensors were reconstructed using DTIFit in FSL Diffusion Toolkit (FDT) (Behrens *et al.*, 2003, 2007). The program takes the input diffusion images and, referencing the mask and diffusion directions, calculates the tensor for each voxel that falls within the mask. Additionally, two files are needed which specify the b-values and b-vectors for each of the 72 image volumes in the 60-direction DTI file. These tensor files were created by reordering the original three tensor files (from the raw 19, 20, and 21-direction DTI

data) so that they coincided with the volumes in the concatenated 60-direction DTI image. The b-value and b-vector matrices are available for reference in Appendix A. The final output images from DTIFit included Fractional Anisotropy, Eigenvalue, and Eigenvector images. The Eigenvalues were used to compute Radial Diffusivity. For the purposes of this thesis, only FA, AD (λ_1), and RD files were considered for structural analysis. Figure 4.4 shows examples images for FA, RD, and AD volumes which were used for analysis.

(a) FA volume

(b) RD volume

(c) AD (λ_1) volume
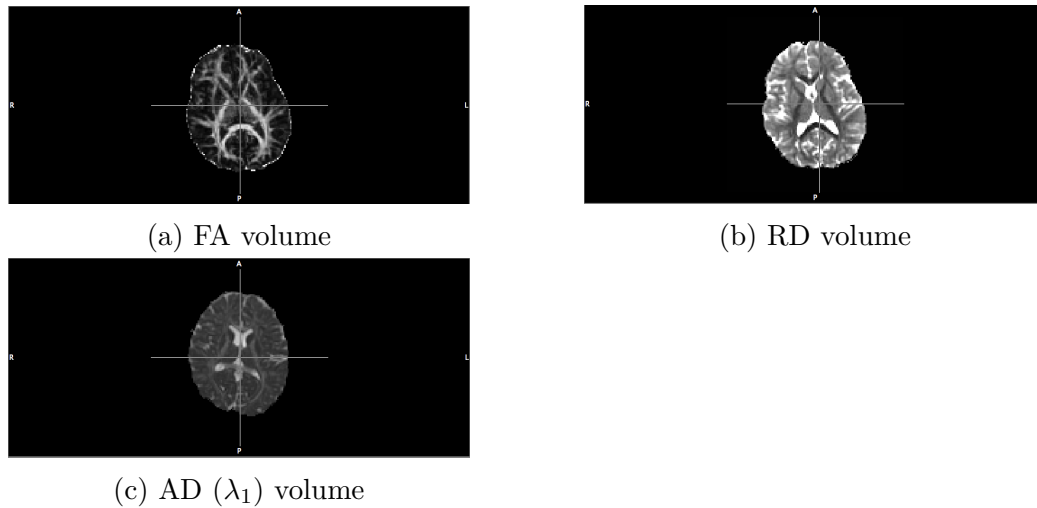
Figure 4.4: DTI Metrics: FA, RD, and AD volumes computed using FSL Diffusion Toolkit

Quantitative Susceptibility Mapping

The majority of processing was performed using a combination of FSL and STISuite (Liu, 2010), which runs through a MatLab interface. Figure 4.5 shows the pipeline for processing the raw SWI magnitude and phase images to generate the fully processed QSM image.

QSM Processing Pipeline for mTBI Subjects
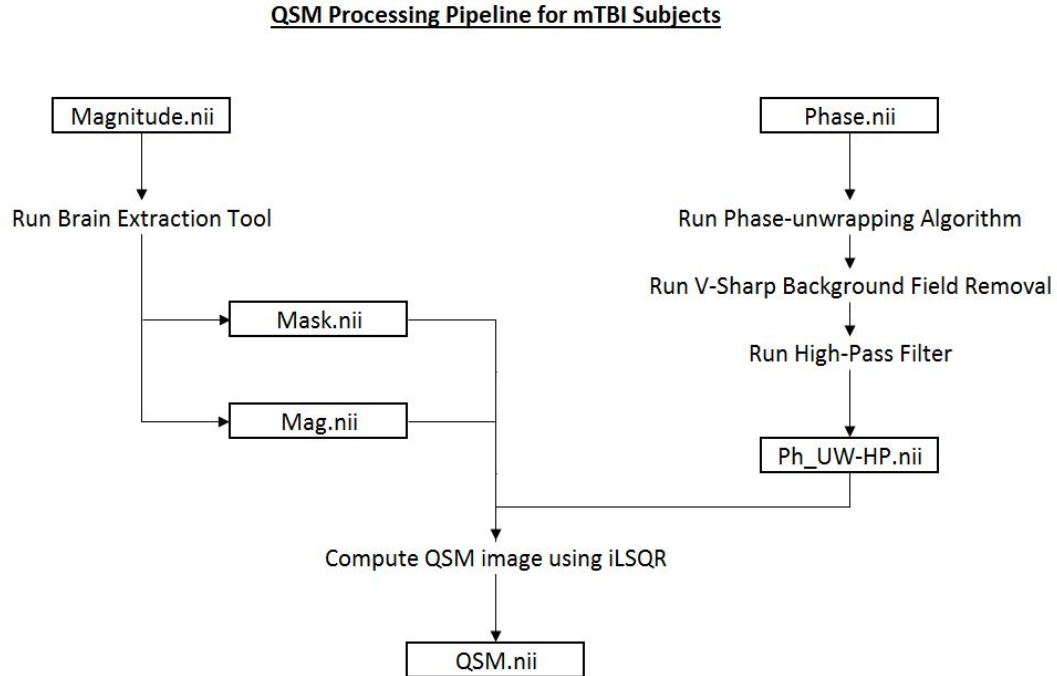
Figure 4.5: Processing Pipeline for mTBI data showing major steps from the raw magnitude and phase image files to the fully processed Quantitative Susceptibility Map image

The first step was to separate the raw SWI data into two separate volumes containing magnitude and phase information respectively (see Figure 4.6). This was accomplished using the 'fslsplit' command line function in FSL. Next, the magnitude volume was run through the FSL BET function (Smith, 2002) to produce a binary brain mask similar to Figure 4.3. A 32×32 high-pass filter was also applied to the phase volume in order to remove the lower-frequency components. The magnitude, phase, and brain mask volumes were then imported into STISuite for further processing.

(a) Magnitude volume   (b) Phase volume
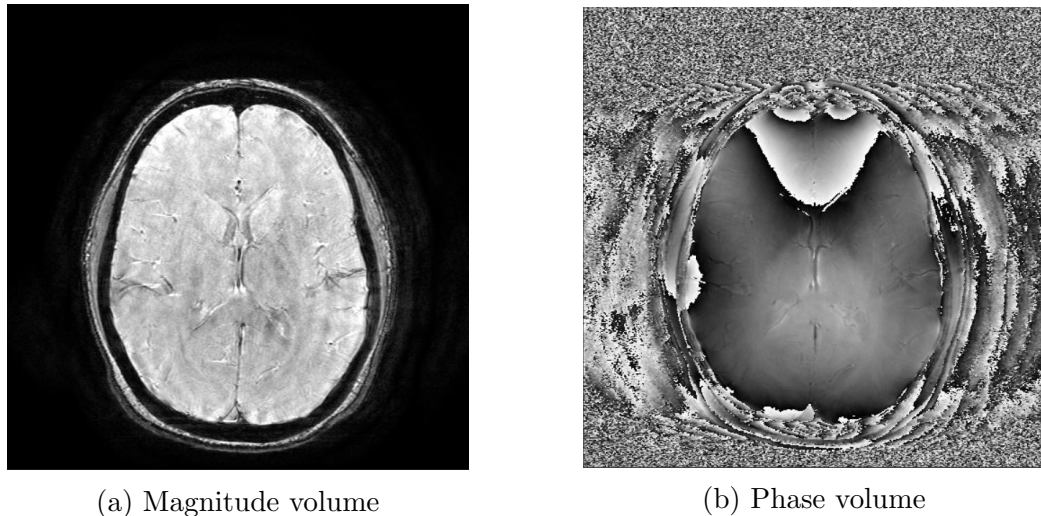
Figure 4.6: Raw SWI Magnitude and Phase Volumes

Within STISuite (Advanced options), the phase volume was scaled to 2π and the scan parameters were then confirmed. The TE was set to 20 ms and voxel size was set to [0.4688, 0.4688, 2.000]. Laplacian-based phase unwrapping algorithm was then applied to the phase volume to achieve 3D phase unwrapping (Li *et al.*, 2011; Wu *et al.*, 2012). This was followed by background field removal using the V-SHARP command. V-SHARP is a modified version of the SHARP method which uses a varying spherical kernel to remove the background phase and preserve contrast near the boundary of the brain (Schofield and Zhu, 2003; Schweser *et al.*, 2010). Lastly the QSM volume was produced using initial least square regression (iLSQR), a method of regression analysis used to approximate the solution for overdetermined systems (ie. there are more equations than unknowns). As shown in Figure 4.7, this process outputs the final QSM image which provides a quantitative measure of magnetic susceptibility within the brain.
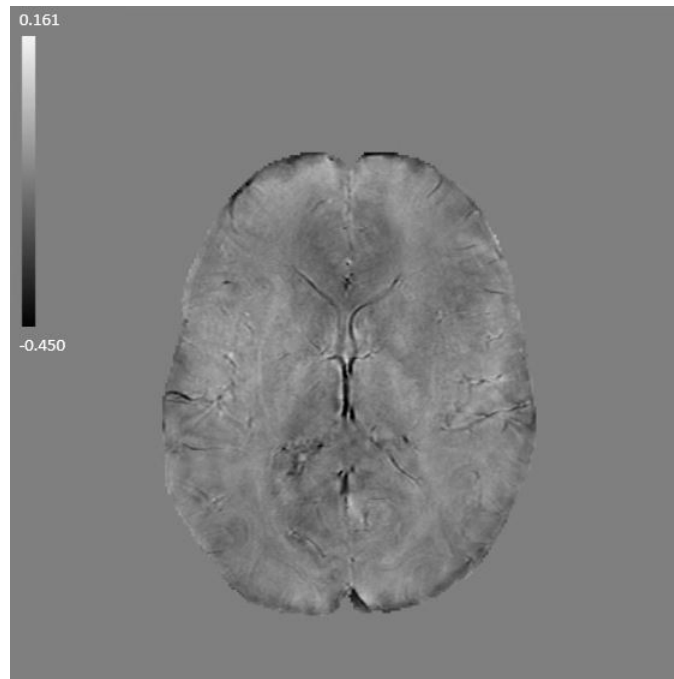
Figure 4.7: QSM processed in STISuite using the iLSQR method (susceptibility measured in ppm)

4.2.2 Control DTI Data

The same process pipeline was used as illustrated in Figure 4.1 except that the raw images were collected in a single file as opposed to three separate files. Therefore there was no need to reorganize and concatenate the images as was the case for the mTBI data. The final output was the FA, RD, and AD images to be used for comparison with the mTBI subject group.

4.2.3 Processing Regions of Interest

The effects of mTBI on specific brain regions were investigated in order to determine which areas were significantly impacted. In order to extract information from each

region, every single fully processed image had to be registered to standard brain space in order to apply a brain mask over the areas of interest to extract data solely from that particular ROI. Brain registration was accomplished using FSL Flirt. The MNI standard-space T1-weighted average structural template image was chosen for this study. This brain was supplied by Andrew Janke and is derived from the average of 152 structural images registered into the MNI co-ordinate system (Jenkinson and Smith, 2001; Jenkinson *et al.*, 2002; Greve and Fischl, 2009).

This study considered 24 unique regions of interest (ROI) within the brain for analysis. Within FSLView, each ROI was obtained from either the Juelich Histological Atlas (Eickhoff *et al.*, 2005, 2006, 2007) or the JHU DTI-based WM Atlas (Mori and Wakana, 2005; Wakana and Mori, 2007; Hua, 2008). The voxels in the ROI images had a value of 0 to 100 representing the probability that the respective voxel was part of that brain region. The ROI was converted into a binary mask using a threshold value of 10 so that voxels with extremely low probabilities were not included in the analysis. After creating the 24 ROI masks, they were individually multiplied over each subjects' (both mTBI and control) FA, RD, AD, and QSM images. Figures 4.8, 4.9, 4.10, and 4.11 show each ROI that was processed using the aforementioned technique.

(a) Acoustic Radiation Left

(b) Acoustic Radiation Right

(c) Cingulate Gyrus Left

(d) Cingulate Gyrus Right

(e) Cingulum Left

(f) Cingulum Right
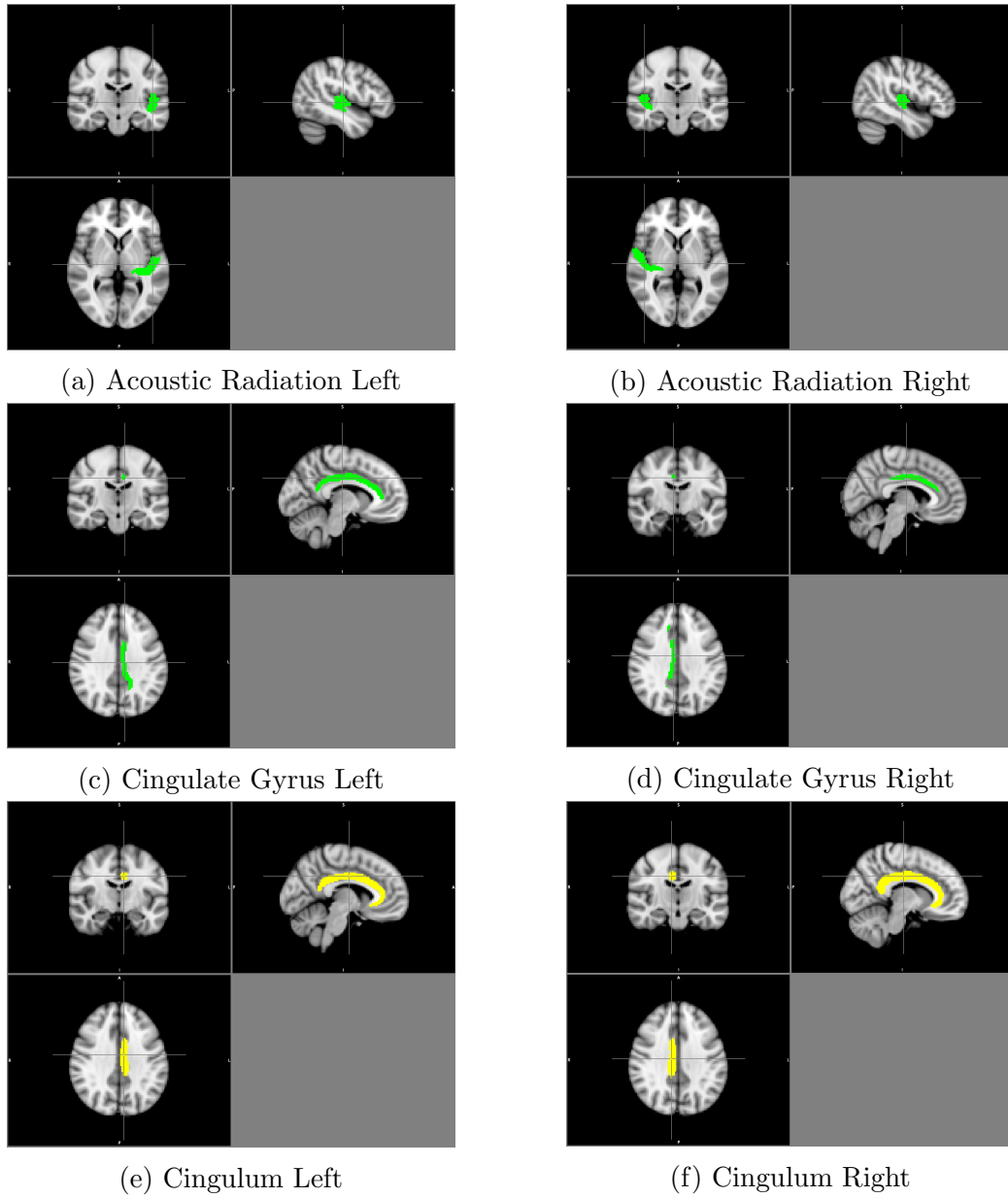
Figure 4.8: ROI Masks 1 through 6

(a) Corticospinal Tract Left

(b) Corticospinal Tract Right

(c) Corpus Callosum

(d) Fornix

(e) Forceps Major

(f) Forceps Minor
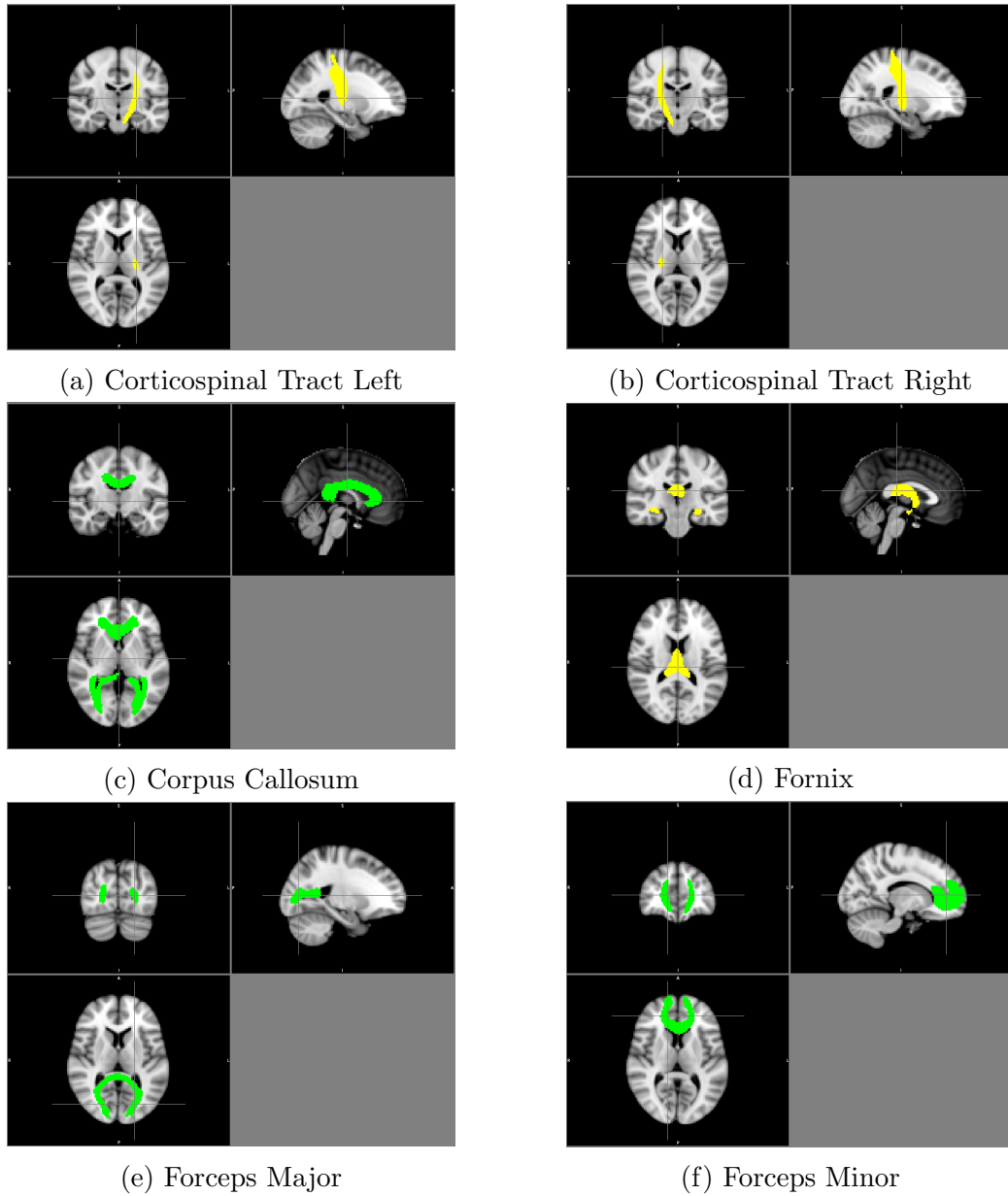
Figure 4.9: ROI Masks 6 through 12
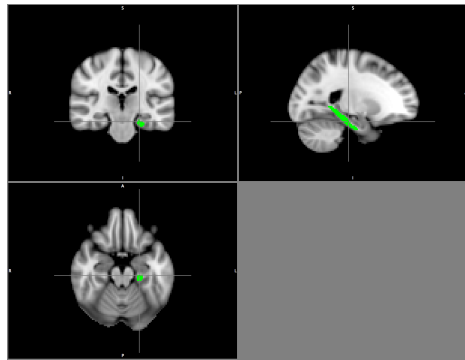
(a) Hippocampus Left
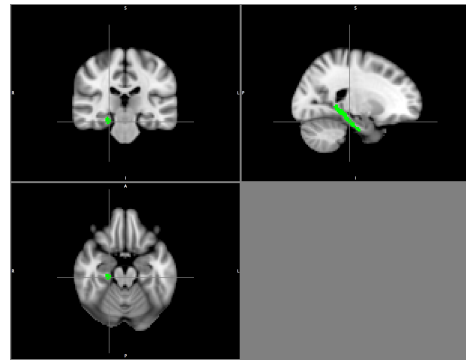
(b) Hippocampus Right
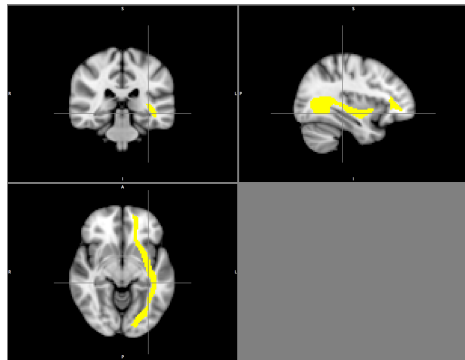
(c) Inferior Fronto-Occipital Fasciculus Left
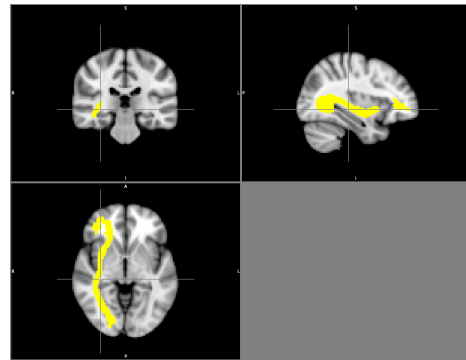
(d) Inferior Fronto-Occipital Fasciculus Right
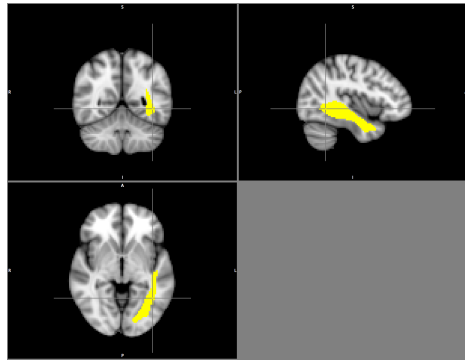
(e) Inferior Longitudinal Fasciculus Left
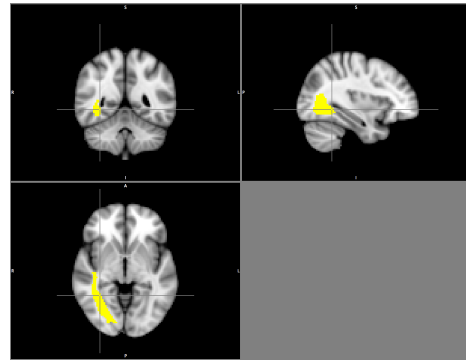
(f) Inferior Longitudinal Fasciculus Right

Figure 4.10: ROI Masks 13 through 18
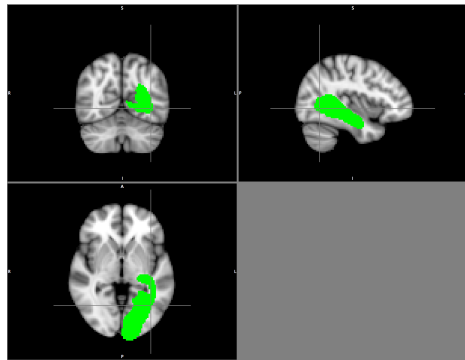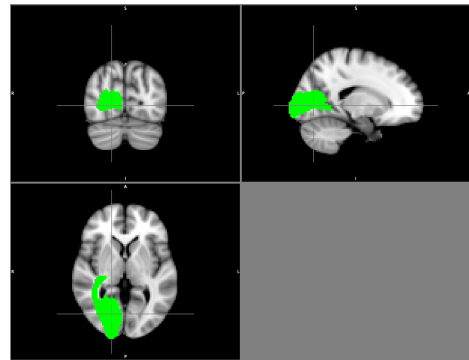
(a) Optic Radiation Left   (b) Optic Radiation Right
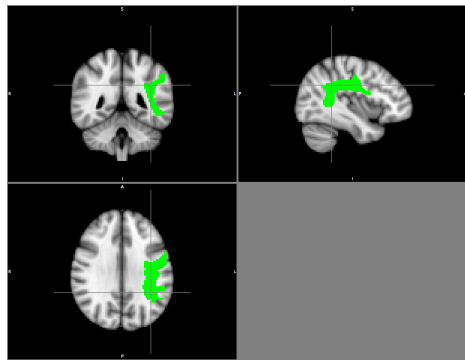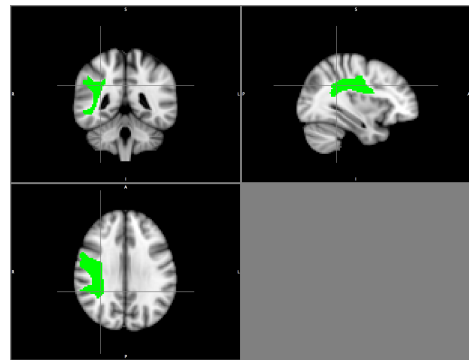
(c) Superior Longitudinal Fasciculus Left   (d) Superior Longitudinal Fasciculus Right
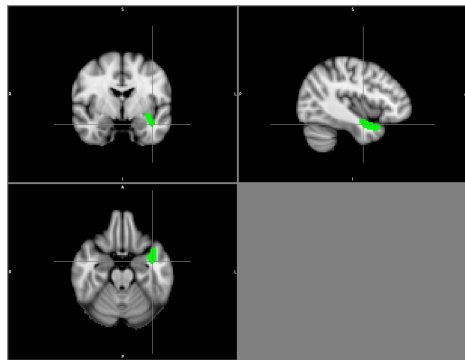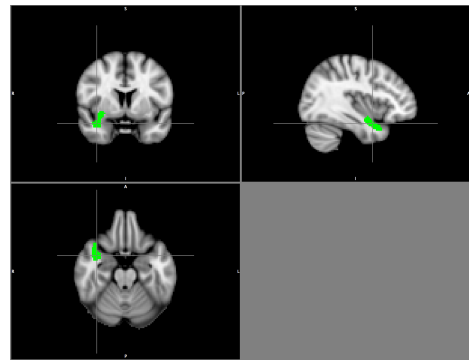
(e) Uncinate Fasciculus Left   (f) Uncinate Fasciculus Right

Figure 4.11: ROI Masks 19 through 24

4.3　Data Analysis

The data analysis was broken down into four major components:

- Case-based analysis using voxel-wise z-scoring analysis

- Longitudinal analysis observing the changes in a single subject over their recovery time

- Group-based analysis using Welch's t-test comparing the mTBI population to the control population

- Correlation analysis between DTI and QSM measurements for each subject

This approach will aid in determining which imaging metrics (FA, RD, AD, Susceptibility), used to characterize the brain microstructure, are most sensitive in the detection of mTBI. Further, the aim of the longitudinal and group analyses will see if any ROI metric measures have the potential to predict recovery times as well as symptom severity. Please note that the equations for statistical analysis derived in this section of the thesis were obtained from the text Applied Statistics and Probability for Engineers by Montgomery and Runger (Montgomery and Runger, 2007).

4.3.1　Normality Testing

After processing all of the images for each ROI, the next step was to ensure that the control data followed a Gaussian distribution. The statistical analysis methods such as z-score and t-score are dependent on the assumption that the sample population follows a normal distribution (as shown in Figure 4.12) otherwise any results obtained would not have any significance.
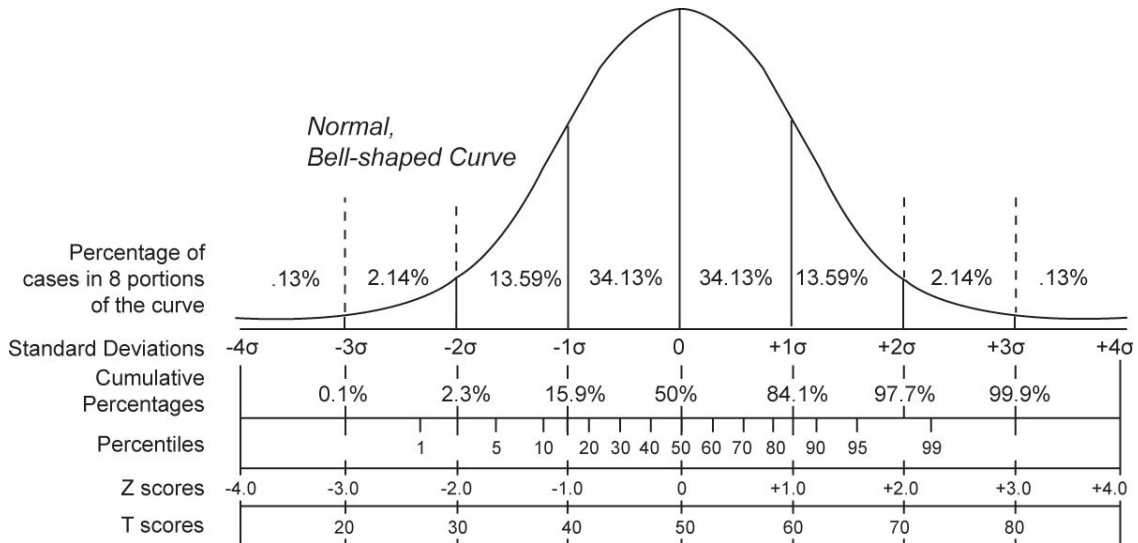
Figure 4.12: Gaussian Distribution and the standard grading methods including z-scoring and t-scoring [Online source: Area Education Agency 267 (2012). Permission to use this image included in Appendix E]

The Shapiro-Wilk normality test was used to test the null hypothesis that the data came from a normally distributed population (Shapiro and Wilk, 1965). Equation 4.1 shows the formula for Shapiro Wilk Test statistic, W:

$$W = \frac{(\sum_{i=1}^{n}(a_i x_{(i)}))^2}{\sum_{i=1}^{n}(x_i - \overline{x})^2} \tag{4.1}$$

where $x_{(i)}$ is the ith order statistic (meaning the ith smallest data value in the sample), $\overline{x}$ is the sample mean and a_i are constants derived by Shapiro and Wilk. These constants vary depending on the sample size. If W is below a certain threshold, determined by the significance level α, then the null hypothesis is rejected and it cannot be assumed that the data is normally distributed. The significance level represents the probability of incorrectly rejecting the null hypothesis H_0. For the purposes of this study, $\alpha = 0.01$, meaning that there exists a 1% risk of falsely

rejecting the hypothesis that the data follows a Gaussian distribution. W can be converted to a specific p-value, or calculated probability of finding the observed result when the null hypothesis is true. When testing for the normality of each control ROI, if the calculated p-value is less than the significance level of 0.01 then the null hypothesis was rejected. Otherwise, the null hypothesis cannot be rejected and the sample data will have passed the normality test. To simplify, if $W < 0.929$ then $p - value < \alpha = 0.01$, meaning that we reject H_0. The results of the Shapiro-Wilk normality test are summarized in Table 4.2. The vast majority of brain ROIs were accepted for each metric with a few exceptions. Every ROI passed the test for FA. In terms of RD, only the acoustic radiation (right) and corpus callosum regions were rejected and, looking at AD, the cingulum, corpus callosum, and uncinate fasciculus regions were also rejected.

Table 4.2: Shapiro-Wilk Normality Test for the control population showing the W-statistic values calculated for every ROI and DTI metric

ROI	W-Statistic		
	FA	AD	RD
Acoustic Radiation Left	0.9675	0.9439	0.9634
Acoustic Radiation Right	0.9308[+]	0.9655	0.8755[+++]
Cingulate Gyrus Left	0.9684	0.9732	0.9293[+]
Cingulate Gyrus Right	0.9312[+]	0.9295[+]	0.9676
Cingulum Left	0.9545	0.8603[+++]	0.9576
Cingulum Right	0.9445	0.8391[+++]	0.9544
Corpus Callosum	0.9545	0.7990[+++]	0.7244[+++]
Corticospinal Tract Left	0.9653	0.9687	0.9295[+]
Corticospinal Tract Right	0.9373	0.9437	0.9411
Forceps Major	0.9551	0.9787	0.9301[+]
Forceps Minor	0.9680	0.9400	0.9719
Fornix	0.9291[+]	0.9327	.9303[+]
Hippocampus Left	0.9300[+]	0.9538	0.9746
Hippocampus Right	0.9529	0.9672	0.9555
Inferior Fronto-occipital Fasciculus Left	0.9846	0.9299[+]	0.9741
Inferior Fronto-occipital Fasciculus Right	0.9679	0.9500	0.9291[+]
Inferior Longitudinal Fasciculus Left	0.9291	0.9345	0.9293
Inferior Longitudinal Fasciculus Right	0.9788	0.9615	.9311[+]
Optic Radiation Left	0.9451	0.9635	0.9593
Optic Radiation Right	0.9385	0.9506	0.9397
Superior Longitudinal Fasciculus Left	0.9662	0.9348	0.9634
Superior Longitudinal Fasciculus Right	0.9758	0.9564	0.9756
Uncinate Fasciculus Left	0.9462	0.8777[+++]	0.9732
Uncinate Fasciculus Right	0.9589	0.8865[+++]	0.9326[+]

[+] denotes $\alpha > 0.01$ after 2 or fewer outliers were removed from the data set; the sample is normally distributed

[+++] denotes $\alpha < 0.01$ therefore H_0 was rejected and the sample is not normally distributed

4.3.2   Case-Based

Voxel-wise z-scoring

The first portion of this study involved voxel-wise z-score analysis of the individual mTBI patients (n=26) for the three DTI metrics previously mentioned: FA, AD and RD. The DTI metric volumes for each patient were multiplied by a brain mask for all 24 processed ROIs to obtain the FA, AD, and RD values within each voxel of the specified ROIs. The mean value was then obtained for each ROI and used for Z-scoring by inputting it into equation 4.2

$$Z = \frac{x - \mu}{\sigma} \tag{4.2}$$

where x represents the mean DTI metric value for a particular ROI, μ represents the mean of the control group (for that same DTI metric and ROI), and σ is the standard deviation of the control group. Overall three DTI metrics were processed in 24 ROIs in each patient for z-scoring analysis. This equates to 72 unique z-scores for each individual patient and 1872 z-scores in total.

A z-score represents where the individual data point would fall on a normal-distribution curve (Figure 4.12) in terms of standard deviations relative to the control mean. The purpose of this portion of the study was to identify outliers from the dataset to determine which regions were most commonly affected by the mTBI (in terms of microstructure). An outlier can be defined as an observation which significantly differs from the normal data. In this study we have defined an outlier as a data point which falls $\pm 2\sigma$ from the mean. We have also identified the number of outliers which fall $\pm 3\sigma$ from the mean to further observe if there were any extreme

shifts from the norm within a particular brain region. If an observation is $\pm 2\sigma$ from the mean it falls in the 95th percentile of the normal data. For $\pm 3\sigma$ the observation falls in the 99th percentile of the data (99.74% to be exact).

Longitudinal Analysis

In terms of longitudinal analysis we investigated changes within each subject's brain microstructure over their recovery time. Seven of the 26 mTBI patients returned for an additional follow up scan and two of those seven returned for a third and final exam. These nine additional follow up DTI scans were processed identically to the initial scans and their z-scores were also calculated for FA, AD, and RD within each ROI. For each subject, outliers from the initial scans were compared relative to their follow up scans (which were scheduled post symptom resolution) to see what changes could be observed, if any, in terms of the microstructure in these regions. The relative change was calculated as follows

$$RelativeChange = \frac{Scan_f - Scan_i}{Scan_i} \tag{4.3}$$

where $Scan_f$ is the DTI-metric value for the follow up scan and $Scan_i$ is the DTI metric for the initial scan. Additionally, the z-score was also taken into account to monitor any changes and determine where the observation for the follow up scans fell relative to the $\pm 2\sigma$ boundary.

4.3.3   Group-Based

For this portion of the study, group statistics were calculated for the mTBI group as a whole (including initial and follow up scnas; n=35) and compared to the control group

(n=49) to investigate population differences. Further, the mTBI patients were also split into distinct sub-groups to further investigate the effects of mTBI and determine if any other relevant factors existed. The sub-groups included:

- Time to reach symptom resolution; split into stratum 1/2 (n=11) and stratum 3 (n=24) subgroups

- Injury Status; split into symptomatic (n=26) and symptom-free (n=9) subgroups

- Age; split into age 10-13 (n=12) and 14-17 (n=23) subgroups

- Gender; split into male (n=13) and female (n=22) subgroups

A two-tailed Welch's t-test was used in order to test the hypothesis that two datasets come from the same population. This was calculated for each of the subgroups relative to one another and the control groups as well. The assumptions of the Welch's t-test are that the two samples come from normal populations and are independent of each other. Additionally, the Welch's t-test does not assume that the variances of each sample are equivalent. The statistic t is defined as

$$t = \frac{\overline{X_1} - \overline{X_2}}{\sqrt{\frac{s_1^2}{n_1} + \frac{s_2^2}{n_2}}} \tag{4.4}$$

where $\overline{X_1}$, s_1^2 and n_1 represent the sample mean, sample variance and sample size for the first group and $\overline{X_2}$, s_2^2 and n_2 represent the sample mean, sample variance and sample size for the second group.

Next the degrees of freedom ν must be calculated using the following approxima-

tion:

$$\nu \approx \frac{(\frac{s_1^2}{N_1} + \frac{s_2^2}{N_2})^2}{\frac{s_1^4}{N_1^2(N_1-1)} + \frac{s_2^4}{N_2^2(N_2-1)}} \tag{4.5}$$

Using the calculated t and ν values allows us to compute the p-value using Statistical

Tables for the Percentage points $t_{\alpha,\nu}$ of the t-Distribution (Montgomery and Runger,

2007). If $p < 0.05$ the null hypothesis is rejected and we can assume, with 95%

confidence, that the two samples are significantly different and do not come from the

same population.

4.3.4   Correlating DTI to QSM

Susceptibility, as measured by QSM, was compared to each DTI metric to determine

if there was any correlation within a particular ROI. This was accomplished by cal-

culating the Pearson product moment correlation coefficient r as a measure of the

linear correlation between two variables. The coefficient r is defined as

$$r = \frac{\sum x_i y_i - n\overline{xy}}{(n-1)s_x s_y} \tag{4.6}$$

where n is the number of observations, $\overline{x}$ is the mean of all x_i, $\overline{y}$ is the mean of all

y_i, s_x is the standard deviation for variable x and s_y is the standard deviation for

variable y. By design r is constrained as follows; $-1 \leq r \leq 1$. Referring to Figure

4.13 , -1 denotes a total negative linear relationship, 0 means no correlation and 1 is

a total positive correlation. As a general rule of thumb, we can describe the strength

of the correlation measurement for absolute values of r:

- 0.00-0.19 as "very weak"

- 0.20-0.39 as "weak"

- 0.40-0.59 as "moderate"

- 0.60-0.79 as "strong"

- 0.80-1.00 as "very strong"

$$r = -1$$
perfect -ve correlation

$$r = 0$$
no correlation

$$r = 1$$
perfect +ve correlation
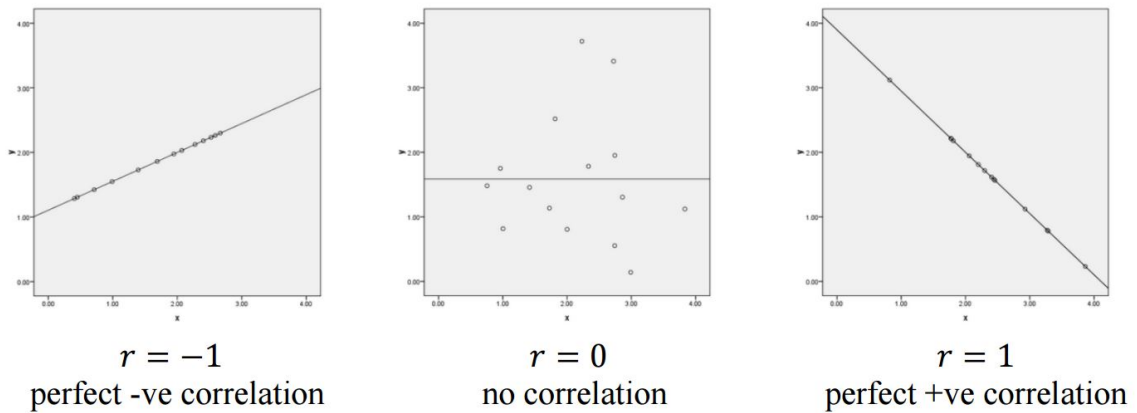
Figure 4.13: Graphical examples of the Pearson Product Moment Correlation Coefficient r

In addition, the correlation measurement r was also tested for significance to determine the appropriateness of defining the relationship as linear. In order to do so, the t-value was calculated using the formula

$$t = \frac{r\sqrt{n-2}}{\sqrt{1-r^2}} \tag{4.7}$$

Using this t value along with the degrees of freedom ($\nu = n - 2$) allows us to compute the p-value using Statistical Tables for the Percentage points $t_{\alpha,\nu}$ of the t-Distribution (Montgomery and Runger, 2007). It should be noted that a two-tailed t-test was used. Therefore, if $p < 0.05$ and $r < 0$ we can assume, with 95% confidence, that a

significant negative correlation exists between susceptibility and the given DTI metric (within a particular region). Similarly, if $p < 0.05$ and $r > 0$ a significant positive correlation exists. The result would not be considered significant for any other cases.

Chapter 5

Results and Evaluation

5.1 Case-based Analysis

5.1.1 Voxel-wise z-scoring

The first case-based analysis looked at voxel-wise z-scores of the mTBI patients (n=26) relative to the normal control population for each of the 24 brain regions. As previously mentioned, z-scores were calculated for FA, AD, and RD values. This method allowed for localization and quantitation of abnormal regions on a per-patient basis.

Table 5.1 shows the number of outliers for each brain region in terms of FA relative to the healthy control population. A number of outliers were observed in a variety of regions throughout the brain. It should be noted that the distribution of the observed outliers was fairly evenly distributed between the left and right hemispheres (58 and 45 outliers, respectively). Statistically significant abnormalities were most frequently observed in the left inferior fronto-occipital fasciculus (12 outliers), left

inferior longitudinal fasciculus (12 outliers), and in both the left and right superior longitudinal fasciculus (11 and 17 outliers, respectively). Further, fewer abnormalities were present in the inner-most brain regions; the cingulum, cingulate gyrus, corpus callosum, fornix and hippocampus regions all had three or fewer outliers. Past studies from Morey (2013) as well as Laitinen *et al.* (2015) have shown a correlation with mTBI severity and WM integrity in the corpus callosum and longitudinal fasciculus. The results in this thesis agree with a loss of integrity in the longitudinal fasciculus, however, they appear to be in complete contrast in terms of corpus callosum integrity as absolutely no outliers were observed. Perhaps the most interesting observation is that in the four regions with the greatest occurrence of abnormalities, every single outlier was found to have $z < -2$, meaning that the FA value was at least two standard deviations less than the mean of the control group. This suggests that the WM integrity was compromised in these regions as a result of mTBI.

Table 5.1: Fractional Anistropy Outliers: Identifying which brain regions are outliers based on Z-scoring of each region's Fractional Anistropy value relative to a healthy control population

ROI	Control Mean	Control SD	No. Outliers (± 2σ)	No. Outliers (± 3σ)
Acoustic Radiation Left	0.2844	0.0257	5	0
Acoustic Radiation Right	0.2724	0.0257	4	0
Cingulate Gyrus Left	0.3609	0.0379	2	0
Cingulate Gyrus Right	0.3095	0.0485	1	0
Cingulum Left	0.3455	0.0407	3	0
Cingulum Right	0.3580	0.0513	0	0
Corpus Callosum	0.4076	0.0319	0	0
Corticospinal Tract Left	0.4713	0.0229	3	2
Corticospinal Tract Right	0.4652	0.0219	5	1
Forceps Major	0.3871	0.0512	0	0
Forceps Minor	0.3770	0.0265	3	1
Fornix	0.2999	0.0415	2	0
Hippocampus Left	0.2652	0.0405	2	0
Hippocampus Right	0.2764	0.0399	1	0
Inferior Fronto-occipital Fasciculus Left	0.3978	0.0207	12	2
Inferior Fronto-occipital Fasciculus Right	0.3945	0.0255	5	0
Inferior Longitudinal Fasciculus Left	0.3517	0.0230	12	1
Inferior Longitudinal Fasciculus Right	0.3600	0.0282	6	1
Optic Radiation Left	0.2975	0.0157	1	0
Optic Radiation Right	0.3092	0.0192	2	0
Superior Longitudinal Fasciculus Left	0.3337	0.0178	11	4
Superior Longitudinal Fasciculus Right	0.3482	0.0185	17	8
Uncinate Fasciculus Left	0.3786	0.0322	7	1
Uncinate Fasciculus Right	0.3534	0.0401	4	0

The next DTI metric studied was AD. Table 5.2 shows the number of outliers for each brain region in terms of AD relative to the healthy control group. This metric had the fewest number of outliers (32) compared to FA and RD z-scores. Of these outliers, 21 were located in the right brain hemisphere compared to only five in the left. Five of the 24 ROIs failed the Shapiro-Wilk normality test as shown in Table 4.2. The right corticospinal tract was the only region that had a significant number of abnormalities (in 10 of the 26 subjects). All ten outliers had $z > 2$ and 25 of the 26 subjects had $z > 0$ indicating that the AD values were greater in mTBI patients relative to the control population. On the other end of the spectrum, nine

of the 19 (normal) regions did not produce a single outlier - this includes the inferior fronto-occipital fasciculus, inferior longitudinal fasciculus and superior longitudinal fasciculus. This is an interesting finding since these were the regions with the highest occurrence of abnormalities when looking at FA.

Table 5.2: Axial Diffusivity Outliers: Identifying which brain regions are outliers based on Z-scoring of each region's principal eigenvalue relative to a healthy control population. Some regions were left blank because they did not pass the Normality Test and z-scoring could not be performed.

ROI	Control Mean	Control SD	No. Outliers (± 2σ)	No. Outliers (± 3σ)
Acoustic Radiation Left	1.159E-03	4.145E-05	1	0
Acoustic Radiation Right	1.171E-03	3.600E-05	6	1
Cingulate Gyrus Left	1.124E-03	6.492E-05	0	0
Cingulate Gyrus Right	1.072E-03	6.246E-05	0	0
Cingulum Left	---	---	---	---
Cingulum Right	---	---	---	---
Corpus Callosum	---	---	---	---
Corticospinal Tract Left	1.323E-03	6.143E-05	3	0
Corticospinal Tract Right	1.315E-03	6.112E-05	10	1
Forceps Major	1.338E-03	9.488E-05	3	0
Forceps Minor	1.219E-03	4.729E-05	1	0
Fornix	1.679E-03	1.663E-04	2	0
Hippocampus Left	1.120E-03	5.306E-05	0	0
Hippocampus Right	1.131E-03	4.884E-05	4	0
Inferior Fronto-occipital Fasciculus Left	1.204E-03	6.051E-05	0	0
Inferior Fronto-occipital Fasciculus Right	1.209E-03	5.535E-05	0	0
Inferior Longitudinal Fasciculus Left	1.167E-03	6.539E-05	0	0
Inferior Longitudinal Fasciculus Right	1.150E-03	5.786E-05	0	0
Optic Radiation Left	1.148E-03	4.877E-05	1	0
Optic Radiation Right	1.136E-03	4.268E-05	1	0
Superior Longitudinal Fasciculus Left	1.097E-03	4.412E-05	0	0
Superior Longitudinal Fasciculus Right	1.097E-03	4.122E-05	0	0
Uncinate Fasciculus Left	---	---	---	---
Uncinate Fasciculus Right	---	---	---	---

Lastly, the regions were evaluated in terms of RD. Table 5.3 shows the number of outliers for each brain region in terms of RD relative to the healthy control group. This metric produced a total of 55 outliers, with a fairly even distribution between the left and right brain hemispheres (28 and 21 outliers, respectively). Two of the 24 ROIs failed the Shapiro-Wilk normality test (Table 4.2) and could not be processed

for z-scoring. The right corticospinal tract and left uncinate fasciculus both had a significant number of abnormalities (10 of 26 subjects in each ROI). In both of these regions, every outlier had $z > 2$. In the corticospinal tract, $z > 0$ for 22 of the 26 subjects and in the uncinate fasciculus, $z > 0$ for 25 of the 26 subjects. This indicates that there was an observed increase of RD in the majority of mTBI patients relative to the healthy control population. Additionally, eight of the 22 (normal) regions did not produce a single outlier, including the inferior fronto-occipital fasciculus, and inferior longitudinal fasciculus - both regions which had a large number of outliers when measuring FA.

Table 5.3: Radial Diffusivity Outliers: Identifying which brain regions are outliers based on Z-scoring of each region's RD value relative to a healthy control population. Some regions were left blank because they did not pass the Normality Test and z-scoring could not be performed.

ROI	Control Mean	Control SD	No. Outliers (± 2σ)	No. Outliers (± 3σ)
Acoustic Radiation Left	7.684E-04	4.978E-05	4	0
Acoustic Radiation Right	---	---	---	---
Cingulate Gyrus Left	6.469E-04	3.709E-05	5	0
Cingulate Gyrus Right	6.763E-04	4.080E-05	5	0
Cingulum Left	6.743E-04	4.312E-05	0	0
Cingulum Right	6.589E-04	4.593E-05	0	0
Corpus Callosum	---	---	---	---
Corticospinal Tract Left	6.523E-04	6.324E-05	6	0
Corticospinal Tract Right	6.517E-04	5.401E-05	10	2
Forceps Major	7.288E-04	7.914E-05	1	0
Forceps Minor	6.903E-04	3.596E-05	4	1
Fornix	1.093E-03	1.853E-04	1	0
Hippocampus Left	7.602E-04	6.240E-05	0	0
Hippocampus Right	7.596E-04	6.219E-05	1	0
Inferior Fronto-occipital Fasciculus Left	6.526E-04	3.273E-05	0	0
Inferior Fronto-occipital Fasciculus Right	6.555E-04	4.559E-05	0	0
Inferior Longitudinal Fasciculus Left	6.884E-04	3.580E-05	0	0
Inferior Longitudinal Fasciculus Right	6.722E-04	4.262E-05	0	0
Optic Radiation Left	7.276E-04	3.287E-05	2	0
Optic Radiation Right	7.088E-04	3.335E-05	0	0
Superior Longitudinal Fasciculus Left	6.779E-04	2.853E-05	1	0
Superior Longitudinal Fasciculus Right	6.624E-04	3.124E-05	1	0
Uncinate Fasciculus Left	6.782E-04	3.829E-05	10	3
Uncinate Fasciculus Right	7.146E-04	5.550E-05	4	0

Overall, significant abnormalities were frequently observed in a number of regions including the longitudinal fasciculus, fronto-occipital fasciculus, uncinate fasciculus and corticospinal tract, while unique abnormalities were localized in a host of other areas due to the individuality of each childs injury. It is also interesting to note that in terms of FA and RD the location of the outliers were fairly evenly distributed between the left and right brain hemispheres with slightly more observed in the left hemisphere (approximately 57%). However, when considering AD z-scores, the vast majority of abnormalities were located in the right brain hemisphere (approximately 81%). This may be due to the mode of injury (ie. location of impact at time of injury). However, it also may be a result of the relatively smaller sample size as this metric produced the fewest number of outliers compared to the other two DTI metrics (FA and RD). In terms of quantity, 108 outliers were observed with FA, 55 with RD and 32 with AD. Perhaps an increased sample size would mitigate this perceived right-hemisphere bias.

5.1.2   Longitudinal Analysis

Next, we took a more in depth analysis of the seven subjects who returned for atleast one follow up scan and monitored their recovery over time comparing their initial, symptomatic, results relative to their follow up, symptom-free, scans. Table 5.4 summarizes the relative change in FA between initial and follow up scan(s). Theoretically we should expect to see the FA increase over time which would indicate an improvement in WM integrity. Surprisingly, minimal change was observed in the vast majority of cases. Among the seven subjects, 24 abnormal regions were identified in total. Nine of the abnormal regions saw a shift in FA to within the normal range ($\pm 2\sigma$) in their

follow up scan. Also, interesting to note, the FA value increased in 16 of the 24 regions between the first and second scan. Participant 5 saw a very significant increase in FA in the uncinate fasciculus region (20.08%) which brought it back within $\pm 2\sigma$ of the control mean. This participant also saw a 7.04% decrease in the superior longitudinal fasciculus which is quite odd. Additionally, participant 6 was the only subject who had an increase in FA in all four abnormal regions which brought the FA value within $\pm 2\sigma$ of the control mean. It would appear that FA monitoring over time has variable effectiveness depending on the patient and the uniqueness of their injury.

Table 5.4: FA Longitudinal Analysis

Participant	Gender	Age	Recovery Stratum	Initial PCSS score (/132)	ROI	FA Measurement			% Change	
						Scan 1	Scan 2	Scan 3	Scan 1 to 2	Scan 1 to 3
1	M	13	2	5	Inferior Fronto-occipital Fasciculus (left)	0.35302	0.34525	---	-2.20%	---
					Superior Longitudinal Fasciculus (right)	0.30340	0.30708	---	1.21%	---
					Uncinate Fasciculus (left)	0.29718	0.29758	---	0.14%	---
2	F	15	3	30	---	---	---	---	---	---
3	M	10	2	13	Acoustic Radiation (left)	0.22583	0.21748	---	-3.70%	---
					Cingulum (left)	0.26172	0.26284	---	0.43%	---
					Forceps Minor	0.31363	0.29651	---	-5.46%	---
					Hippocampus (right)	0.19261	0.19873 †	---	3.18%	---
					Inferior Fronto-occipital Fasciculus (left)	0.34020	0.34367 †	---	1.02%	---
					Inferior Fronto-occipital Fasciculus (right)	0.33257	0.33574	---	0.95%	---
					Inferior Longitudinal Fasciculus (left)	0.30391	0.31223 †	---	2.74%	---
					Superior Longitudinal Fasciculus (left)	0.27860	0.28522	---	2.38%	---
					Superior Longitudinal Fasciculus (right)	0.28069	0.27513	---	-1.98%	---
					Uncinate Fasciculus (left)	0.29001	0.28001	---	-3.45%	---
4	F	17	3	10	Corticospinal Tract (right)	0.39576	0.40298	0.39182	1.82%	-1.00%
					Superior Longitudinal Fasciculus (right)	0.30639	0.30823	0.29712	0.60%	-3.03%
5	F	16	3	2	Superior Longitudinal Fasciculus (right)	0.31095	0.28905	---	-7.04%	---
					Uncinate Fasciculus (right)	0.25701	0.30863 †	---	20.08%	---
6	F	14	3	57	Inferior Fronto-occipital Fasciculus (left)	0.35563	0.35997 †	---	1.22%	---
					Inferior Longitudinal Fasciculus (left)	0.30384	0.31051 †	---	2.20%	---
					Uncinate Fasciculus (left)	0.30572	0.31451 †	---	2.88%	---
					Uncinate Fasciculus (right)	0.27150	0.27436 †	---	1.05%	---
7	M	16	3	2	Acoustic Radiation (left)	0.22887	0.22845	---	-0.18%	---
					Inferior Fronto-occipital Fasciculus (left)	0.35628	0.35702 †	---	0.21%	---
					Inferior Longitudinal Fasciculus (left)	0.29365	0.28909	---	-1.55%	---

† denotes the measurement is not an outlier (ie. It is within ± 2σ of the control mean)

Table 5.5 summarizes the relative change in AD between initial and follow up scan(s). Five of the seven abnormal regions, identified in the seven subjects, shifted to within the expected healthy range. It was difficult to determine a general trend in the data as three of the seven regions saw relatively small increases in AD and the other four showed decreases in AD to varying degrees. Patient 5 and 6 saw the most significant decreases in the right corticospinal tract and right acoustic radiation regions (-7.89% and -6.40%, respectively). Other than those two instances, the other regions exhibited fairly modest change between scans. These results suggest that AD may be a more effective way of monitoring recovery over time however it has some drawbacks. First, AD appears to be the least effective of the three DTI metrics at identifying abnormalities (as shown in the previous section it had the fewest number of outliers compared to FA and RD). Second, with such a small sample size, it was difficult to determine the general trend in the data. It appeared that AD may be slightly more likely to decrease post-recovery but almost half of the observations saw AD marginally increase. Further data is needed to confirm that AD is sensitive to measure microstructural changes indicating recovery from mTBI.

Lastly, Table 5.6 summarizes the relative change in RD between the initial and follow up scan(s). Seven of the 15 abnormal regions shifted back to within the expected control range in the second scan. The RD decreased in 13 of these abnormal regions between the first and second scan. Participant 4 oddly saw two of the regions fluctuate between normal and abnormal between the second and third scan. The RD measures of the uncinate fasciculus fluctuated within 1.90% of the initial scan which is fairly small and therefore we can assume that the microstructure remained mostly unchanged over time. However, the corticospinal tract is another matter. It

experienced a relative change of up to 7.03% from the initial scan meaning that this shift could indicate viable changes in microstructure over a short time span. But, it could also just be some sort of signal noise or perhaps a random anomaly in the acquisition. Participant 3 saw a significant RD decrease of -10.99% in the the right corticospinal tract. Most notably, all three abnormal regions identified in participant 5 experienced a fairly consistent decrease in RD. The RD decreased in the acoustic radiation as well as the left and right uncinate fasciculus by -12.58%, -12.85% and -10.74%, respectively. This analysis suggests that RD may be helpful in monitoring recovery from mTBI. Having said that, as was the case with both FA and AD, the efficacy of monitoring RD as a biomarker of patient recovery varies depending on the individual.

Table 5.5: AD Longitudinal Analysis

Participant	Gender	Age	Recovery Stratum	Initial PCSS score (/132)	ROI	AD Measurement			% Change	
						Scan 1	Scan 2	Scan 3	Scan 1 to 2	Scan 1 to 3
1	M	13	2	5	Hippocampus (right)	1.250E-03	1.226E-03 †	---	-1.92%	---
					Optic Radiation (right)	1.050E-03	1.060E-03 †	---	0.95%	---
2	F	15	3	30	---	---	---	---	---	---
3	M	10	2	13	Corticospinal Tract (left)	1.470E-03	1.480E-03	---	0.68%	---
					Corticospinal Tract (right)	1.520E-03	1.400E-03 †	---	-7.89%	---
4	F	17	3	10	Corticospinal Tract (right)	1.456E-03	1.462E-03	1.450E-03	0.41%	-0.41%
5	F	16	3	2	Acoustic Radiation (right)	1.250E-03	1.170E-03 †	---	-6.40%	---
6	F	14	3	57	---	---	---	---	---	---
7	M	16	3	2	Fornix	2.020E-03	2.006E-03 †	---	-0.69%	---

† denotes the measurement is not an outlier (ie. It is within ± 2σ of the control mean)

Table 5.6: RD Longitudinal Analysis

Participant	Gender	Age	Recovery Stratum	Initial PCSS score (/132)	ROI	RD Measurement			% Change	
						Scan 1	Scan 2	Scan 3	Scan 1 to 2	Scan 1 to 3
1	M	13	2	5	Cingulate Gyrus (right)	7.70E-04	7.64E-04	---	-0.78%	---
					Hippocampus (right)	9.17E-04	9.00E-04	---	-1.85%	---
2	F	15	3	30	Optic Radiation (left)	6.61E-04	6.67E-04 †	6.62E-04 †	0.91%	0.15%
3	M	10	2	13	Corticospinal Tract (right)	8.10E-04	7.21E-04 †	---	-10.99%	---
4	F	17	3	10	Corticospinal Tract (left)	8.11E-04	7.54E-04 †	8.37E-04	-7.03%	3.21%
					Corticospinal Tract (right)	8.57E-04	8.16E-04	8.35E-04	-4.78%	-2.57%
					Uncinate Fasciculus (left)	7.59E-04	7.51E-04 †	7.60E-04	-1.05%	0.13%
					Uncinate Fasciculus (right)	8.42E-04	8.26E-04	8.28E-04	-1.90%	-1.66%
					Acoustic Radiation (right)	9.30E-04	8.13E-04 †	---	-12.58%	---
5	F	16	3	2	Uncinate Fasciculus (left)	7.78E-04	6.78E-04 †	---	-12.85%	---
					Uncinate Fasciculus (right)	8.29E-04	7.40E-04 †	---	-10.74%	---
6	F	14	3	57	Acoustic Radiation (left)	8.87E-04	8.81E-04	---	-0.68%	---
					Uncinate Fasciculus (left)	8.63E-04	8.39E-04	---	-2.78%	---
7	M	16	3	2	Acoustic Radiation (right)	9.19E-04	9.16E-04	---	-0.33%	---
					Cingulate Gyrus (right)	7.78E-04	7.87E-04	---	1.16%	---

† denotes the measurement is not an outlier (ie. It is within ± 2σ of the control mean)

5.2   Group-based Analysis

In this next section, focus will be shifted away from case-based analysis towards a group-based approach. This should provide a means to identify major trends and patterns in the data. As previously mentioned, theoretically we would expect to see decreased FA in the mTBI group relative to the control population. Further, it is reasonable to expect that either AD or RD (or a combination of both) would be greater in the mTBI group. These expected outcomes are believed to be indicative of compromised WM integrity and correlate to the degree of injury. As was the case for z-scoring, t-test analysis requires that the data follow a Gaussian distribution. For AD, five of the 24 regions failed the normality test and could not be analyzed. Two of the regions failed for RD as well.

5.2.1   mTBI Group versus Control Group

Referring to Table 5.7, in terms of FA, the mTBI group was significantly different from the control group in 19 of the 24 ROIs analyzed. The remaining five regions which did not generate a $p < 0.05$ were the left and right cingulum, corpus callosum, forceps major and fornix. It is interesting that these five regions are located in the deeper brain tissues whereas the other 19 regions, for which the null hypothesis was rejected, tended to be from more peripheral areas of the brain in closer proximity to the skull. Additionally, in every region, excluding the forceps major, the mean FA for the mTBI group was less than for the control group. This was in line with theory suggesting that a decrease in FA correlates to a loss of WM integrity. Another exciting result was that a number of regions had $p < 1.0E^{-9}$ which means that there was a one in a billion chance that we were wrong to reject the null hypothesis and

assume that the region was from a different population than the control group.

Table 5.7: Fractional Anisotropy T-Test scores: mTBI group vs control group

ROI	TBI Group	Control Group	P-Value (T-test)	Reject H$_0$ (if p<0.05)
Acoustic Radiation Left	0.2562	0.2844	1.56E-06	Reject
Acoustic Radiation Right	0.2504	0.2724	1.01E-04	Reject
Cingulate Gyrus Left	0.3378	0.3609	8.36E-03	Reject
Cingulate Gyrus Right	0.2775	0.3095	2.35E-03	Reject
Cingulum Left	0.3324	0.3455	1.71E-01	---
Cingulum Right	0.3402	0.3580	8.54E-02	---
Corpus Callosum	0.4020	0.4076	3.60E-01	---
Corticospinal Tract Left	0.4418	0.4713	1.66E-07	Reject
Corticospinal Tract Right	0.4406	0.4652	1.61E-05	Reject
Forceps Major	0.3937	0.3871	4.79E-01	---
Forceps Minor	0.3567	0.3770	6.17E-04	Reject
Fornix	0.2866	0.2999	1.21E-01	---
Hippocampus Left	0.2349	0.2652	3.59E-04	Reject
Hippocampus Right	0.2493	0.2764	5.93E-04	Reject
Inferior Fronto-occipital Fasciculus Left	0.3666	0.3978	7.17E-09	Reject
Inferior Fronto-occipital Fasciculus Right	0.3601	0.3945	1.70E-10	Reject
Inferior Longitudinal Fasciculus Left	0.3158	0.3517	3.43E-09	Reject
Inferior Longitudinal Fasciculus Right	0.3234	0.3600	8.50E-09	Reject
Optic Radiation Left	0.2907	0.2975	4.29E-02	Reject
Optic Radiation Right	0.2945	0.3092	1.18E-04	Reject
Superior Longitudinal Fasciculus Left	0.3012	0.3337	1.66E-12	Reject
Superior Longitudinal Fasciculus Right	0.3033	0.3482	6.31E-19	Reject
Uncinate Fasciculus Left	0.3245	0.3786	1.17E-12	Reject
Uncinate Fasciculus Right	0.2974	0.3534	3.89E-12	Reject
			TOTAL	19

Table 5.8 summarizes T-test results in terms of AD. Significant differences between the mTBI group and control group were found in nine of the 19 regions (that passed the normality test). The results appear to be relatively random as far as which ROIs had $p < 0.05$. In fact, in four instances, the one hemisphere of a particular region was accepted while another rejected. This was the case for the acoustic radiation, hippocampus, inferior fronto-occipital fasciculus and inferior longitudinal fasciculus. On the other end of the spectrum, both the corticospinal tract and optic radiation regions were the most significantly different between the mTBI and control data (with all their p-values calculated at $1.634E^{-7}$ or less). In 11 of the 19 regions, the mTBI

group had higher mean AD compared to the control group. A similar pattern was observed among the nine significantly different ROIs with greater mean AD values found in five of the regions.

Table 5.8: Axial Diffusivity T-Test scores: mTBI group versus control group

ROI	TBI Group	Control Group	P-Value (T-test)	Reject H_0 (if p<0.05)
Acoustic Radiation Left	1.159E-03	1.159E-03	9.638E-01	---
Acoustic Radiation Right	1.197E-03	1.171E-03	7.972E-03	Reject
Cingulate Gyrus Left	1.134E-03	1.124E-03	3.675E-01	---
Cingulate Gyrus Right	1.089E-03	1.072E-03	1.203E-01	---
Cingulum Left	---	---	---	---
Cingulum Right	---	---	---	---
Corpus Callosum	---	---	---	---
Corticospinal Tract Left	1.392E-03	1.323E-03	1.634E-07	Reject
Corticospinal Tract Right	1.404E-03	1.315E-03	2.664E-09	Reject
Forceps Major	1.344E-03	1.338E-03	7.825E-01	---
Forceps Minor	1.247E-03	1.219E-03	2.068E-03	Reject
Fornix	1.707E-03	1.679E-03	4.294E-01	---
Hippocampus Left	1.106E-03	1.120E-03	1.864E-01	---
Hippocampus Right	1.161E-03	1.131E-03	9.804E-03	Reject
Inferior Fronto-occipital Fasciculus Left	1.179E-03	1.204E-03	1.321E-02	Reject
Inferior Fronto-occipital Fasciculus Right	1.194E-03	1.209E-03	1.041E-01	---
Inferior Longitudinal Fasciculus Left	1.133E-03	1.167E-03	1.587E-03	Reject
Inferior Longitudinal Fasciculus Right	1.133E-03	1.150E-03	9.043E-02	---
Optic Radiation Left	1.096E-03	1.148E-03	2.715E-08	Reject
Optic Radiation Right	1.093E-03	1.136E-03	9.019E-08	Reject
Superior Longitudinal Fasciculus Left	1.088E-03	1.097E-03	1.913E-01	---
Superior Longitudinal Fasciculus Right	1.102E-03	1.097E-03	4.598E-01	---
Uncinate Fasciculus Left	---	---	---	---
Uncinate Fasciculus Right	---	---	---	---
			TOTAL	9

Table 5.9 provides a summary of the RD analysis T-test results. The mTBI group was significantly different from the control group in 14 of the 22 (normal) regions. The corticospinal tract and uninate fasciculus regions had the greatest probability of being from two different populations with p-values at $4.589E^{-7}$ or less. Again, much like with AD, the results appear to be fairly random with both peripheral and deeper brain regions having p-values below the $p = 0.05$ threshold. The mean RD of the mTBI group was greater than the control group in 15 of the 22 regions tested.

Similarly, this was also the case in 10 of the 14 significantly different regions.

Table 5.9: Radial Diffusivity T-Test scores: mTBI group versus control group

ROI	TBI Group	Control Group	P-Value (T-test)	Reject H$_0$ (if p<0.05)
Acoustic Radiation Left	8.181E-04	7.684E-04	6.903E-06	Reject
Acoustic Radiation Right	---	---	---	---
Cingulate Gyrus Left	6.833E-04	6.469E-04	4.014E-05	Reject
Cingulate Gyrus Right	7.123E-04	6.763E-04	3.666E-04	Reject
Cingulum Left	6.814E-04	6.743E-04	4.140E-01	---
Cingulum Right	6.685E-04	6.589E-04	3.253E-01	---
Corpus Callosum	---	---	---	---
Corticospinal Tract Left	7.329E-04	6.523E-04	1.277E-07	Reject
Corticospinal Tract Right	7.341E-04	6.517E-04	4.589E-07	Reject
Forceps Major	6.987E-04	7.288E-04	8.947E-02	---
Forceps Minor	7.227E-04	6.903E-04	7.028E-05	Reject
Fornix	1.145E-03	1.093E-03	1.877E-01	---
Hippocampus Left	7.549E-04	7.602E-04	6.610E-01	---
Hippocampus Right	7.928E-04	7.596E-04	1.227E-02	Reject
Inferior Fronto-occipital Fasciculus Left	6.505E-04	6.526E-04	7.333E-01	---
Inferior Fronto-occipital Fasciculus Right	6.621E-04	6.555E-04	3.735E-01	---
Inferior Longitudinal Fasciculus Left	6.707E-04	6.884E-04	9.671E-03	Reject
Inferior Longitudinal Fasciculus Right	6.572E-04	6.722E-04	2.844E-02	Reject
Optic Radiation Left	6.933E-04	7.276E-04	1.232E-07	Reject
Optic Radiation Right	6.857E-04	7.088E-04	1.621E-04	Reject
Superior Longitudinal Fasciculus Left	6.809E-04	6.779E-04	5.802E-01	---
Superior Longitudinal Fasciculus Right	6.861E-04	6.624E-04	1.094E-04	Reject
Uncinate Fasciculus Left	7.437E-04	6.782E-04	6.492E-09	Reject
Uncinate Fasciculus Right	7.823E-04	7.146E-04	9.313E-09	Reject
			TOTAL	14

In general, FA results for all but one region followed a similar trend in that the mTBI group mean was consistently less than the control group. Conversely, the RD and AD measurements were more variable with a slight tendency toward the mTBI averages being greater than the control population. In order to determine if any other trends existed within the RD and AD measurements further analysis was performed. This analysis focused specifically on ROIs which had $p < 0.05$ for both DTI metrics. Referring to Table 5.10, seven regions were found to be significantly different in terms of both AD and RD; the corticospinal tract, forceps minor, right hippocampus, left inferior longitudinal fasciculus and optic radiation. In every region,

without exception, both AD and RD measurements trended in the same direction (ie. either increased or decreased relative to the control group). The corticospinal tract saw the most dramatic difference between the two groups, with approximately 12.55% greater AD and 6.0% greater RD in both left and right hemispheres. Further, the forceps minor and right hippocampus were moderately greater for both RD and AD in mTBI patients by 2.3% to 4.7%. The inferior longitudinal fasciculus in addition to both optic radiation regions had moderately lower values in the mTBI group compared to the control group by factors of -2.6% to -4.7%.

Table 5.10: Relative Difference in AD and RD between the mTBI and control group. Table only includes ROIs for which $p < 0.05$ for both DTI metrics

ROI	% Difference (mTBI vs Control)	
	AD	RD
Corticospinal Tract Left	12.4%	5.2%
Corticospinal Tract Right	12.7%	6.8%
Forceps Minor	4.7%	2.3%
Hippocampus Right	4.4%	2.6%
Inferior Longitudinal Fasciculus Left	-2.6%	-3.0%
Optic Radiation Left	-4.7%	-4.5%
Optic Radiation Right	-3.3%	-3.7%

Looking at the big picture, the ROIs had variable efficacy at identifying differences between the control and mTBI groups in terms of FA, RD and AD measurements. Some regions were quite effective for all three DTI metrics, most were useful when focusing on one metric and a select few were completely ineffective regardless of the metric. We were unable to detect any group differences, regardless of the DTI metric, in the cingulum, corpus callosum, forceps major and fornix. Based on this evidence, these regions do not appear to provide any useful DTI information when determining group differences in mTBI. On the other hand the corticospinal tract, forceps minor,

right hippocampus, left inferior longitudinal fasciculus and optic radiation regions were all found to be significantly different in the mTBI group for the three metrics. Table 5.11 provides a rank-order of these seven ROIs based on each region's average p-value calculated for FA, AD and RD (where $p_{avg} = \frac{p_{FA}+p_{AD}+p_{RD}}{3}$). This data suggests that the corticospinal tract was the most effective region to focus on when differentiating between the mTBI and healthy control groups.

Table 5.11: Ranking the most effective ROIs at identifying significant differences between mTBI and control groups. Based on the average p-value of each ROI for the three DTI metrics.

ROI	Average P-value (FA + AD + RD)
Corticospinal Tract Left	1.53E-07
Corticospinal Tract Right	5.52E-06
Optic Radiation Right	9.35E-05
Forceps Minor	9.19E-04
Inferior Longitudinal Fasciculus Left	3.75E-03
Hippocampus Right	7.55E-03
Optic Radiation Left	1.43E-02

5.2.2 Time to Reach Symptom Resolution

Independent samples Welch's t-tests were conducted for FA, RD and AD measurements between mTBI patients with recovery times of 28 days or less (stratum 1+2; n=11) versus mTBI patients with recovery times greater than 28 days (stratum 3; n=24). Refer to section 4.1.1 for further explanation on the recovery strata. Additional t-tests were also performed to compare each stratum subgroup to the control population. The results for FA, AD and RD are summarized in Tables 5.12, 5.13 and 5.14, respectively.

In terms of FA, there were significant differences found between stratum 1+2 and

stratum 3 in ten of the 24 regions analysed. However, in seven of the ten both strata were still significantly different relative to the control group. Interestingly, for the remaining three cases (right cingulate gyrus, right cingulum and left optic radiation) stratum 1+2 rejected the null hypothesis and stratum 3 was found to be more similar to the control group. This seems to be a counter intuitive result since stratum 3 indicates a longer recovery time. One caveat to this finding is that all three of the regions in question were found to be poor indicators of mTBI based on z-scoring (Table 5.1).

Further, the mean FA for the stratum 1+2 subgroup was less than for stratum 3 in 18 of the 24 regions. This is another fascinating, somewhat counter intuitive, outcome as a decrease in FA could be an indication of compromised WM integrity resulting from mTBI. Based on this reasoning, one would expect that lower FA would correlate to a more severe injury that would most likely result in longer recovery time. But in light of this data, perhaps that is not the case and more complex mechanisms are at work. However, both hemispheres of the corticospinal tract provided a more expected result with larger FA measures observed in the stratum 1+2 group relative to stratum 3. This bodes well for the efficacy of assessing the corticospinal tract region when diagnosing mTBI.

Looking at AD, only three regions showed differences between the stratum 1+2 and stratum 3 subgroups - the left and right inferior longitudinal fasciculus as well as the right optic radiation regions. However, none of these regions were particularly effective at identifying outliers using z-score analysis (Table 5.2). Focusing on the corticospinal tract, which had significantly greater AD in the mTBI group as a whole (Table 5.10), mixed results were observed here. Though AD for the right hemisphere

for the stratum 3 group was greater than for stratum 1+2, the left hemisphere had smaller AD measurements for stratum 3. Overall, both strata had eight regions which were found to be significantly different from the control population. This data implies that AD may not be a reliable metric for differentiating between the various recovery strata.

T-test results for RD identified significant differences between the two strata in only two of the 22 (normal) regions. The disparity observed in the left inferior fronto-occipital fasciculus is odd since both strata were found to be similar to the control group. This may just be a statistical anomaly as this ROI was not very effective at identifying mTBI based on z-scoring (Table 5.3). The corticospinal tract, however, showed more promising results. For both the left and right hemispheres, the RD measurement was greater in the stratum 3 subgroup relative to the stratum 1+2 subgroup. As a result, the p-values for the stratum 3 group compared to the control group are substantially less than for stratum 1+2 versus control. This follows the same trend shown in Table 5.10 which implies that increased RD in the corticospinal tract may be indicative of mTBI. Further, because the p-values were less when testing stratum 3 relative to the control group, the data also suggests that the corticospinal tract RD measure may also be useful to estimate a patient's expected recovery time.

Table 5.12: FA T-Test scores: comparing stratum 1+2 group, stratum 3 group and control group

ROI	Stratum 1+2	Stratum 3	Control Group	Stratum 1+2 vs Stratum 3		Stratum 1+2 vs Control		Stratum 3 vs Control	
				T-Test (P-value)	Reject H_0 (if p<0.05)	T-Test (P-value)	Reject H0 (if p<0.05)	T-Test (P-value)	Reject H0 (if p<0.05)
Acoustic Radiation Left	0.2509	0.2586	0.2844	4.40E-01	---	3.47E-03	Reject	2.59E-05	Reject
Acoustic Radiation Right	0.2535	0.2490	0.2724	6.58E-01	---	7.84E-02	---	6.19E-05	Reject
Cingulate Gyrus Left	0.3186	0.3466	0.3609	1.00E-01	---	1.77E-02	Reject	9.18E-02	---
Cingulate Gyrus Right	0.2541	0.2883	0.3095	4.03E-02	Reject	1.73E-03	Reject	5.50E-02	---
Cingulum Left	0.3071	0.3440	0.3455	5.40E-02	---	4.19E-02	Reject	8.66E-01	---
Cingulum Right	0.3137	0.3523	0.3580	3.89E-02	Reject	2.12E-02	Reject	5.59E-01	---
Corpus Callosum	0.3908	0.4072	0.4076	9.41E-02	---	9.19E-02	---	9.47E-01	---
Corticospinal Tract Left	0.4428	0.4413	0.4713	8.61E-01	---	1.23E-03	Reject	8.58E-06	Reject
Corticospinal Tract Right	0.4487	0.4369	0.4652	1.78E-01	---	3.93E-02	Reject	4.82E-05	Reject
Forceps Major	0.3772	0.4013	0.3871	1.14E-01	---	5.21E-01	---	1.24E-01	---
Forceps Minor	0.3422	0.3634	0.3770	2.80E-02	Reject	8.82E-04	Reject	2.56E-02	Reject
Fornix	0.2977	0.2815	0.2999	2.57E-01	---	8.73E-01	---	4.76E-02	Reject
Hippocampus Left	0.2389	0.2330	0.2652	6.79E-01	---	7.57E-02	---	3.71E-04	Reject
Hippocampus Right	0.2398	0.2536	0.2764	2.96E-01	---	1.35E-02	Reject	3.39E-03	Reject
Inferior Fronto-occipital Fasciculus Left	0.3516	0.3735	0.3978	2.19E-03	Reject	1.34E-07	Reject	2.96E-05	Reject
Inferior Fronto-occipital Fasciculus Right	0.3518	0.3639	0.3945	4.49E-02	Reject	7.53E-08	Reject	1.40E-07	Reject
Inferior Longitudinal Fasciculus Left	0.3021	0.3221	0.3517	1.80E-02	Reject	1.84E-06	Reject	1.11E-05	Reject
Inferior Longitudinal Fasciculus Right	0.3078	0.3305	0.3600	9.41E-03	Reject	1.94E-06	Reject	6.80E-06	Reject
Optic Radiation Left	0.2790	0.2961	0.2975	3.16E-03	Reject	1.74E-03	Reject	6.58E-01	---
Optic Radiation Right	0.2849	0.2989	0.3092	6.74E-03	Reject	3.85E-05	Reject	8.01E-03	Reject
Superior Longitudinal Fasciculus Left	0.2926	0.3051	0.3337	5.98E-02	---	4.74E-06	Reject	5.06E-09	Reject
Superior Longitudinal Fasciculus Right	0.2955	0.3069	0.3482	7.15E-02	---	9.64E-08	Reject	3.34E-14	Reject
Uncinate Fasciculus Left	0.3070	0.3325	0.3786	2.60E-03	Reject	2.31E-10	Reject	2.03E-08	Reject
Uncinate Fasciculus Right	0.3041	0.2943	0.3534	2.09E-01	---	1.65E-06	Reject	1.56E-11	Reject
					10		19		17

Table 5.13: AD T-Test scores: comparing stratum 1+2 group, stratum 3 group and control group

ROI	Stratum 1+2	Stratum 3	Control Group	Stratum 1+2 vs Stratum 3		Stratum 1+2 vs Control		Stratum 3 vs Control	
				T-Test (P-value)	Reject H_0 (if p<0.05)	T-Test (P-value)	Reject H0 (if p<0.05)	T-Test (P-value)	Reject H0 (if p<0.05)
Acoustic Radiation Left	1.151E-03	1.163E-03	1.159E-03	2.25E-01	---	3.23E-01	---	6.98E-01	---
Acoustic Radiation Right	1.181E-03	1.204E-03	1.171E-03	1.09E-01	---	3.96E-01	---	6.77E-03	Reject
Cingulate Gyrus Left	1.136E-03	1.134E-03	1.124E-03	9.26E-01	---	5.52E-01	---	3.94E-01	---
Cingulate Gyrus Right	1.086E-03	1.091E-03	1.072E-03	7.39E-01	---	3.51E-01	---	1.15E-01	---
Cingulum Left*	---	---	---	---	---	---	---	---	---
Cingulum Right*	---	---	---	---	---	---	---	---	---
Corpus Callosum*	---	---	---	---	---	---	---	---	---
Corticospinal Tract Left	1.399E-03	1.389E-03	1.323E-03	6.20E-01	---	7.71E-04	Reject	4.47E-06	Reject
Corticospinal Tract Right	1.387E-03	1.412E-03	1.315E-03	2.85E-01	---	4.25E-03	Reject	1.30E-08	Reject
Forceps Major	1.291E-03	1.368E-03	1.338E-03	5.43E-02	---	1.99E-01	---	2.07E-01	---
Forceps Minor	1.249E-03	1.247E-03	1.219E-03	8.92E-01	---	7.82E-02	---	2.62E-03	Reject
Fornix	1.708E-03	1.707E-03	1.679E-03	9.95E-01	---	6.04E-01	---	4.84E-01	---
Hippocampus Left	1.106E-03	1.106E-03	1.120E-03	9.92E-01	---	2.54E-01	---	2.60E-01	---
Hippocampus Right	1.161E-03	1.161E-03	1.131E-03	9.92E-01	---	1.63E-01	---	1.68E-02	Reject
Inferior Fronto-occipital Fasciculus Left	1.169E-03	1.183E-03	1.204E-03	1.28E-01	---	2.50E-03	Reject	5.76E-02	---
Inferior Fronto-occipital Fasciculus Right	1.185E-03	1.199E-03	1.209E-03	1.77E-01	---	4.12E-02	Reject	2.66E-01	---
Inferior Longitudinal Fasciculus Left	1.115E-03	1.141E-03	1.167E-03	4.17E-03	Reject	1.54E-05	Reject	1.88E-02	Reject
Inferior Longitudinal Fasciculus Right	1.114E-03	1.142E-03	1.150E-03	1.49E-02	Reject	6.17E-03	Reject	4.23E-01	---
Optic Radiation Left	1.088E-03	1.100E-03	1.148E-03	1.76E-01	---	6.22E-07	Reject	1.73E-06	Reject
Optic Radiation Right	1.081E-03	1.099E-03	1.136E-03	3.68E-02	Reject	1.25E-06	Reject	4.73E-06	Reject
Superior Longitudinal Fasciculus Left	1.085E-03	1.089E-03	1.097E-03	3.68E-01	---	9.71E-02	---	2.97E-01	---
Superior Longitudinal Fasciculus Right	1.093E-03	1.106E-03	1.097E-03	9.49E-02	---	6.53E-01	---	2.04E-01	---
Uncinate Fasciculus Left*	---	---	---	---	---	---	---	---	---
Uncinate Fasciculus Right*	---	---	---	---	---	---	---	---	---
					3		8		8

Table 5.14: RD T-Test scores: comparing stratum 1+2 group, stratum 3 group and control group

ROI	Stratum 1+2	Stratum 3	Control Group	Stratum 1+2 vs Stratum 3		Stratum 1+2 vs Control		Stratum 3 vs Control	
				T-Test (P-value)	Reject H_0 (if p<0.05)	T-Test (P-value)	Reject H0 (if p<0.05)	T-Test (P-value)	Reject H0 (if p<0.05)
Acoustic Radiation Left	8.188E-04	8.178E-04	7.684E-04	9.46E-01	---	1.26E-03	Reject	1.63E-04	Reject
Acoustic Radiation Right*	---	---	---	---	---	---	---	---	---
Cingulate Gyrus Left	6.984E-04	6.765E-04	6.469E-04	1.55E-01	---	2.56E-03	Reject	1.51E-03	Reject
Cingulate Gyrus Right	7.270E-04	7.056E-04	6.763E-04	2.43E-01	---	9.11E-03	Reject	6.56E-03	Reject
Cingulum Left	7.004E-04	6.727E-04	6.743E-04	5.09E-02	---	6.41E-02	---	8.49E-01	---
Cingulum Right	6.889E-04	6.592E-04	6.589E-04	1.09E-01	---	1.04E-01	---	9.78E-01	---
Corpus Callosum*	---	---	---	---	---	---	---	---	---
Corticospinal Tract Left	7.195E-04	7.391E-04	6.523E-04	3.72E-01	---	3.11E-03	Reject	1.96E-06	Reject
Corticospinal Tract Right	6.972E-04	7.511E-04	6.517E-04	4.21E-02	Reject	5.57E-02	---	5.02E-07	Reject
Forceps Major	6.753E-04	7.094E-04	7.288E-04	2.43E-01	---	5.64E-02	---	3.30E-01	---
Forceps Minor	7.393E-04	7.151E-04	6.903E-04	5.28E-02	---	3.87E-04	Reject	4.78E-03	Reject
Fornix	1.132E-03	1.151E-03	1.093E-03	7.77E-01	---	5.58E-01	---	1.76E-01	---
Hippocampus Left	7.495E-04	7.574E-04	7.602E-04	5.87E-01	---	4.06E-01	---	8.44E-01	---
Hippocampus Right	8.051E-04	7.872E-04	7.596E-04	4.85E-01	---	8.97E-02	---	3.26E-02	Reject
Inferior Fronto-occipital Fasciculus Left	6.641E-04	6.443E-04	6.526E-04	2.58E-02	Reject	1.89E-01	---	1.81E-01	---
Inferior Fronto-occipital Fasciculus Right	6.660E-04	6.604E-04	6.555E-04	5.61E-01	---	3.49E-01	---	5.07E-01	---
Inferior Longitudinal Fasciculus Left	6.770E-04	6.678E-04	6.884E-04	3.28E-01	---	2.25E-01	---	6.53E-03	Reject
Inferior Longitudinal Fasciculus Right	6.622E-04	6.550E-04	6.722E-04	3.29E-01	---	2.74E-01	---	1.16E-02	Reject
Optic Radiation Left	6.985E-04	6.910E-04	7.276E-04	3.23E-01	---	6.97E-04	Reject	4.24E-07	Reject
Optic Radiation Right	6.874E-04	6.850E-04	7.088E-04	7.65E-01	---	1.68E-02	Reject	2.38E-04	Reject
Superior Longitudinal Fasciculus Left	6.888E-04	6.773E-04	6.779E-04	1.70E-01	---	1.92E-01	---	9.16E-01	---
Superior Longitudinal Fasciculus Right	6.938E-04	6.826E-04	6.624E-04	2.14E-01	---	2.33E-03	Reject	1.47E-03	Reject
Uncinate Fasciculus Left	7.488E-04	7.414E-04	6.782E-04	6.49E-01	---	1.12E-04	Reject	5.49E-06	Reject
Uncinate Fasciculus Right	7.597E-04	7.927E-04	7.146E-04	7.63E-02	---	2.24E-02	Reject	7.80E-11	Reject
					2		10		14

5.2.3   Symptomatic versus Symptom-Free

As a follow up to the longitudinal analysis summarized in Section 5.1.2, mTBI patients were subdivided into two groups based on symptom status at the time of scanning. Welch's t-tests were conducted between the scans that occurred while the patient was symptomatic (initial scan; n=26) versus scans occuring post symptom-resolution (follow up scan; n=9). On average, the follow up scans occured approximately 157 days post-injury and 74 days post symptom-resolution. The results for FA, AD and RD are presented in Tables 5.15, 5.16 and 5.17, respectively. Surprisingly, there was only a single instance in which a significant difference was found between the symptomatic and post symptom-resolution groups. The RD in the forceps minor region (Table 5.17) showed a disparity between the symptomatic group relative to both the symptom free and control data.

Furthermore, both FA and AD T-test results showed the symptomatic group was significantly different from the control group in more ROIs relative to the symptom free group versus the control group (19 compared to 15 for FA and 9 compared to 4 for AD). This was not the case for RD as both mTBI subgroups identified 12 disparities relative to the control population. These results suggest that the DTI metrics were ineffective at identifying whether or not a patient was still experiencing symptoms of mTBI. More specifically, the results show that brain microstructure stayed relatively constant over the first six months post-injury. Perhaps this time frame was not sufficient to allow the brain to fully repair its microstructure. As previously eluded to, it would be interesting to rescan mTBI patients 12 months post symptom-resolution to see if the brain did continue to repair its microstructure or if it remained unchanged from the follow-up scans analyzed in this thesis.

Table 5.15: FA T-Test scores: comparing symptomatic, symptom-free and control groups

ROI	Initial Scan	Follow-up Scan	Control Group	Initial vs Follow-up Scan		Initial Scan vs Control		Follow-up Scan vs Control	
				T-Test (P-value)	Reject H₀ (if p<0.05)	T-Test (P-value)	Reject H0 (if p<0.05)	T-Test (P-value)	Reject H0 (if p<0.05)
Acoustic Radiation Left	0.2559	0.2570	0.2844	9.11E-01	---	1.23E-05	Reject	1.04E-02	Reject
Acoustic Radiation Right	0.2480	0.2574	0.2724	2.16E-01	---	2.01E-04	Reject	3.76E-02	Reject
Cingulate Gyrus Left	0.3363	0.3421	0.3609	7.21E-01	---	1.11E-02	Reject	2.34E-01	---
Cingulate Gyrus Right	0.2751	0.2845	0.3095	5.90E-01	---	3.22E-03	Reject	1.49E-01	---
Cingulum Left	0.3294	0.3409	0.3455	5.22E-01	---	1.32E-01	---	7.83E-01	---
Cingulum Right	0.3401	0.3404	0.3580	9.85E-01	---	1.14E-01	---	2.94E-01	---
Corpus Callosum	0.3998	0.4084	0.4076	3.47E-01	---	2.38E-01	---	9.27E-01	---
Corticospinal Tract Left	0.4445	0.4340	0.4713	1.87E-01	---	2.81E-05	Reject	9.79E-05	Reject
Corticospinal Tract Right	0.4437	0.4317	0.4652	2.20E-01	---	6.67E-04	Reject	2.53E-03	Reject
Forceps Major	0.3938	0.3934	0.3871	9.80E-01	---	5.04E-01	---	6.48E-01	---
Forceps Minor	0.3540	0.3646	0.3770	3.32E-01	---	3.08E-04	Reject	2.53E-01	---
Fornix	0.2860	0.2882	0.2999	8.73E-01	---	1.49E-01	---	3.65E-01	---
Hippocampus Left	0.2386	0.2242	0.2652	1.96E-01	---	5.22E-03	Reject	6.89E-04	Reject
Hippocampus Right	0.2527	0.2393	0.2764	2.26E-01	---	5.51E-03	Reject	2.97E-03	Reject
Inferior Fronto-occipital Fasciculus Left	0.3651	0.3711	0.3978	4.71E-01	---	1.77E-07	Reject	3.71E-03	Reject
Inferior Fronto-occipital Fasciculus Right	0.3598	0.3609	0.3945	8.38E-01	---	1.17E-08	Reject	7.05E-07	Reject
Inferior Longitudinal Fasciculus Left	0.3136	0.3220	0.3517	3.60E-01	---	8.13E-08	Reject	3.54E-03	Reject
Inferior Longitudinal Fasciculus Right	0.3208	0.3309	0.3600	2.03E-01	---	9.26E-08	Reject	8.09E-04	Reject
Optic Radiation Left	0.2895	0.2942	0.2975	3.64E-01	---	3.49E-02	Reject	4.93E-01	---
Optic Radiation Right	0.2942	0.2953	0.3092	8.18E-01	---	4.34E-04	Reject	9.19E-03	Reject
Superior Longitudinal Fasciculus Left	0.3003	0.3040	0.3337	6.26E-01	---	3.68E-11	Reject	1.84E-03	Reject
Superior Longitudinal Fasciculus Right	0.3037	0.3023	0.3482	8.22E-01	---	1.78E-14	Reject	1.08E-06	Reject
Uncinate Fasciculus Left	0.3257	0.3211	0.3786	6.11E-01	---	9.79E-10	Reject	3.80E-06	Reject
Uncinate Fasciculus Right	0.2998	0.2903	0.3534	1.77E-01	---	3.64E-10	Reject	1.09E-09	Reject
TOTAL					0		19		15

Table 5.16: AD T-Test scores: comparing symptomatic, symptom-free and control groups

ROI	Initial Scan	Follow-up Scan	Control Group	Initial vs Follow-up Scan		Initial Scan vs Control		Follow-up Scan vs Control	
				T-Test (P-value)	Reject H_0 (if p<0.05)	T-Test (P-value)	Reject H0 (if p<0.05)	T-Test (P-value)	Reject H0 (if p<0.05)
Acoustic Radiation Left	1.161E-03	1.153E-03	1.159E-03	5.11E-01	---	7.96E-01	---	6.31E-01	---
Acoustic Radiation Right	1.202E-03	1.181E-03	1.171E-03	1.31E-01	---	7.75E-03	Reject	3.87E-01	---
Cingulate Gyrus Left	1.132E-03	1.140E-03	1.124E-03	5.18E-01	---	5.15E-01	---	1.77E-01	---
Cingulate Gyrus Right	1.091E-03	1.084E-03	1.072E-03	6.37E-01	---	1.00E-01	---	4.76E-01	---
Cingulum Left*	1.164E-03	1.155E-03	1.137E-03	---	---	---	---	---	---
Cingulum Right*	1.179E-03	1.147E-03	1.139E-03	---	---	---	---	---	---
Corpus Callosum*	1.442E-03	1.404E-03	1.438E-03	---	---	---	---	---	---
Corticospinal Tract Left	1.400E-03	1.370E-03	1.323E-03	2.26E-01	---	6.80E-09	Reject	8.12E-02	---
Corticospinal Tract Right	1.409E-03	1.392E-03	1.315E-03	4.88E-01	---	2.34E-08	Reject	6.13E-03	Reject
Forceps Major	1.356E-03	1.308E-03	1.338E-03	2.47E-01	---	4.52E-01	---	4.39E-01	---
Forceps Minor	1.251E-03	1.236E-03	1.219E-03	1.86E-01	---	1.87E-03	Reject	1.18E-01	---
Fornix	1.713E-03	1.691E-03	1.679E-03	7.24E-01	---	3.90E-01	---	8.39E-01	---
Hippocampus Left	1.108E-03	1.099E-03	1.120E-03	5.44E-01	---	3.19E-01	---	1.76E-01	---
Hippocampus Right	1.158E-03	1.167E-03	1.131E-03	6.40E-01	---	3.68E-02	Reject	5.21E-02	---
Inferior Fronto-occipital Fasciculus Left	1.178E-03	1.180E-03	1.204E-03	8.53E-01	---	1.47E-02	Reject	9.69E-02	---
Inferior Fronto-occipital Fasciculus Right	1.196E-03	1.189E-03	1.209E-03	5.13E-01	---	1.70E-01	---	1.05E-01	---
Inferior Longitudinal Fasciculus Left	1.132E-03	1.134E-03	1.167E-03	8.83E-01	---	1.95E-03	Reject	2.32E-02	Reject
Inferior Longitudinal Fasciculus Right	1.131E-03	1.141E-03	1.150E-03	4.28E-01	---	6.14E-02	---	4.92E-01	---
Optic Radiation Left	1.099E-03	1.090E-03	1.148E-03	4.57E-01	---	2.26E-07	Reject	2.85E-04	Reject
Optic Radiation Right	1.095E-03	1.089E-03	1.136E-03	4.36E-01	---	1.29E-06	Reject	2.01E-06	Reject
Superior Longitudinal Fasciculus Left	1.090E-03	1.081E-03	1.097E-03	1.58E-01	---	3.35E-01	---	6.06E-02	---
Superior Longitudinal Fasciculus Right	1.105E-03	1.094E-03	1.097E-03	1.25E-01	---	2.81E-01	---	7.03E-01	---
Uncinate Fasciculus Left*	1.200E-03	1.191E-03	1.192E-03	---	---	---	---	---	---
Uncinate Fasciculus Right*	1.228E-03	1.214E-03	1.214E-03	---	---	---	---	---	---
TOTAL					0		9		4

Table 5.17: RD T-Test scores: comparing symptomatic, symptom-free and control groups

ROI	Initial Scan	Follow-up Scan	Control Group	Initial vs Follow-up Scan		Initial Scan vs Control		Follow-up Scan vs Control	
				T-Test (P-value)	Reject H₀ (if p<0.05)	T-Test (P-value)	Reject H0 (if p<0.05)	T-Test (P-value)	Reject H0 (if p<0.05)
Acoustic Radiation Left	8.201E-04	8.124E-04	7.684E-04	6.65E-01	---	2.68E-05	Reject	2.03E-02	Reject
Acoustic Radiation Right*	8.585E-04	8.393E-04	8.000E-04	---	---	---	---	---	---
Cingulate Gyrus Left	6.859E-04	6.760E-04	6.469E-04	4.72E-01	---	1.49E-04	Reject	3.35E-02	Reject
Cingulate Gyrus Right	7.149E-04	7.049E-04	6.763E-04	5.82E-01	---	7.34E-04	Reject	1.10E-01	---
Cingulum Left	6.866E-04	6.663E-04	6.743E-04	1.63E-01	---	1.82E-01	---	5.63E-01	---
Cingulum Right	6.718E-04	6.590E-04	6.589E-04	4.27E-01	---	2.35E-01	---	9.97E-01	---
Corpus Callosum*	7.853E-04	7.442E-04	7.828E-04	---	---	---	---	---	---
Corticospinal Tract Left	7.353E-04	7.260E-04	6.523E-04	7.26E-01	---	7.92E-07	Reject	1.34E-02	Reject
Corticospinal Tract Right	7.336E-04	7.358E-04	6.517E-04	9.43E-01	---	9.06E-06	Reject	1.36E-02	Reject
Forceps Major	7.073E-04	6.739E-04	7.288E-04	2.11E-01	---	2.87E-01	---	3.08E-02	Reject
Forceps Minor	7.303E-04	7.007E-04	6.903E-04	3.77E-02	Reject	5.04E-06	Reject	4.22E-01	---
Fornix	1.150E-03	1.131E-03	1.093E-03	7.70E-01	---	1.89E-01	---	5.69E-01	---
Hippocampus Left	7.576E-04	7.472E-04	7.602E-04	5.76E-01	---	8.42E-01	---	4.76E-01	---
Hippocampus Right	7.901E-04	8.008E-04	7.596E-04	6.22E-01	---	3.77E-02	Reject	6.27E-02	---
Inferior Fronto-occipital Fasciculus Left	6.534E-04	6.422E-04	6.526E-04	1.80E-01	---	9.01E-01	---	2.16E-01	---
Inferior Fronto-occipital Fasciculus Right	6.633E-04	6.588E-04	6.555E-04	5.87E-01	---	3.16E-01	---	7.36E-01	---
Inferior Longitudinal Fasciculus Left	6.750E-04	6.582E-04	6.884E-04	7.11E-02	---	6.64E-02	---	3.05E-03	Reject
Inferior Longitudinal Fasciculus Right	6.593E-04	6.511E-04	6.722E-04	9.45E-02	---	7.09E-02	---	3.46E-03	Reject
Optic Radiation Left	6.961E-04	6.853E-04	7.276E-04	1.94E-01	---	3.97E-06	Reject	7.30E-05	Reject
Optic Radiation Right	6.873E-04	6.812E-04	7.088E-04	3.55E-01	---	1.15E-03	Reject	4.07E-04	Reject
Superior Longitudinal Fasciculus Left	6.830E-04	6.750E-04	6.779E-04	3.33E-01	---	3.92E-01	---	7.18E-01	---
Superior Longitudinal Fasciculus Right	6.878E-04	6.814E-04	6.624E-04	4.37E-01	---	1.77E-04	Reject	2.82E-02	Reject
Uncinate Fasciculus Left	7.461E-04	7.369E-04	6.782E-04	6.29E-01	---	2.20E-07	Reject	6.06E-03	Reject
Uncinate Fasciculus Right	7.820E-04	7.831E-04	7.146E-04	9.47E-01	---	1.76E-07	Reject	6.77E-04	Reject
TOTAL					1		12		12

5.2.4   Demographics

Further T-test analysis was performed focusing on the demographics of the mTBI sample. The objective was to determine if any external factors (apart from having sustained a mTBI) contributed to disparities observed between the mTBI and control group. This section examined the impact of age and gender on the efficacy of using FA, AD and RD measurements to identify abnormal ROIs within the brain.

Age Groups

The mTBI group was split into two subgroups based on the subject's age. Independent samples Welch's T-tests were performed (for each DTI metric) between patients who were 10 to 13 years old (n=12) and patients who were 14 to 17 years old (n=23). Additional T-tests were also performed to compare each age-range subgroup to the control population. The results for FA, AD and RD are summarized in Tables 5.18, 5.19 and 5.20, respectively.

Looking at FA (Table 5.18, significant differences were found between then 10-13 and 14-17 age groups in 16 of the 24 regions. However, in nine of those 16 instances both age groups were still significantly different relative to the control data. One fascinating observation was that, in six of these 16 regions, the younger age group differed from the control population where as the older age group did not. The six regions were comprised of the cingulate gyrus, cingulum, corpus callosum and left optic radiation. With the exception of optic radiation, these ROIs are all representative of deeper, inner brain structures. Another noteworthy result was that the FA was relatively less in the younger group relative to the older group in 22 of the 24 regions. As previously mentioned, a decrease in FA could indicate reduced WM integrity as a

result of injury.

As shown in Table 5.19, in terms of AD, only four regions were found to be significantly different between the two age groups (inferior longitudinal fasciculus and optic radiation). Overall neither of the age groups had a clear advantage when differentiating between mTBI and control populations, however, one pattern did emerge. Save for the left corticospinal tract, the AD was lower in the 10-13 age group relative to the 14-17 age group in every region. This varied from our findings when comparing the mTBI group as a whole to the control data. Referring to Table 5.8, AD was found to be lower in the mTBI group in only eight regions.

Table 5.20 shows that the RD was significantly different between the two age groups in eight regions. Similar to FA, three of the eight instances were found in the deep brain structures of the right cingulate gyrus and cingulum. In those regions, a disparity was observed between the younger age group and the control group where as the older age group was fairly similar to the controls. In addition, AD for the 10-13 year-olds was greater than for the 14-17 year-olds in all but four of the ROIs.

Based on this analysis, the subject's age may factor into differences observed between the mTBI and control population for certain regions. Further, the younger age groups appear to be more sensitive to mTBI which results in more significant microstructural abnormalities observed. It appears that these abnormalities were also prevalent within the deeper brain regions such as the cingulum, cingulate gyrus and corpus callosum - areas which were mostly unaffected in the older age group. Intriguingly, the only ROI which was unaffected by age was the corticospinal tract. Regardless of the DTI metric, the two age groups were found to be relatively similar to each other and both differed significantly from the control data for that ROI.

Table 5.18: FA T-Test scores: comparing age 10 to 13, age 14-17 and control groups

ROI	10-13	14-17	Control Group	10-13 vs 14-17		10-13 vs Control		14-17 vs Control	
				T-Test (P-value)	Reject H_0 (if p<0.05)	T-Test (P-value)	Reject H0 (if p<0.05)	T-Test (P-value)	Reject H0 (if p<0.05)
Acoustic Radiation Left	0.2443	0.2624	0.2844	4.44E-02	Reject	1.29E-04	Reject	2.73E-04	Reject
Acoustic Radiation Right	0.2400	0.2558	0.2724	8.67E-02	---	1.43E-03	Reject	4.04E-03	Reject
Cingulate Gyrus Left	0.3081	0.3533	0.3609	2.98E-03	Reject	7.96E-04	Reject	3.46E-01	---
Cingulate Gyrus Right	0.2428	0.2957	0.3095	6.56E-05	Reject	3.99E-07	Reject	2.09E-01	---
Cingulum Left	0.2895	0.3547	0.3455	6.34E-05	Reject	2.90E-04	Reject	2.75E-01	---
Cingulum Right	0.3011	0.3605	0.3580	4.56E-05	Reject	7.84E-05	Reject	7.98E-01	---
Corpus Callosum	0.3858	0.4105	0.4076	3.77E-03	Reject	1.02E-02	Reject	6.38E-01	---
Corticospinal Tract Left	0.4326	0.4466	0.4713	8.61E-02	---	3.21E-05	Reject	1.07E-04	Reject
Corticospinal Tract Right	0.4387	0.4416	0.4652	7.14E-01	---	1.39E-04	Reject	1.44E-03	Reject
Forceps Major	0.3686	0.4068	0.3871	6.51E-03	Reject	1.79E-01	---	2.82E-02	Reject
Forceps Minor	0.3471	0.3618	0.3770	1.14E-01	---	2.30E-03	Reject	1.75E-02	Reject
Fornix	0.2934	0.2830	0.2999	4.40E-01	---	6.08E-01	---	8.05E-02	---
Hippocampus Left	0.2238	0.2407	0.2652	1.75E-01	---	1.87E-03	Reject	8.39E-03	Reject
Hippocampus Right	0.2348	0.2568	0.2764	4.23E-02	Reject	4.90E-04	Reject	1.85E-02	Reject
Inferior Fronto-occipital Fasciculus Left	0.3485	0.3761	0.3978	1.18E-04	Reject	1.66E-08	Reject	4.64E-05	Reject
Inferior Fronto-occipital Fasciculus Right	0.3528	0.3639	0.3945	7.78E-02	---	2.94E-07	Reject	1.30E-07	Reject
Inferior Longitudinal Fasciculus Left	0.2992	0.3244	0.3517	1.83E-03	Reject	7.84E-08	Reject	3.01E-05	Reject
Inferior Longitudinal Fasciculus Right	0.3107	0.3300	0.3600	2.58E-02	Reject	3.27E-06	Reject	8.01E-06	Reject
Optic Radiation Left	0.2760	0.2984	0.2975	6.42E-07	Reject	8.90E-07	Reject	7.73E-01	---
Optic Radiation Right	0.2823	0.3009	0.3092	9.08E-05	Reject	4.62E-07	Reject	2.35E-02	Reject
Superior Longitudinal Fasciculus Left	0.2883	0.3079	0.3337	8.64E-04	Reject	8.25E-09	Reject	2.85E-08	Reject
Superior Longitudinal Fasciculus Right	0.2919	0.3093	0.3482	6.01E-03	Reject	7.95E-09	Reject	4.38E-15	Reject
Uncinate Fasciculus Left	0.3093	0.3325	0.3786	2.03E-02	Reject	2.90E-07	Reject	3.45E-09	Reject
Uncinate Fasciculus Right	0.3008	0.2956	0.3534	4.32E-01	---	6.46E-10	Reject	3.52E-10	Reject
TOTAL					16		22		17

Table 5.19: AD T-Test scores: comparing age 10 to 13, age 14-17 and control groups

ROI	10-13	14-17	Control Group	10-13 vs 14-17 T-Test (P-value)	Reject H0 (if p<0.05)	10-13 vs Control T-Test (P-value)	Reject H0 (if p<0.05)	14-17 vs Control T-Test (P-value)	Reject H0 (if p<0.05)
Acoustic Radiation Left	1.148E-03	1.165E-03	1.159E-03	9.13E-02	---	2.07E-01	---	5.26E-01	---
Acoustic Radiation Right	1.189E-03	1.201E-03	1.171E-03	4.68E-01	---	1.71E-01	---	1.50E-02	Reject
Cingulate Gyrus Left	1.127E-03	1.138E-03	1.124E-03	5.52E-01	---	8.70E-01	---	2.02E-01	---
Cingulate Gyrus Right	1.078E-03	1.095E-03	1.072E-03	1.86E-01	---	6.43E-01	---	5.98E-02	---
Cingulum Left*	1.135E-03	1.176E-03	1.137E-03	---	---		---		---
Cingulum Right*	1.153E-03	1.180E-03	1.139E-03		---		---		---
Corpus Callosum*	1.413E-03	1.442E-03	1.438E-03		---		---		---
Corticospinal Tract Left	1.405E-03	1.386E-03	1.323E-03	2.66E-01	---	6.22E-05	Reject	2.31E-05	Reject
Corticospinal Tract Right	1.390E-03	1.411E-03	1.315E-03	3.39E-01	---	2.08E-03	Reject	2.56E-08	Reject
Forceps Major	1.304E-03	1.365E-03	1.338E-03	1.21E-01	---	3.42E-01	---	2.70E-01	---
Forceps Minor	1.238E-03	1.252E-03	1.219E-03	3.88E-01	---	2.22E-01	---	2.48E-04	Reject
Fornix	1.682E-03	1.721E-03	1.679E-03	4.91E-01	---	9.60E-01	---	3.08E-01	---
Hippocampus Left	1.095E-03	1.112E-03	1.120E-03	2.45E-01	---	7.32E-02	---	4.91E-01	---
Hippocampus Right	1.160E-03	1.161E-03	1.131E-03	9.63E-01	---	1.76E-01	---	1.25E-02	Reject
Inferior Fronto-occipital Fasciculus Left	1.168E-03	1.184E-03	1.204E-03	9.00E-02	---	1.55E-03	Reject	7.17E-02	---
Inferior Fronto-occipital Fasciculus Right	1.188E-03	1.197E-03	1.209E-03	3.53E-01	---	6.73E-02	---	2.23E-01	---
Inferior Longitudinal Fasciculus Left	1.116E-03	1.142E-03	1.167E-03	2.17E-03	Reject	8.16E-06	Reject	2.49E-02	Reject
Inferior Longitudinal Fasciculus Right	1.119E-03	1.141E-03	1.150E-03	4.89E-02	Reject	1.52E-02	Reject	3.64E-01	---
Optic Radiation Left	1.083E-03	1.103E-03	1.148E-03	2.55E-02	Reject	4.47E-08	Reject	5.11E-06	Reject
Optic Radiation Right	1.080E-03	1.100E-03	1.136E-03	1.86E-02	Reject	2.67E-07	Reject	8.38E-06	Reject
Superior Longitudinal Fasciculus Left	1.084E-03	1.090E-03	1.097E-03	3.36E-01	---	1.02E-01	---	3.17E-01	---
Superior Longitudinal Fasciculus Right	1.095E-03	1.106E-03	1.097E-03	1.47E-01	---	8.05E-01	---	2.31E-01	---
Uncinate Fasciculus Left*	1.184E-03	1.205E-03	1.192E-03	---	---		---		---
Uncinate Fasciculus Right*	1.223E-03	1.225E-03	1.214E-03	---	---		---		---
TOTAL					4		7		8

Table 5.20: RD T-Test scores: comparing age 10 to 13, age 14-17 and control groups

ROI	10-13	14-17	Control Group	10-13 vs 14-17		10-13 vs Control		14-17 vs Control	
				T-Test (P-value)	Reject H_0 (if p<0.05)	T-Test (P-value)	Reject H0 (if p<0.05)	T-Test (P-value)	Reject H0 (if p<0.05)
Acoustic Radiation Left	8.292E-04	8.123E-04	7.684E-04	2.57E-01	---	1.03E-04	Reject	7.40E-04	Reject
Acoustic Radiation Right*	8.613E-04	8.496E-04	8.000E-04	---	---	---	---	---	---
Cingulate Gyrus Left	7.113E-04	6.688E-04	6.469E-04	2.05E-03	Reject	2.57E-05	Reject	1.20E-02	Reject
Cingulate Gyrus Right	7.462E-04	6.947E-04	6.763E-04	4.85E-05	Reject	4.72E-10	Reject	1.03E-01	---
Cingulum Left	7.118E-04	6.655E-04	6.743E-04	2.49E-05	Reject	2.81E-04	Reject	3.11E-01	---
Cingulum Right	7.064E-04	6.488E-04	6.589E-04	1.40E-06	Reject	4.77E-06	Reject	3.18E-01	---
Corpus Callosum*	7.806E-04	7.717E-04	7.828E-04	---	---	---	---	---	---
Corticospinal Tract Left	7.478E-04	7.251E-04	6.523E-04	2.53E-01	---	5.42E-06	Reject	9.66E-05	Reject
Corticospinal Tract Right	7.193E-04	7.419E-04	6.517E-04	3.39E-01	---	1.59E-03	Reject	2.92E-05	Reject
Forceps Major	6.939E-04	7.012E-04	7.288E-04	8.00E-01	---	1.89E-01	---	1.80E-01	---
Forceps Minor	7.412E-04	7.130E-04	6.903E-04	1.85E-02	Reject	8.80E-05	Reject	9.39E-03	Reject
Fornix	1.118E-03	1.160E-03	1.093E-03	5.21E-01	---	6.89E-01	---	1.31E-01	---
Hippocampus Left	7.522E-04	7.564E-04	7.602E-04	7.61E-01	---	4.79E-01	---	7.97E-01	---
Hippocampus Right	8.152E-04	7.812E-04	7.596E-04	1.54E-01	---	2.67E-02	Reject	9.02E-02	---
Inferior Fronto-occipital Fasciculus Left	6.688E-04	6.410E-04	6.526E-04	4.01E-04	Reject	3.23E-02	Reject	5.71E-02	---
Inferior Fronto-occipital Fasciculus Right	6.669E-04	6.597E-04	6.555E-04	4.19E-01	---	2.80E-01	---	5.75E-01	---
Inferior Longitudinal Fasciculus Left	6.797E-04	6.660E-04	6.884E-04	1.22E-01	---	3.07E-01	---	3.82E-03	Reject
Inferior Longitudinal Fasciculus Right	6.600E-04	6.558E-04	6.722E-04	5.58E-01	---	1.82E-01	---	1.54E-02	Reject
Optic Radiation Left	6.985E-04	6.906E-04	7.276E-04	2.73E-01	---	2.41E-04	Reject	6.81E-07	Reject
Optic Radiation Right	6.894E-04	6.838E-04	7.088E-04	4.65E-01	---	2.27E-02	Reject	1.31E-04	Reject
Superior Longitudinal Fasciculus Left	6.923E-04	6.750E-04	6.779E-04	3.06E-02	Reject	6.96E-02	---	6.03E-01	---
Superior Longitudinal Fasciculus Right	6.988E-04	6.796E-04	6.624E-04	3.15E-02	Reject	4.00E-04	Reject	4.15E-03	Reject
Uncinate Fasciculus Left	7.584E-04	7.360E-04	6.782E-04	1.39E-01	---	1.02E-06	Reject	4.28E-05	Reject
Uncinate Fasciculus Right	7.833E-04	7.818E-04	7.146E-04	9.23E-01	---	5.71E-05	Reject	7.40E-07	Reject
TOTAL					8		15		12

80

Gender Groups

In order to look at the effect gender had on our analysis, independent samples Welch's T-tests were performed (for each DTI metric) between female (n=22) and male (n=13) subjects within the mTBI group. Additional T-tests were also performed to compare each gender subgroup to the control population. The results for FA, AD and RD are summarized in Tables 5.21, 5.22 and 5.23, respectively.

Significant differences were observed in 15 regions based on FA. In six of those 15 regions, only the male subgroup differed from the control data. Such was the case for the cingulate gyrus, cingulum and corpus callosum - all relatively deep brain regions. Further, $p < 0.05$ for the male data in 22 cases compared to 15 for the female data. The overall trend in the data was that FA was found to be greater in females for every region other than the right uncinate fasciculus. Overall, it would appear that gender does bias the results when looking at FA measurements.

Only two regions, the left and right acoustic radiation, were found to be significantly different in terms of AD between female and male subgroups. In 18 of 24 regions, mean AD was greater in females when compared to males. Overall, it appeared that AD was equally effective at identifying mTBI data regardless of gender.

Looking at RD, 10 regions differed significantly between the two genders. Five of those 10 regions were still different from the control group for both gender groups. Following the trend observed for FA, the deep brain regions of the cingulate gyrus and cingulum differed for the male group relative to the controls and not for the female group. Additionally, RD values were consistently less in the females relative to the males in every ROI other than the acoustic radiation and right uncinate fasiciculus.

Table 5.21: FA T-Test scores: comparing male, female and control groups

ROI	Female	Male	Control Group	Female vs Male T-Test (P-value)	Female vs Male Reject H0 (if p<0.05)	Female vs Control T-Test (P-value)	Female vs Control Reject H0 (if p<0.05)	Male vs Control T-Test (P-value)	Male vs Control Reject H0 (if p<0.05)
Acoustic Radiation Left	0.2633	0.2442	0.2844	2.99E-02	Reject	4.16E-04	Reject	6.50E-05	Reject
Acoustic Radiation Right	0.2558	0.2411	0.2724	1.01E-01	---	4.20E-03	Reject	1.38E-03	Reject
Cingulate Gyrus Left	0.3452	0.3253	0.3609	1.74E-01	---	9.69E-02	---	1.44E-02	Reject
Cingulate Gyrus Right	0.2936	0.2504	0.3095	3.23E-03	Reject	1.56E-01	---	7.03E-05	Reject
Cingulum Left	0.3448	0.3113	0.3455	4.69E-02	Reject	9.41E-01	---	3.46E-02	Reject
Cingulum Right	0.3545	0.3158	0.3580	1.13E-02	Reject	7.46E-01	---	5.69E-03	Reject
Corpus Callosum	0.4118	0.3855	0.4076	7.64E-04	Reject	5.06E-01	---	3.82E-03	Reject
Corticospinal Tract Left	0.4451	0.4362	0.4713	2.12E-01	---	3.03E-04	Reject	2.92E-07	Reject
Corticospinal Tract Right	0.4424	0.4375	0.4652	4.99E-01	---	4.13E-03	Reject	1.12E-08	Reject
Forceps Major	0.4048	0.3748	0.3871	7.15E-03	Reject	8.73E-02	---	2.51E-01	---
Forceps Minor	0.3663	0.3405	0.3770	4.40E-03	Reject	6.54E-02	---	1.70E-04	Reject
Fornix	0.2923	0.2769	0.2999	2.52E-01	---	4.16E-01	---	8.03E-02	---
Hippocampus Left	0.2458	0.2164	0.2652	1.43E-02	Reject	2.90E-02	Reject	1.46E-04	Reject
Hippocampus Right	0.2584	0.2339	0.2764	1.54E-02	Reject	3.36E-02	Reject	8.23E-05	Reject
Inferior Fronto-occipital Fasciculus Left	0.3749	0.3527	0.3978	1.31E-03	Reject	1.26E-04	Reject	8.22E-09	Reject
Inferior Fronto-occipital Fasciculus Right	0.3620	0.3569	0.3945	4.18E-01	---	6.44E-08	Reject	1.78E-06	Reject
Inferior Longitudinal Fasciculus Left	0.3233	0.3031	0.3517	1.96E-02	Reject	1.78E-05	Reject	2.47E-06	Reject
Inferior Longitudinal Fasciculus Right	0.3244	0.3217	0.3600	7.68E-01	---	4.26E-07	Reject	2.86E-04	Reject
Optic Radiation Left	0.2975	0.2792	0.2975	6.49E-05	Reject	9.97E-01	---	3.88E-05	Reject
Optic Radiation Right	0.3007	0.2840	0.3092	9.44E-05	Reject	3.24E-02	Reject	3.63E-08	Reject
Superior Longitudinal Fasciculus Left	0.3056	0.2937	0.3337	5.56E-02	---	2.14E-08	Reject	6.98E-07	Reject
Superior Longitudinal Fasciculus Right	0.3079	0.2956	0.3482	3.73E-02	Reject	3.61E-13	Reject	2.26E-09	Reject
Uncinate Fasciculus Left	0.3312	0.3133	0.3786	7.58E-02	---	2.14E-09	Reject	9.62E-07	Reject
Uncinate Fasciculus Right	0.2951	0.3012	0.3534	3.72E-01	---	4.75E-10	Reject	9.67E-10	Reject
TOTAL					14		15		22

Table 5.22: AD T-Test scores: comparing male, female and control groups

ROI	Female	Male	Control Group	Female vs Male		Female vs Control		Male vs Control	
				T-Test (P-value)	Reject H$_0$ (if p<0.05)	T-Test (P-value)	Reject H0 (if p<0.05)	T-Test (P-value)	Reject H0 (if p<0.05)
Acoustic Radiation Left	1.169E-03	1.142E-03	1.159E-03	7.78E-03	Reject	2.90E-01	---	4.95E-02	Reject
Acoustic Radiation Right	1.210E-03	1.175E-03	1.171E-03	2.05E-02	Reject	1.75E-03	Reject	7.42E-01	---
Cingulate Gyrus Left	1.132E-03	1.139E-03	1.124E-03	6.68E-01	---	5.11E-01	---	3.91E-01	---
Cingulate Gyrus Right	1.098E-03	1.075E-03	1.072E-03	8.11E-02	---	3.07E-02	Reject	8.41E-01	---
Cingulum Left*	1.165E-03	1.156E-03	1.137E-03	---	---	---	---	---	---
Cingulum Right*	1.172E-03	1.169E-03	1.139E-03	---	---	---	---	---	---
Corpus Callosum*	1.424E-03	1.446E-03	1.438E-03	---	---	---	---	---	---
Corticospinal Tract Left	1.380E-03	1.412E-03	1.323E-03	7.60E-02	---	3.79E-05	Reject	2.85E-05	Reject
Corticospinal Tract Right	1.405E-03	1.402E-03	1.315E-03	8.90E-01	---	1.85E-07	Reject	4.51E-04	Reject
Forceps Major	1.342E-03	1.347E-03	1.338E-03	8.99E-01	---	8.66E-01	---	7.89E-01	---
Forceps Minor	1.249E-03	1.244E-03	1.219E-03	7.05E-01	---	1.06E-03	Reject	9.84E-02	---
Fornix	1.684E-03	1.747E-03	1.679E-03	3.06E-01	---	8.99E-01	---	2.67E-01	---
Hippocampus Left	1.109E-03	1.102E-03	1.120E-03	6.40E-01	---	3.45E-01	---	1.93E-01	---
Hippocampus Right	1.155E-03	1.171E-03	1.131E-03	4.19E-01	---	6.25E-02	---	3.74E-02	Reject
Inferior Fronto-occipital Fasciculus Left	1.183E-03	1.171E-03	1.204E-03	2.13E-01	---	6.35E-02	---	2.68E-03	Reject
Inferior Fronto-occipital Fasciculus Right	1.196E-03	1.192E-03	1.209E-03	6.32E-01	---	1.84E-01	---	9.62E-02	---
Inferior Longitudinal Fasciculus Left	1.137E-03	1.125E-03	1.167E-03	2.31E-01	---	8.98E-03	Reject	9.47E-04	Reject
Inferior Longitudinal Fasciculus Right	1.136E-03	1.130E-03	1.150E-03	5.64E-01	---	1.77E-01	---	8.22E-02	---
Optic Radiation Left	1.098E-03	1.093E-03	1.148E-03	5.93E-01	---	9.96E-07	Reject	4.82E-06	Reject
Optic Radiation Right	1.095E-03	1.089E-03	1.136E-03	4.96E-01	---	1.55E-06	Reject	1.41E-05	Reject
Superior Longitudinal Fasciculus Left	1.089E-03	1.086E-03	1.097E-03	6.10E-01	---	2.74E-01	---	1.49E-01	---
Superior Longitudinal Fasciculus Right	1.104E-03	1.099E-03	1.097E-03	5.09E-01	---	3.37E-01	---	8.32E-01	---
Uncinate Fasciculus Left*	1.206E-03	1.183E-03	1.192E-03	---	---	---	---	---	---
Uncinate Fasciculus Right*	1.230E-03	1.215E-03	1.214E-03	---	---	---	---	---	---
TOTAL					2		8		8

Table 5.23: RD T-Test scores: comparing male, female and control groups

ROI	Female	Male	Control Group	Female vs Male		Female vs Control		Male vs Control	
				T-Test (P-value)	Reject H$_0$ (if p<0.05)	T-Test (P-value)	Reject H0 (if p<0.05)	T-Test (P-value)	Reject H0 (if p<0.05)
Acoustic Radiation Left	8.188E-04	8.169E-04	7.684E-04	8.99E-01	---	2.25E-04	Reject	8.97E-04	Reject
Acoustic Radiation Right*	8.577E-04	8.466E-04	8.000E-04	---	---	---	---	---	---
Cingulate Gyrus Left	6.770E-04	6.942E-04	6.469E-04	2.14E-01	---	2.66E-03	Reject	1.13E-03	Reject
Cingulate Gyrus Right	6.955E-04	7.408E-04	6.763E-04	2.11E-03	Reject	8.05E-02	---	1.56E-05	Reject
Cingulum Left	6.710E-04	6.990E-04	6.743E-04	1.80E-02	Reject	7.23E-01	---	2.62E-02	Reject
Cingulum Right	6.514E-04	6.976E-04	6.589E-04	4.05E-04	Reject	4.83E-01	---	8.12E-04	Reject
Corpus Callosum*	7.528E-04	8.118E-04	7.828E-04	---	---	---	---	---	---
Corticospinal Tract Left	7.197E-04	7.552E-04	6.523E-04	6.42E-02	---	3.65E-04	Reject	8.21E-08	Reject
Corticospinal Tract Right	7.316E-04	7.384E-04	6.517E-04	7.83E-01	---	1.88E-04	Reject	2.43E-04	Reject
Forceps Major	6.822E-04	7.265E-04	7.288E-04	1.12E-01	---	2.50E-02	Reject	9.25E-01	---
Forceps Minor	7.075E-04	7.483E-04	6.903E-04	4.52E-04	Reject	2.86E-02	Reject	4.77E-06	Reject
Fornix	1.116E-03	1.195E-03	1.093E-03	2.45E-01	---	5.68E-01	---	1.34E-01	---
Hippocampus Left	7.455E-04	7.710E-04	7.602E-04	9.62E-02	---	3.06E-01	---	4.25E-01	---
Hippocampus Right	7.776E-04	8.186E-04	7.596E-04	4.51E-02	Reject	1.98E-01	---	4.51E-03	Reject
Inferior Fronto-occipital Fasciculus Left	6.426E-04	6.639E-04	6.526E-04	7.11E-03	Reject	1.14E-01	---	1.44E-01	---
Inferior Fronto-occipital Fasciculus Right	6.599E-04	6.660E-04	6.555E-04	4.80E-01	---	5.52E-01	---	3.12E-01	---
Inferior Longitudinal Fasciculus Left	6.635E-04	6.829E-04	6.884E-04	4.35E-02	Reject	4.98E-04	Reject	5.65E-01	---
Inferior Longitudinal Fasciculus Right	6.565E-04	6.584E-04	6.722E-04	7.88E-01	---	2.07E-02	Reject	1.21E-01	---
Optic Radiation Left	6.868E-04	7.044E-04	7.276E-04	1.52E-02	Reject	2.33E-08	Reject	2.25E-03	Reject
Optic Radiation Right	6.801E-04	6.953E-04	7.088E-04	3.92E-02	Reject	8.88E-06	Reject	8.57E-02	---
Superior Longitudinal Fasciculus Left	6.775E-04	6.867E-04	6.779E-04	2.24E-01	---	9.48E-01	---	2.28E-01	---
Superior Longitudinal Fasciculus Right	6.794E-04	6.976E-04	6.624E-04	1.81E-02	Reject	8.89E-03	Reject	4.20E-05	Reject
Uncinate Fasciculus Left	7.433E-04	7.445E-04	6.782E-04	9.39E-01	---	1.81E-05	Reject	1.13E-05	Reject
Uncinate Fasciculus Right	7.902E-04	7.690E-04	7.146E-04	8.48E-02	---	5.85E-07	Reject	1.11E-06	Reject
TOTAL					10		13		13

5.3   Correlating DTI Findings with QSM

Lastly, a preliminary test was undertaken to see if susceptibility, as measured by QSM, could provide another viable indicator of mTBI. Pearson's product moment correlation method was used to investigate whether a linear correlation existed between susceptibility and each DTI metric individually (FA, AD and RD). The significance (p) of each measured r coefficient was also calculated. This analysis was performed for all 24 processed ROIs and the results for susceptibility relative to FA, AD and RD are presented in Tables 5.24, 5.25 and 5.26, respectively.

Significant moderately positive correlations were observed under only two specific parameters; susceptibility relative to AD in the superior longitudinal fasciculus and susceptibility relative to RD in the forceps minor. Figures 5.1 and 5.2 provide a graphical representation of the relationship between these metrics. Further, QSM derived magnetic susceptibility measurements were found to be weakly correlated to FA in ten regions, AD in seven regions and RD in five regions. However, none of these correlations were considered significant since $p > 0.05$. In general, this preliminary data suggests that there may not be a significant correlation between QSM and DTI measurements.

Table 5.24: FA vs Susceptibility: Pearson Correlation Coefficient scores

ROI	R coefficient	p-value
Acoustic Radiation Left	-0.1121	0.5345
Acoustic Radiation Right	0.2163	0.2268
Cingulate Gyrus Left	-0.2592	0.1452
Cingulate Gyrus Right	-0.1277	0.4788
Cingulum Left	-0.2695	0.1294
Cingulum Right	-0.2879	0.1043
Corpus Callosum	-0.0815	0.6523
Corticospinal Tract Left	-0.2625	0.1400
Corticospinal Tract Right	-0.0088	0.9614
Forceps Major	-0.1093	0.5447
Forceps Minor	-0.2364	0.1854
Fornix	0.3387	0.0538
Hippocampus Left	0.2614	0.1417
Hippocampus Right	-0.0360	0.8423
Inferior Fronto-occipital Fasciculus Left	0.0261	0.8854
Inferior Fronto-occipital Fasciculus Right	-0.2546	0.1528
Inferior Longitudinal Fasciculus Left	-0.0626	0.7293
Inferior Longitudinal Fasciculus Right	-0.0025	0.9890
Optic Radiation Left	-0.0412	0.8197
Optic Radiation Right	0.0216	0.9049
Superior Longitudinal Fasciculus Left	-0.1820	0.3108
Superior Longitudinal Fasciculus Right	0.1160	0.5205
Uncinate Fasciculus Left	0.2598	0.1443
Uncinate Fasciculus Right	-0.0419	0.8170

† denotes that the correlation coefficient r is significant for that particular ROI

Table 5.25: AD vs Susceptibility: Pearson Correlation Coefficient scores

ROI	R coefficient	p-value
Acoustic Radiation Left	0.0418	0.8174
Acoustic Radiation Right	0.0751	0.6779
Cingulate Gyrus Left	-0.0958	0.5961
Cingulate Gyrus Right	0.0961	0.5948
Cingulum Left	-0.2547	0.1526
Cingulum Right	-0.2260	0.2060
Corpus Callosum	-0.2981	0.0920
Corticospinal Tract Left	-0.1559	0.3864
Corticospinal Tract Right	0.2408	0.1770
Forceps Major	-0.1432	0.4267
Forceps Minor	0.1025	0.5705
Fornix	-0.2155	0.2285
Hippocampus Left	-0.0472	0.7943
Hippocampus Right	-0.0488	0.7874
Inferior Fronto-occipital Fasciculus Left	0.1432	0.4265
Inferior Fronto-occipital Fasciculus Right	0.0063	0.9721
Inferior Longitudinal Fasciculus Left	-0.0022	0.9904
Inferior Longitudinal Fasciculus Right	0.0569	0.7533
Optic Radiation Left	-0.0271	0.8811
Optic Radiation Right	-0.1898	0.2902
Superior Longitudinal Fasciculus Left	0.0906	0.6160
Superior Longitudinal Fasciculus Right	0.4617	0.0068 [†]
Uncinate Fasciculus Left	0.0038	0.9831
Uncinate Fasciculus Right	-0.2125	0.2351

[†] denotes that the correlation coefficient r is significant for that particular ROI

Table 5.26: RD vs Susceptibility: Pearson Correlation Coefficient scores

ROI	R coefficient	p-value
Acoustic Radiation Left	0.1408	0.4346
Acoustic Radiation Right	0.0036	0.9840
Cingulate Gyrus Left	0.1932	0.2814
Cingulate Gyrus Right	-0.0241	0.8941
Cingulum Left	0.1726	0.3367
Cingulum Right	-0.0054	0.9764
Corpus Callosum	-0.2244	0.2093
Corticospinal Tract Left	0.0222	0.9025
Corticospinal Tract Right	0.0364	0.8404
Forceps Major	-0.1353	0.4529
Forceps Minor	0.4508	0.0085 †
Fornix	-0.2597	0.1444
Hippocampus Left	-0.1108	0.5395
Hippocampus Right	0.0762	0.6733
Inferior Fronto-occipital Fasciculus Left	-0.0077	0.9661
Inferior Fronto-occipital Fasciculus Right	0.2423	0.1744
Inferior Longitudinal Fasciculus Left	0.0535	0.7675
Inferior Longitudinal Fasciculus Right	-0.2560	0.1505
Optic Radiation Left	-0.0216	0.9050
Optic Radiation Right	-0.1631	0.3645
Superior Longitudinal Fasciculus Left	0.1458	0.4183
Superior Longitudinal Fasciculus Right	0.0341	0.8507
Uncinate Fasciculus Left	-0.0969	0.5915
Uncinate Fasciculus Right	-0.0482	0.7900

† denotes that the correlation coefficient r is significant for that particular ROI
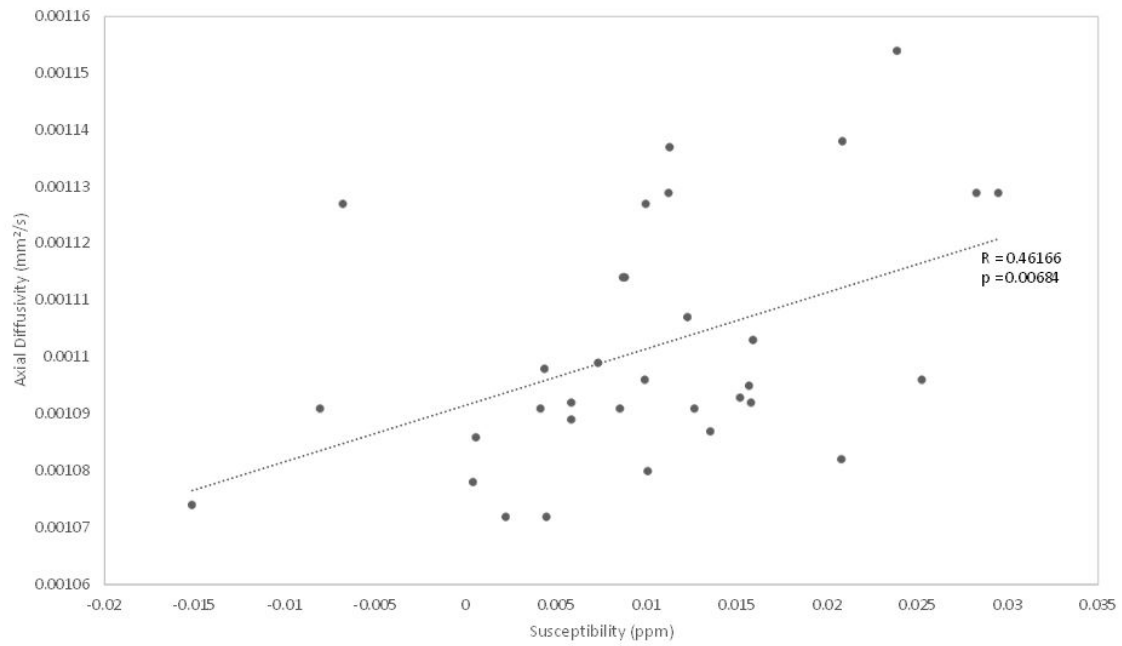
Figure 5.1: AD vs Susceptibility within the right Superior Longitudinal Fasciculus
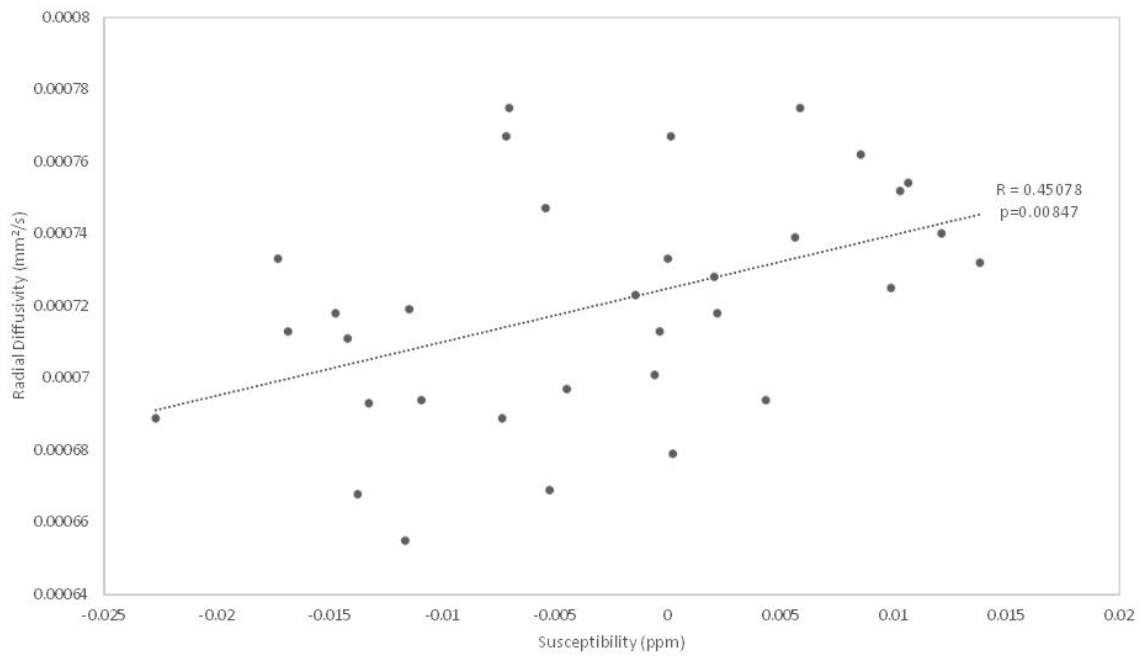

Figure 5.2: RD vs Susceptibility within the Forceps Minor

89

Chapter 6

Conclusions and Future Work

6.1 Summary of Major Findings

Paediatric patients who had recently been diagnosed with a mTBI were recruited for the purposes of this study. DTI and SWI data was acquired from this group and compared relative to a large age-matched control population in order to investigate the microstructural changes resulting from mTBI. Patients were also examined longitudinally over time to monitor their recovery and observe any microstructural changes on an individual basis.

6.1.1 Diagnosis of mTBI

Based on results from the case-based Z-scoring, DTI metrics measured in specific ROIs appeared to provide viable biomarkers for diagnosis of mTBI in a given individual. Using FA measurements, we were able to identify significant abnormalities in the inferior and superior longitudinal fasciculus as well as the inferior fronto-occipital

fasciculus. These regions are all involved in auditory, visual, and memory integration. Any impairment may result in a decreased ability to comprehend and remember new information; both written and spoken. The uncinate fasciculus was found to be abnormal for a number of patients in terms of RD and the corticospinal tract was greatly impacted in terms of both RD and AD. The uncinate fasciculus' primary function is memory integration and the corticospinal tract is involved in motor control processes by conducting brain impulses to the spinal cord.

These outcomes were supported by group-based analysis which verified that the mTBI group was significantly different from the control population in each of the identified regions. Further, certain ROIs were found to be effective at identifying abnormalities regardless of the DTI metric, where as others were most useful when focusing on a single metric. A select few ROIs were virtually ineffective regardless of the metric - interestingly these ROIs tended to be part of deeper brain structures. When considering the efficacy of all three DTI metrics, the corticospinal tract was determined to be the region most significantly impacted by mTBI.

6.1.2   Prognosis of mTBI

The results of the longitudinal study showed minimal variation between the initial and follow up scans for each patient. The majority of microstructural abnormalities observed in the initial scans remained abnormal even after the patient's symptoms had resolved. This was further supported by group-based analysis comparing the data from the symptomatic and symptom-free groups (only one ROI was significantly different in terms of RD; none were significantly different for FA or AD). Overall, this data suggests that even though FA, AD and RD measurements appear to be helpful

when diagnosing mTBI, they were mostly ineffectual at identifying an individual's stage of recovery. At least that was the case over the six-month duration these participants participated in the study. Perhaps differences would be observed if the follow up scan was scheduled on a later date, increasing total recovery time. What can be surmised from this experiment was that, in most cases, the abnormalities identified did not resolve themselves over this six-month monitoring window. We can hypothesize that the brain was able to adapt to these microstructural abnormalities over the course of recovery. It is possible that these microstructural changes are in fact permanent but there also exists the possibility that they may eventually resolve if given adequate time to recover.

6.1.3   Patient Demographic Factors

Though there were several differences identified between the mTBI and control groups as a whole, it was found that age and gender also factored into the differences observed within certain regions. A great number of abnormalities were found in the male participants and the younger age group. Additionally, abnormalities were more commonly identified in deeper brain regions for the younger age group. This suggests that younger individuals may be more sensitive to mTBI resulting in more significant microstructural irregularities within deeper brain tissue.

6.1.4   Correlating DTI to QSM

Preliminary analysis using Pearson's product-moment correlation method yielded only two instances where a significant linear correlation was observed between a DTI metric and susceptibility measurement. With the exceptions of AD in the superior

longitudinal fasciculus and RD in the forceps minor, susceptibility did not appear to have a strong correlation with any of the DTI metrics or within any particular ROI. Even when ignoring the significance level and focusing on the correlation coefficients, no pattern emerged for FA, AD or RD relative to susceptibility. Overall this evidence suggests that no correlation exists between DTI and QSM measurements. This, however, does not mean that susceptibility cannot be used for analysis of mTBI. Further studies should still be undertaken to investigate differences between healthy and concussed individuals as measured by QSM.

6.2   Areas of Improvement and Future Research

There are a few areas within this study which could be improved upon for future work. Notably, more comprehensive information pertaining to each mTBI patient would be useful for further analysis and for identifying potential trends in the data. This study compared the mTBI subjects relative to an age-matched control population (which was also tested for normality). However, it would be even more useful if base-line data was also collected. This would allow us to quantify, with relative certainty, each individual's brain microstructure prior to injury. Realistically it would be difficult to recruit healthy paediatric subjects to undergo baseline MRI examinations and then, essentially be on-call for if they suffer a mTBI. Perhaps a viable alternative would be to perform baseline scans for players from a high-impact sports team or league (such as football or hockey) and then monitor them over the course of a season. If any player sustained a concussion, another MRI exam could be performed and this data could be referenced to that player's baseline data to identify which regions were affected. Further, acquiring more detailed information at the time of recruitment would also

be useful. Specifically, it would be invaluable to identify the mode of injury including the location of the concussive impact. Identifying which area of the head was hit (or if the head wasn't the primary point of contact at all and a whiplash effect caused the injury) may be crucial information to help account for the variability seen between patients in terms of the location and frequency of abnormalities.

As previously stated, longitudinal analyses proved ineffective at predicting recovery rates on a per patient basis. On a microstructural level, it would appear that the brain does not necessarily have to resolve the abnormalities before the patient can fully recover. Rather, the brain seemed to find ways to compensate by creating new neural pathways and connections to adapt to the abnormalities in microstructure. It would be very useful if patients returned for one final follow up scan 12 months post-symptom resolution date to see if the brain microstrucuture has remained constant or if the abnormalities have resolved. The outcomes of this work may provide insight into which people are more likely to develop post-concussive symptoms in the future or are at greater risk of re-injury. Further long-term longitudinal studies would be very useful in order to answer questions such as;

- Do abnormalities resulting from mTBI eventually resolve and revert back to its pre-mTBI state or is the microstructure forever altered?

- Assuming abnormalities resolve themselves in only some patients but not in every case, is one group more susceptible to future injuries or more likely to develop long-term post-concussive symptoms in the future?

Another way to approach the second question would be; in terms of long-term health, is it advantageous for the brain to adapt to the new microstructure or is it preferable

that the abnormalities eventually resolve over time? Though these questions are yet to be answered, longitudinal studies monitoring individual patient recovery over long time frames (in excess of 12 months) would help shed light on these issues. Improved understanding of the deeper mechanics of mTBI would also further aid in identifying which regions of the brain provide the best biomarkers of injury and can help predict both severity and duration of symptoms on an individualized basis.

Appendix A

Diffusion Tensor Gradient

Table A.1 shows the concatenated 60-direction tensor file. This tensor is preceded by $12 < 0, 0, 0 >$ vectors representing the b0 volumes. Table A.2 shows the initial twelve b-values, this is followed by 60 b=1000 rows.

Table A.1: 60 direction b-vector tensor: lines 13 through 72

60-dir Tensor

	-1	0	0
	-0.439	0.898	0
	0.291	0.468	0.834
	-0.848	-0.53	0.028
	0.178	-0.869	0.462
	0.557	-0.291	0.778
	-0.827	0.506	0.246
	0.207	0.978	-0.003
	-0.844	-0.037	0.535
direction 10	-0.501	-0.758	0.418
	-0.019	-0.863	-0.505
	0.386	-0.183	-0.904
	0.042	-0.532	0.846
	0.581	0.708	0.401
	0.481	0.375	-0.793
	0.796	-0.504	0.336
	-0.816	-0.156	-0.556
	-0.08	-0.046	-0.996
	0.447	-0.643	-0.621
direction 20	-1	0	0

	-0.336	0.942	0
	0.405	0.606	0.685
	-0.825	-0.513	-0.236
	-0.006	-0.363	0.932
	0.811	-0.287	0.51
	-0.852	-0.32	0.414
	0.24	0.959	0.149
	-0.835	0.272	0.478
	-0.009	-0.904	0.427
direction 30	0.063	-0.812	-0.58
	0.269	-0.39	-0.881
	0.422	-0.624	0.658
	0.601	0.779	-0.177
	0.516	0.086	-0.852
	0.79	-0.607	0.087
	-0.729	-0.181	-0.661
	-0.265	-0.096	-0.96
	0.561	-0.701	-0.44
	0.405	0.631	-0.662
direction 40	-1	0	0
	-0.528	0.849	0
	0.222	0.613	0.759
	-0.811	-0.58	0.079
	0.094	-0.86	0.501
	0.817	-0.181	0.548
	-0.77	0.312	0.557
	-0.024	0.997	0.067
	-0.804	-0.258	0.535
	-0.429	-0.86	0.277
direction 50	-0.417	-0.852	-0.317
	0.317	-0.381	-0.869
	0.277	-0.433	0.858
	0.812	0.414	0.412
	0.398	0.115	-0.91
	0.6	-0.644	0.475
	-0.559	-0.218	-0.8
	-0.132	-0.048	-0.99
	0.308	-0.807	-0.504
	0.317	0.589	-0.743
direction 60	-0.876	0.478	0.062

Table A.2: 60 direction b-value matrix: lines 1 through 12

	B-values
	0
	0
	1000
	1000
line 5	0
	0
	1000
	1000
	0
line 10	0
	1000
	1000

Appendix B

DTI Processing Pipeline

This project involved a significant amount of Bourne-again shell (BASH) programming in order to facilitate data reconstruction and post-processing. Below is an outline of all the major steps used in order to generate FA, AD, and RD volumes from the raw 19-, 20-, and 21-direction DTI files:

1. Merge the 19-, 20-, and 21-dir.nii files into a single file named "dti60.nii"

   a) split each file into their 72 individual volumes including b0 volumes using the command:

      - fslsplit dti19 v19- t

   b) merge these 72 volumes into a single file (with all b0 volumes at the beginning) using the command:

      - fslmerge t dti60.nii v19-0000 v19-0001 v19-0012 v19-0022 v20-0000 v20-0001 v20-0012 v20-0023 v21-0000 v21-0001 v21-0012 v21-0024 v19-0002 v19-0003 v19-0004 v19-0005 v19-0006 v19-0007 v19-0008 v19-0009 v19-0010 v19-0011 v19-0013 v19-0014 v19-0015 v19-0016 v19-0017 v19-0018

v19-0019 v19-0020 v19-0021 v20-0002 v20-0003 v20-0004 v20-0005 v20-0006 v20-0007 v20-0008 v20-0009 v20-0010 v20-0011 v20-0013 v20-0014 v20-0015 v20-0016 v20-0017 v20-0018 v20-0019 v20-0020 v20-0021 v20-0022 v21-0002 v21-0003 v21-0004 v21-0005 v21-0006 v21-0007 v21-0008 v21-0009 v21-0010 v21-0011 v21-0013 v21-0014 v21-0015 v21-0016 v21-0017 v21-0018 v21-0019 v21-0020 v21-0021 v21-0022 v21-0023

c) Confirm that they are in correct order in FSLview (CSF will be bright in b0 images)

2. Eddy Current correction in FSL FDTDiffusion (takes approximately 30 minutes) outputs the file "dti60-ecc.nii"

3. Brain extraction of the dti60-ecc.nii file using FSL BET (std brain extraction using bet2). Set threshold =0.3 to err on side of caution. Under advanced options, select "binary brain mask" and deselect "extracted brain"

4. Reconstruct diffusion tensor using FSL FDT. Specify input files manually:

a) DW Data = dti-ecc.nii

b) Brain mask = dti60-ecc-brain

c) output basename = (default)

d) Gradient = dti60.bvec

e) b Values = dti60.bval

Appendix C

ROI Generation Shell Script

ROI processing for both DTI and QSM data was accomplished, largely, through BASH scripting. The following script was used to multiply the 24 ROI binary masks over the 34 FA, RD, AD and 33 QSM volumes for each mTBI participant as well as the 49 FA, RD, AD volumes for the control subjects.

```
#!/bin/bash

-------------------------------------------------------------------------------------
#NOTES: This script multiplies every FA, L1, and RD image to each brain mask for
given ROIs.
        #remember to type in command line... chmod 700 "script name"
        #Type ./"script name" to run

#UPDATE 3: includes both L & R portions of each ROI

#DTI Inputs: FA, L1, RD files for control files and tbi files saved in separate folders
(naming convention: fa$i, l$i, rd$i; i=1-49 for ctrl; i=1-35 for tbi)

#QSM Inputs: files named qsm$i; i=1-33

#Mask inputs: naming convention is mask-"roi"; where "roi"= [cigyL, cigyR, cingL,
cingR, ... slfaL, slfaR]
-------------------------------------------------------------------------------------
echo "CONTROL FA"

for i in {1..49}
do
        fslmaths mask-cigyL -mul fa$i cigyL-fa$i
        fslmaths mask-cigyR -mul fa$i cigyR-fa$i
        fslmaths mask-cingL -mul fa$i cingL-fa$i
        fslmaths mask-cingR -mul fa$i cingR-fa$i
        fslmaths mask-corspL -mul fa$i corspL-fa$i
        fslmaths mask-corspR -mul fa$i corspR-fa$i

        fslmaths mask-hipL -mul fa$i hipL-fa$i
        fslmaths mask-hipR -mul fa$i hipR-fa$i
        fslmaths mask-formaj -mul fa$i formaj-fa$i
        fslmaths mask-formin -mul fa$i formin-fa$i
        fslmaths mask-forn -mul fa$i forn-fa$i
        fslmaths mask-ilfaL -mul fa$i ilfaL-fa$i

        fslmaths mask-ilfaR -mul fa$i ilfaR-fa$i
        fslmaths mask-unfaL -mul fa$i unfaL-fa$i
        fslmaths mask-unfaR -mul fa$i unfaR-fa$i
        fslmaths mask-acradL -mul fa$i acradL-fa$i
        fslmaths mask-acradR -mul fa$i acradR-fa$i
        fslmaths mask-cc -mul fa$i cc-fa$i

        fslmaths mask-ifofaL -mul fa$i ifoFaL-fa$i
```

```
        fslmaths mask-ifofaR -mul fa$i ifoFaR-fa$i
        fslmaths mask-opradL -mul fa$i opRadL-fa$i
        fslmaths mask-opradR -mul fa$i opRadR-fa$i
        fslmaths mask-slfaL -mul fa$i slFaL-fa$i
        fslmaths mask-slfaR -mul fa$i slFaR-fa$i

done

echo "CONTROL L1"

for i in {1..49}
do
        fslmaths mask-cigyL -mul l$i cigyL-l$i
        fslmaths mask-cigyR -mul l$i cigyR-l$i
        fslmaths mask-cingL -mul l$i cingL-l$i
        fslmaths mask-cingR -mul l$i cingR-l$i
        fslmaths mask-corspL -mul l$i corspL-l$i
        fslmaths mask-corspR -mul l$i corspR-l$i


        fslmaths mask-hipL -mul l$i hipL-l$i
        fslmaths mask-hipR -mul l$i hipR-l$i
        fslmaths mask-formaj -mul l$i formaj-l$i
        fslmaths mask-formin -mul l$i formin-l$i
        fslmaths mask-forn -mul l$i forn-l$i
        fslmaths mask-ilfaL -mul l$i ilfaL-l$i

        fslmaths mask-ilfaR -mul l$i ilfaR-l$i
        fslmaths mask-unfaL -mul l$i unfaL-l$i
        fslmaths mask-unfaR -mul l$i unfaR-l$i
        fslmaths mask-acradL -mul l$i acradL-l$i
        fslmaths mask-acradR -mul l$i acradR-l$i
        fslmaths mask-cc -mul l$i cc-l$i

        fslmaths mask-ifofaL -mul l$i ifoFaL-l$i
        fslmaths mask-ifofaR -mul l$i ifoFaR-l$i
        fslmaths mask-opradL -mul l$i opRadL-l$i
        fslmaths mask-opradR -mul l$i opRadR-l$i
        fslmaths mask-slfaL -mul l$i slFaL-l$i
        fslmaths mask-slfaR -mul l$i slFaR-l$i

done

echo "CONTROL RD"

for i in {1..49}
do
```

```
        fslmaths mask-cigyL -mul rd$i cigyL-rd$i
        fslmaths mask-cigyR -mul rd$i cigyR-rd$i
        fslmaths mask-cingL -mul rd$i cingL-rd$i
        fslmaths mask-cingR -mul rd$i cingR-rd$i
        fslmaths mask-corspL -mul rd$i corspL-rd$i
        fslmaths mask-corspR -mul rd$i corspR-rd$i

        fslmaths mask-hipL -mul rd$i hipL-rd$i
        fslmaths mask-hipR -mul rd$i hipR-rd$i
        fslmaths mask-formaj -mul rd$i formaj-rd$i
        fslmaths mask-formin -mul rd$i formin-rd$i
        fslmaths mask-forn -mul rd$i forn-rd$i
        fslmaths mask-ilfaL -mul rd$i ilfaL-rd$i

        fslmaths mask-ilfaR -mul rd$i ilfaR-rd$i
        fslmaths mask-unfaL -mul rd$i unfaL-rd$i
        fslmaths mask-unfaR -mul rd$i unfaR-rd$i
        fslmaths mask-acradL -mul rd$i acradL-rd$i
        fslmaths mask-acradR -mul rd$i acradR-rd$i
        fslmaths mask-cc -mul rd$i cc-rd$i

        fslmaths mask-ifofaL -mul rd$i ifoFaL-rd$i
        fslmaths mask-ifofaR -mul rd$i ifoFaR-rd$i
        fslmaths mask-opradL -mul rd$i opRadL-rd$i
        fslmaths mask-opradR -mul rd$i opRadR-rd$i
        fslmaths mask-slfaL -mul rd$i slFaL-rd$i
        fslmaths mask-slfaR -mul rd$i slFaR-rd$i

done

echo "QSM masking"

for i in {1..33}
do
        fslmaths mask-cigyL -mul qsm$i cigyL-qsm$i
        fslmaths mask-cigyR -mul qsm$i cigyR-qsm$i
        fslmaths mask-cingL -mul qsm$i cingL-qsm$i
        fslmaths mask-cingR -mul qsm$i cingR-qsm$i
        fslmaths mask-corspL -mul qsm$i corspL-qsm$i
        fslmaths mask-corspR -mul qsm$i corspR-qsm$i

        fslmaths mask-hipL -mul qsm$i hipL-qsm$i
        fslmaths mask-hipR -mul qsm$i hipR-qsm$i
        fslmaths mask-formaj -mul qsm$i formaj-qsm$i
        fslmaths mask-formin -mul qsm$i formin-qsm$i
        fslmaths mask-forn -mul qsm$i forn-qsm$i
```

```
fslmaths mask-ilfaL -mul qsm$i ilfaL-qsm$i

fslmaths mask-ilfaR -mul qsm$i ilfaR-qsm$i
fslmaths mask-unfaL -mul qsm$i unfaL-qsm$i
fslmaths mask-unfaR -mul qsm$i unfaR-qsm$i
fslmaths mask-acradL -mul qsm$i acradL-qsm$i
fslmaths mask-acradR -mul qsm$i acradR-qsm$i
fslmaths mask-cc -mul qsm$i cc-qsm$i

fslmaths mask-ifofaL -mul qsm$i ifoFaL-qsm$i
fslmaths mask-ifofaR -mul qsm$i ifoFaR-qsm$i
fslmaths mask-opradL -mul qsm$i opRadL-qsm$i
fslmaths mask-opradR -mul qsm$i opRadR-qsm$i
fslmaths mask-slfaL -mul qsm$i slFaL-qsm$i
fslmaths mask-slfaR -mul qsm$i slFaR-qsm$i

done
```

Appendix D

ROI Statistics Shell Script

In order to obtain the DTI and QSM data for each ROI, further BASH scripting was required. The following script calculates the mean (for all non-zero voxels) of the processed FA volumes one ROI at a time. This code can also work for the rest of the data by replacing <fa> within the code with <rd; ad; qsm>.

```
#!/bin/bash

-----------------------------------------------------------------------------------------------------
# Control FA, RD, L1 Stats

#NOTES: This script computes the mean value of every image in each ROI series
        #remember to type in command line... chmod 700 "script name"
        #Type ./"script name" to run

#INPUTS: every tbi group <roi> - <dti> and every <roi - qsm> volume (35 subjects *
3 metrics * 24 regions for dti files, 33 subjects *24 regions for qsm files)

#INPUTS: switch folder to control data and input every <roi> - <dti> file (49
subjects * 3 metrics * 24 regions)
-----------------------------------------------------------------------------------------------------
```

```
echo "Control Group:"

                    echo "**********FRACTIONAL ANISTROPY**********"

echo "CINGULATE GYRUS L"
for i in {1..49}
do
        fslstats cigyL-fa$i -M
done

echo "CINGULATE GYRUS R"
for i in {1..49}
do
        fslstats cigyR-fa$i -M
done

echo "CINGULUM L"
for i in {1..49}
do
        fslstats cingL-fa$i -M
done

echo "CINGULUM R"
for i in {1..49}
do
        fslstats cingR-fa$i -M
done

echo "CORTICOSPINAL TRACT L"
for i in {1..49}
do
        fslstats corspL-fa$i -M
done

echo "CORTICOSPINAL TRACT R"
for i in {1..49}
do
        fslstats corspR-fa$i -M
done

echo "FORCEPS MAJOR"
for i in {1..49}
do
        fslstats formaj-fa$i -M
done
```

```
echo "FORCEPS MINOR"
for i in {1..49}
do
        fslstats formin-fa$i -M
done

echo "FORNIX"
for i in {1..49}
do
        fslstats forn-fa$i -M
done

echo "HIPPOCAMPUS L"
for i in {1..49}
do
        fslstats hipL-fa$i -M
done

echo "HIPPOCAMPUS R"
for i in {1..49}
do
        fslstats hipR-fa$i -M
done

echo "INFERIOR LONGITUDINAL FASCICULUS L"
for i in {1..49}
do
        fslstats ilfaL-fa$i -M
done

echo "INFERIOR LONGITUDINAL FASCICULUS R"
for i in {1..49}
do
        fslstats ilfaR-fa$i -M
done

echo "UNCINATE FASCICULUS L"
for i in {1..49}
do
        fslstats unfaL-fa$i -M
done

echo "UNCINATE FASCICULUS R"
for i in {1..49}
do
        fslstats unfaR-fa$i -M
```

```
done

echo "ACOUSTIC RADIATION L"
for i in {1..49}
do
      fslstats acradL-fa$i -M
done

echo "ACOUSTIC RADIATION R"
for i in {1..49}
do
      fslstats acradR-fa$i -M
done

echo "CORPUS CALLOSUM"
for i in {1..49}
do
      fslstats cc-fa$i -M
done

echo "INFERIOR FRONTO-OCCIPITAL FASCICULUS L"
for i in {1..49}
do
      fslstats ifoFaL-fa$i -M
done

echo "INFERIOR FRONTO-OCCIPITAL FASCICULUS R"
for i in {1..49}
do
      fslstats ifoFaR-fa$i -M
done

echo "OPTIC RADIATION L"
for i in {1..49}
do
      fslstats opradL-fa$i -M
done

echo "OPTIC RADIATION R"
for i in {1..49}
do
      fslstats opradR-fa$i -M
done

echo "SUPERIOR LONGITUDINAL FASCICULUS L"
for i in {1..49}
```

```
do
        fslstats slFaL-fa$i -M
done

echo "SUPERIOR LONGITUDINAL FASCICULUS R"
for i in {1..49}
do
        fslstats slFaR-fa$i -M
done
```

Appendix E

Publisher Permissions

Figure 3.2, 3.4 and 4.12 were obtained via external sources and are included, with permission, in this thesis. The following documentation was received from the copyright owner of Figure 4.12 and permits it to be incorporated in this thesis. In addition, permission was also granted by the respective authors to use Figures 3.2 and 3.4. These permissions were sent via email exchange and are not included in this section.

Figure E.1: Permission to use Figure 4.12

Bibliography

Akiyama, Y. (2009). Susceptibility-weighted magnetic resonance imaging for the detection of cerebral microhemorrhage in patients with traumatic brain injury. *Neurologia Medico-Chirurgica*, **49**, 97–99.

Andersson, J. and Sotiropoulos, S. (2016). An integrated approach to correction for off-resonance effects and subject movement in diffusion MR imaging. *Neuroimage*, **125**, 1063–1078.

Area Education Agency 267 (2012). Z scores and t scores. `https://www.aea267.k12.ia.us/assessment/different-types-of-data-and-scores/z-scores-and-t-scores/`. [Online; accessed 2016-07-05].

Arfanakis, K. (2002). Diffusion tensor MR imaging in diffuse axonal injury. *American Journal of Neuroradiology*, **23**, 794–802.

Basser, P., Mattiello, J., and Lebihan, D. (1994a). Estimation of the effective self-diffusion tensor from the NMR spin echo. *Journal of Magnetic Resonance*, **103**, 247–254.

Basser, P., Mattiello, J., and Lebihan, D. (1994b). The basis of anisotropic water

diffusion in the nervous system a technical review. *Biophysics Journal*, **66**, 259–267.

Bazarian, J., Blyth, B., and Cimpello, L. (2006). Bench to bedside: evidence for brain injury after concussionlooking beyond the computed tomography scan. *Academic Emergency Medicine*, **13**, 199–214.

Beaulieu, C. (2002). The basis of anisotropic water diffusion in the nervous system a technical review. *NMR in Biomedicine*, **15**, 435–455.

Behrens, T., Woolrich, M., Jenkinson, M., Johansen-Berg, H., Nunes, R., Clare, S., Matthews, P., Brady, J., and Smith, S. (2003). Characterization and propagation of uncertainty in diffusion-weighted MR imaging. *Magnetic Resonance in Medicine*, **50**, 1077–1088.

Behrens, T., Johansen-Berg, H., Jbabdi, S., Rushworth, M., and Woolrich, M. (2007). Probabilistic diffusion tractography with multiple fibre orientations. What can we gain? *Neuroimage*, **23**, 144–155.

Bernstein, M., King, K., and Zhou, X. (2004). *Handbook of MRI Pulse Sequences.* Elsevier, Inc., Amsterdam.

Binder, L., Rohling, M., and Larrabee, J. (1997a). A review of mild head trauma. Part I: Meta-analytic review of neuropsychological studies. *Journal of Clinical and Experimental Neuropsychology*, **19**, 421–431.

Binder, L., Rohling, M., and Larrabee, J. (1997b). A review of mild head trauma. Part II: Clinical implications. *Journal of Clinical and Experimental Neuropsychology*, **19**, 432–457.

Caeyenberghs, K., Leemans, A., Geurts, M., and Linden, C. (2011a). Bimanual coordination and corpus callosum microstructure in young adults with traumatic brain injury: a diffusion tensor imaging study. *Journal of Neurotrauma*, **28**, 897–913.

Caeyenberghs, K., Leemans, A., Geurts, M., and Linden, C. (2011b). Correlations between white matter integrity and motor function in traumatic brain injury patients. *Neurorehabilitation and Neural Repair*, **25**, 492–502.

Cantu, R. (1998). Second-Impact Syndrome. *Clinics in Sports Medicine*, **17**, 37–44.

Cubon, V. (2011). A diffusion tensor imaging study on the white matter skeleton in individuals with sports-related concussion. *Journal of Neurotrauma*, **28**, 189–201.

Dennis, E. (2015). White matter disruption in moderate/severe pediatric traumatic brain injury: advanced tract-based analyses. *Neuroimage: Clinical*, **7**, 493–505.

Doshi, H., Wiseman, N., Liu, J., Wang, W., Welch, R., O'Neil, B., Zuk, C., and Wang, X. (2015). Cerebral Hemodynamic Changes of Mild Traumatic Brain Injury at the Acute Stage. *PloS One*, **10**, 1–18.

Eickhoff, S., Stephan, K., and Mohlberg, H. (2005). A new SPM toolbox for combining probabilistic cytoarchitectonic maps and functional imaging data. *Neuroimage*, **25**, 1325–35.

Eickhoff, S., Heim, S., and Zilles, K. (2006). Testing anatomically specified hypotheses in functional imaging using cytoarchitectonic maps. *Neuroimage*, **32**, 570–582.

Eickhoff, S., Paus, T., Caspers, S., and Grosbras, M. (2007). Assignment of functional

activations to probabilistic cytoarchitectonic areas revisited. *Neuroimage*, **36**, 511–521.

Fatemi-Ardekani, A., Boylan, C., and Noseworthy, M. (2009). Identification of breast calcification using magnetic resonance imaging. *Medical Physics*, **36**, 5429–5436.

Greve, D. and Fischl, B. (2009). Accurate and robust brain image alignment using boundary-based registration. *Neuroimage*, **48**, 63–72.

Guskiewicz, K. (2005). Association between recurrent concussion and late-life cognitive impairment in retired professional football players. *Neurosurgery*, **57**, 719–726.

Haacke, M. (1995). In vivo validation of the BOLD mechanism: a review of signal changes in gradient echo functional MRI in the presence of flow. *International Journal of Imaging Systems and Technology*, **6**, 153–163.

Haacke, M. (2004). Susceptibility Weighted Imaging (SWI). *Magnetic Resonance in Medicine*, **52**, 612–618.

Haacke, M. (2005). Imaging iron stores in the brain using magnetic resonance imaging. *Magnetic Resonance Imaging*, **23**, 1–25.

Haacke, M. (2007). Establishing a baseline phase behavior in magnetic resonance imaging to determine normal vs. abnormal iron content in the brain. *Journal of Magnetic Resonance Imaging*, **26**, 256–264.

Haacke, M. (2009). Characterizing iron deposition in multiple sclerosis lesions using susceptibility weighted imaging. *Journal of Magnetic Resonance Imaging*, **29**, 537–544.

Haacke, M., Mittal, S., Wue, Z., Neelavalli, J., and Cheng, Y. (2009). Susceptibility-weighted imaging: technical aspects and clinical applications, part 1. *Journal of Neuroradiology*, **30**, 19–30.

Haacke, M., Liu, S., Buch, S., Zheng, W., Dongmei, W., and Yongquan, Y. (2015). Quantitative susceptibility mapping: current status and future directions. *Magnetic Resonance Imaging*, **33**, 1–25.

Hua, K. (2008). Tract probability maps in stereotaxic spaces: analysis of white matter anatomy and tract-specific quantification. *Neuroimage*, **39**, 336–347.

Hughes, D. (2004a). Abnormalities on magnetic resonance imaging seen acutely following mild traumatic brain injury: correlation with neuropsychological tests and delayed recovery. *Neuroradiology*, **46**, 550–558.

Hughes, D. (2004b). Abnormalities on magnetic resonance imaging seen acutely following mild traumatic brain injury: correlation with neuropsychological tests and delayed recovery. *Neuroradiology*, **46**, 550–558.

Inglese, M. (2005). Diffuse axonal injury in mild traumatic brain injury: a diffusion tensor imaging study. *Journal of Neurosurgery*, **103**, 298–303.

Jenkinson, M. and Smith, S. (2001). A global optimisation method for robust affine registration of brain images. *Medical Image Analysis*, **5**, 143–156.

Jenkinson, M., Bannister, P., Brady, J., and Smith, S. (2002). Improved optimisation for the robust and accurate linear registration and motion correction of brain images. *Neuroimage*, **17**, 825–841.

Jenkinson, M., Beckmann, C., Behrens, T., Woolrich, M., and Smith, S. (2012). FSL. *Neuroimage*, **62**, 782–790.

Laitinen, T., Sierra, A., Bolkvadze, T., Pitkanen, A., and Grohn, O. (2015). Diffusion Tensor Imaging Detects Chronic microstructural changes in white and gray matter after traumatic brain injury in rat. *Frontiers in Neuroscience*, **9**, 128–140.

Lebel, C., Benner, T., and Bealiaeu, C. (2012). Six is enough? Comparison of Diffusion parameters measured using six or more diffusion-encoding gradient directions with deterministic tractography. *Magnetic Resonance in Medicine*, **68**, 474–483.

Lee, J. (2009). The contribution of myelin to magnetic susceptibility-weighted contrasts in high-field MRI of the brain. *Neuroimage*, **59**, 3967–3975.

Li, W., Wu, B., and Liu, C. (2011). Quantitative susceptibility mapping of human brain reflects spatial variation in tissue composition. *Neuroimage*, **55**, 1645–1656.

Lin, P., Chao, T., and Wu, M. (2014). Quantitative Susceptibility Mapping of Human Brain at 3T: A Multisite Reproducibility Study. *American Journal of Neuroradiology*, **36**, 467–474.

Lipton, M., Gulko, G., Zimmerman, M., Friedman, B., Gold, T., and Branch, C. (2009). Diffusion-Tensor Imaging Implicates Prefrontal Axonal Injury in Executive Function Impairment Following Very Mild Traumatic Brain Injury 1. *Radiology*, **252**, 816–824.

Liu, C. (2010). Susceptibility Tensor Imaging. *Magnetic Resonance in Medicine*, **63**, 1471–1477.

Liu, C., Lei, W., Tong, K., Yeom, K., and Kuzminski, S. (2015a). Susceptibility weighted imaging and quantitative susceptibility mapping in the brain. *Journal of Magnetic Resonance Imaging*, **42**, 23–41.

Liu, J., Xia, S., Hanks, R., Wiseman, N., and Peng, C. (2015b). Susceptibility Weighted Imaging and Mapping of Micro-hemorrhages and Major Deep Veins after Traumatic Brain Injury. *Journal of neurotrauma*, **33**, 10–21.

Liu, S., Mok, K., Neelavalli, K., Cheng, Y., Tang, J., and Haacke, M. (2014). Improved MR venography using quantitative susceptibilityweighted imaging. *Journal of Magnetic Resonance Imaging*, **40**, 698–708.

Mayer, A. (2010). A prospective diffusion tensor imaging study in mild traumatic brain injury. *Neurology*, **74**, 643–650.

Messe, A. (2011). Diffusion tensor imaging and white matter lesions at the subacute stage in mild traumatic brain injury with persistent neurobehavioral impairment. *Human Brain Mapping*, **23**, 999–1011.

Montgomery, D. and Runger, G. (2007). *Applied Statistics and Probability for Engineers*. John Wiley & Sons Inc., 4th edition.

Morey, R. (2013). Effects of chronic mild traumatic brain injury on white matter integrity in Iraq and Afghanistan war veterans. *Human Brain Mapping*, **34**, 2986–2999.

Mori, S. and Wakana, S. (2005). MRI Atlas of Human White Matter. *Elsevier*.

Mukherjee, P., Berman, J., Chung, S., Hess, C., and Henry, R. (2008). Diffusion

Tensor MR Imaging and Fiber Tractography: Theoretic Underpinnings. *American Journal of Neuroradiology*, **29**, 632–641.

Niogi, S., Jaghar, J., Johnson, C., Kolster, R., and Sarkar, R. (2008). Extent of microstructural white matter injury in postconcussive syndrome correlates with impaired cognitive reaction time: a 3T diffusion tensor imaging study of mild traumatic brain injury. *American Journal of Neuroradiology*, **29**, 967–973.

Parizel, P. (2007). Imaging findings in diffuse axonal injury after closed head trauma. *European Radiology*, **8**, 960–965.

Pierpaoli, C. (2001). Water diffusion changes in Wallerian degeneration and their dependence on white matter architecture. *Neuroimage*, **13**, 1174–1185.

Pierpaoli, C. and Basser, P. (1996). Toward a quantitative assessment of diffusion anisotropy. *Magnetic Resonance in Medicine*, **36**, 893–906.

Reichenbach, J. (1997). Small vessels in the human brain: MR venography with deoxyhemoglobin as an intrinsic contrast agent. *Radiology*, **204**, 272–277.

Reichenbach, J. (1998). High-resolution venography of the brain using magnetic resonance imaging. *Magnetic Resonance Materials in Physics, Biology and Medicine*, **6**, 62–69.

Reichenbach, J. (2000). High-resolution MR venography at 3.0 Tesla. *Journal of Computer Assisted Tomography*, **24**, 949–957.

Rivkin, M., Ball, W., Wang, D., McCracken, J., M.D., Brandt, M., Fletcher, J., and McKinstry, R. (2007). NIH: National Database for Autism Research - Pediatric MRI. http://pediatricmri.nih.gov. [Online; accessed May 2016].

Rutgers, D. (2008). White matter abnormalities in mild traumatic brain injury: a diffusion tensor imaging study. *American Journal of Neurology*, **29**, 514–519.

Schofield, M. and Zhu, Y. (2003). Fast phase unwrapping algorithm for interferometric applications. *Optic Letters*, **28**, 1194–1196.

Schweser, F., Deistung, A., Lehr, B., and Reichenbach, J. (2010). Quantitative imaging of intrinsic magnetic tissue properties using MRI signal phase: An approach to in vivo brain iron metabolism? *Neuroimage*, **54**, 2789–2807.

Shapiro, S. and Wilk, M. (1965). An analysis of variance test for normality (complete samples). *Biometrika*, **52**, 591–611.

Sharp, D. and Ham, T. (2011). nvestigating white matter injury after mild traumatic brain injury I. *Current Opinion in Neuroradiology*, **24**, 558–563.

Smith, S. (2002). Fast robust automated brain extraction. *Human Brain Mapping*, **17**, 143–155.

Smith, S., Jenkinson, M., Woolrich, M., Beckmann, C., Behrens, T., Johansen-Berg, H., Bannister, P., Luca, M. D., Drobnjak, I., Flitney, D., Niazy, R., Saunders, J., Vickers, J., Zhang, Y., Stefano, N. D., Brady, J., and Matthews, P. (2004). Advances in functional and structural MR image analysis and implementation as FSL. *Neuroimage*, **23**, 208–219.

Smits, M. (2011). Microstructural brain injury in post-concussion syndrome after minor head injury. *Neuroradiology*, **53**, 553–563.

Suskauer, S. and Huisman, T. (2009). Neuroimaging in pediatric traumatic brain

injury: current and future predictors of functional outcome. *Developmental Disabilities Research Review*, **15**, 117–123.

Tong, K. (2004). Diffuse axonal injury in children: clinical correlation with hemorrhagic lesions. *Annals of Neurology*, **56**, 36–50.

Tuch, D. (2002). High angular resolution diffusion imaging reveals intravoxel white matter fiber heterogeneity. *Magnetic Resonance in Medicine*, **48**, 577–582.

Vanderploeg, R. (2007). Long-term morbidities following self-reported mild traumatic brain injury. *Journal of Clinical and Experimental Neuropsychology*, **29**, 585–598.

Wakana, S. and Mori, S. (2007). Reproducibility of quantitative tractography methods applied to cerebral white matter. *Neuroimage*, **36**, 630–644.

Wang, X. (2014). Microbleeds on susceptibility-weighted MRI in depressive and non-depressive patients after mild traumatic brain injury. *Neurological Sciences*, **35**, 1533–1539.

Woolrich, M., S.Jbabdi, Patenaude, B., Chappell, M., Makni, S., Behrens, T., Beckmann, C., Jenkinson, M., and Smith, S. (2009). Bayesian Analysis of Neuroimaging Data in FSL. *Neuroimage*, **45**, 173–186.

Wozniak, J. (2007). Neurocognitive and neuroimaging correlates of pediatric traumatic brain injury: a diffusion tensor imaging (DTI) study. *Archives of Clinical Neuropsychology*, **22**, 555–568.

Wu, B., Li, W., Guidon, A., and Zhu, Y. (2012). Whole brain susceptibility mapping using compressed sensing. *Magnetic Resonance in Medicine*, **67**, 137–147.

Xiang, H. and Yablonskiy, D. (2009). Biophysical mechanisms of phase contrast in gradient echo MRI. *Proceedings of the National Academy of Sciences*, **106**, 13558–13563.

Yuh, E., Hawryluk, G., and Manley, G. (2014). Imaging Concussion: A Review. *Neurosurgery*, **75**, 50–63.